

DEPOLARIZATION EFFECTS AT 3 GHz DUE TO PRECIPITATION

by

Robert G. Humphries, M.Sc.

A thesis submitted to the Faculty of Graduate
Studies and Research of McGill University in
partial fulfilment of the requirements for the
degree of Doctor of Philosophy.

Department of Meteorology
McGill University

Montreal
October, 1973

ABSTRACT

Observations and calculations of the depolarization effects due to forward and backward scattering from precipitation have been carried out at 3 GHz.

The theoretical calculations, based on Rayleigh scattering theory, of the effects of forward scattering from water ellipsoids suggest that propagation through heavy rain can alter the polarization of the transmitted radiation to the extent that the polarization parameters of the backscattered radiation are no longer directly related to the backscatter properties of the precipitation particles. The PPI displays of the polarization parameters for a convective storm show the presence of strong propagation effects.

Observations made in widespread precipitation show the characteristics of the polarization parameters in rain and the melting layer. The observations are consistent with the idea that raindrops tend to fall as oblate spheroids with a vertical minor axis thus forming an anisotropic propagation medium.

Calculations of the effects of backscattering from water ellipsoids show the relationship of the rainfall rate and drop size distribution to the polarization parameters of the backscattered radiation.

RÉSUMÉ

Des observations et calculs des effets de dépolarisation due à la prodiffusion et la rétrodiffusion de la précipitation furent établis à 3 GHz.

Basés sur la diffusion Raleigh, les calculs théoriques des effets de prodiffusion d'ellipsoïde d'eau suggèrent que la propagation dans une pluie dense peut altérer la polarisation de la radiation transmise à un tel point que les paramètres de polarisation de la radiation rétrodiffusée ne sont plus directement reliés aux propriétés rétrodiffuses des particules de précipitation. Les présentations PPI des paramètres de polarisation d'une tempête de pluie convective démontrent la forte présence des effets de propagation.

Des observations en précipitation étendue démontrent les caractéristiques des paramètres de polarisation dans la pluie et au niveau de fusion. Ces observations sont compatibles avec l'idée que les gouttes de pluie tendent à tomber comme des sphéroïdes aplatis ayant leur axe mineur dans la vertical, formant ainsi un milieu de propagation anisotrope.

Des calculs des effets de rétrodiffusion d'ellipsoïdes d'eau démontrent la relation entre l'intensité de la précipitation et la répartition des gouttelettes en fonction de leurs dimensions, avec les paramètres de polarisation de la radiation rétrodiffusée.

ACKNOWLEDGEMENTS

The data for this thesis were obtained in Alberta while the author was associated with the field program of the Alberta Hall Studies of the Research Council of Alberta. The author gratefully acknowledges the cooperation and assistance of the Alberta Hall Studies staff especially Dr. P.W. Summers and Mr. J.H. Renick. The radar facilities were operated and maintained through the diligence of Steve Bond and his crew.

During the past years the author has had many fruitful discussions with Dr. G.C. McCormick, of the National Research Council, who provided many insights into the understanding of the data. The author acknowledges the efforts of Mr. A. Hendry, Mr. L. Allan, and Mr. P. Cook in the development, construction, and installation of equipment that was used in this study.

The patient guidance and counselling given by Dr. R.R. Rogers during his supervision of this thesis is gratefully acknowledged. During the early stages of this thesis, discussions with fellow-student Dr. Brian Barge helped the author gain an understanding of the Alberta Hall Studies polarization diversity radar and polarization research. His help in the field was invaluable. Dr. Henry Leighton provided many helpful suggestions during the writing of this thesis. Mr. Shue Fan Yip drafted the diagrams while Miss Ursula Seidenfuss made the photographic reproductions of the PPI displays.

I especially wish to thank my wife, Donna, who not only assisted in much of the tedious work associated with my research

but proof-read and typed this thesis.

The author was provided with financial assistance by the Atmospheric Environment Service, Environment Canada, the National Research Council of Canada, and the Research Council of Alberta.

PREFACE

Various people associated with the Alberta Hail Studies have been involved in radar studies to discriminate between rain and hail. The scope of this type of investigation was expanded with the acquisition of a 3 GHz polarization diversity radar which, in addition to the reflectivity, allowed the circular depolarization ratio (CDR), and the phase difference and correlation between the orthogonal components of the backscattered radiation to be studied.

The first investigation of hail detection with the polarization diversity radar was reported by Barge (1972). His research was primarily concerned with relating observations below the melting level of both the reflectivity and CDR to ground observations of rain and hail.

As a follow up, this thesis was undertaken to determine if measurements below the melting level of the phase angle and correlation could aid in discriminating rain from hail. The author spent the summer of 1971 collecting polarization data with a range-azimuth gated chart recorder system which samples the backscattered signal from one selected area of a storm during each rotation of the antenna. The analysis of the data, carried out during the winter at McGill, indicated that the polarization parameters in question were different in hailstorms than in stratiform rain but because of limitations in the data the reason for these differences could only be guessed at.

For the summer of 1972 equipment developed by the National Research Council enabled the phase angle and correlation to be displayed on a PPI scope for the first time. This display was a significant aid in the interpretation of these two parameters. The analysis of these data led to the investigation of forward scattering phenomena.

The following are the original contributions to knowledge of this thesis:

- a) Observations of the reflectivity, CDR, phase angle, and correlation together with theoretical calculations show that propagation through heavy rain can depolarize a 3 GHz circularly polarized wave. It is shown that this propagation effect can seriously influence the CDR so that it is no longer representative of the backscattered properties of the precipitation particles.
- b) It is demonstrated that the propagation effect tends to mask the effects of non-Rayleigh scattering with the result that the phase angle does not readily discriminate rain from hail.
- c) For a given reflectivity it is found that the average correlation measured at 3 GHz in Alberta is generally lower than that measured at 16.5 GHz in Ottawa. This average correlation tends to increase with the reflectivity. The correlation below the melting level in convective storms or convective cells imbedded in widespread precipitation is usually greater than 67%

(1)

indicating that a majority of the scatterers have similar orientations and thus form an anisotropic propagation medium.

- d) Calculations of the CDR and reflectivity for various rainfall rates using the drop size distribution of Marshall and Palmer (1948) and the size-shape relationship of Pruppacher and Pitter (1971) suggest that the CDR for rain has a limiting value. Furthermore, these calculations show that the reflectivity and CDR are sensitive to different parts of the drop size distribution. The drops that contribute the most to the CDR are larger than the drops that contribute the most to the reflectivity.

TABLE OF CONTENTS

	Page
ABSTRACT	ii
ACKNOWLEDGEMENTS	iv
PREFACE	vi
LIST OF TABLES	xi
LIST OF FIGURES	xii
LIST OF PLATES	xiv
I. THE POLARIZATION PROPERTIES OF ELECTROMAGNETIC RADIATION	
1.1 The monochromatic Plane Wave	1
1.2 The Polarization Properties of a Quasi-Monochromatic Plane Wave	3
II. A REVIEW OF POLARIZATION STUDIES OF PRECIPITATION	6
III. THE SCATTERING PROBLEM	
3.1 Components and Coordinate Systems	10
3.2 Propagation Between the Radar and Scatterer	12
3.3 Scattering From the Target	14
3.4 The Received Signals	15
3.5 The Observables	17
3.6 Forward Scattering and Propagation	20
3.7 The Scattering Matrix Elements	23
3.8 Summary	25
IV. THE RADAR FACILITIES	
4.1 The Alberta Hail Studies Radar	27
4.2 The Chart Recorder System	28
4.3 The Phase/Correlation PPI	31

	Page
4.4 Calibration	32
V. PROPAGATION	
5.1 Phase Angle Observations	34
5.2 Calculations of the Propagation Effect	36
5.3 The Storm of 27 July 1972	39
5.4 Propagation Through Hail	42
VI. BACKSCATTER EFFECTS	
6.1 The Orientation of Haindrops	54
6.2 Bright Band Observations	55
6.3 Non-Rayleigh Scattering	58
6.4 Correlation Observations	60
6.5 Backscatter Calculations	61
VII. SUMMARY AND CONCLUSIONS	
7.1 Summary	70
7.2 Conclusions	73
APPENDIX I. THE SCATTERING AMPLITUDES OF FOUR HAILSTONES	77
REFERENCES	79

LIST OF TABLES

	Page
5.1 The minimum and maximum diameters of four hailstones and their corresponding differential phase shift and attenuation at 3 GHz based on scattering amplitudes calculated by Oguchi for oblate spheroids of ice at 0°C.	43
6.1 The minimum and maximum diameters of four oblate hailstones and the orientation of the backscattered ellipse for a region containing only that type of hailstone.	59
A1.1 The minimum and maximum diameters, the axial ratio, and the diameter of an equivolumic sphere for the four selected hailstones.	77
A1.2 The forward scattering amplitudes of the four selected hailstones.	78
A1.3 The backward scattering amplitudes of the four selected hailstones.	78

LIST OF FIGURES

	Facing Page
1.1 Illustrations of elliptical, linear, and circular polarizations.	1
1.2 The relationship of the orientation of the backscattered ellipse to the phase difference between the left hand circular and right hand circular components.	2
3.1 Orientation of the symmetry axes of anisotropic medium with respect to the basic xyz coordinate system.	12
3.2 The coordinate systems defining the orientation of the scatterer.	14
3.3 Coordinate systems defining the orientation of water drops forming an anisotropic medium.	20
3.4 Forward scattering of a plane wave from a plane-parallel slab containing many raindrops with identical orientations.	21
3.5 Body axes of an oblate spheroid.	23
4.1 Block diagram of the antenna microwave circuitry of the Alberta Hail Studies radar.	27
4.2 Block diagram of the two channel receiving system.	28
4.3 Block diagram of the chart recorder system.	29
4.4 Transfer characteristics of the main and orthogonal signal channels of the chart recorder system.	32
4.5 The outputs of mixers A and B as a function of the RF phase shifter setting or the orientation of the linear polarization transmitted by the monitor.	33
5.1 Frequency distribution of orientations of the backscattered ellipse for observations above and below the melting level.	34
5.2 Size-shape relationship for freely falling water drops.	36

	Facing Page
5.3 The rain induced differential attenuation.	37
5.4 The rain induced differential phase shift.	37
5.5 Depolarization of a wave due to propagation through rain.	38
5.6 The rain induced differential phase shift as a function of the reflectivity.	39
5.7 Calculations of the intrinsic CDR and the CDR with the propagation term included, along a radial path at 350° azimuth for 0146 MDT-27 July 1972.	41
5.8 Same as Fig. 5.7 except at 5° azimuth for 0207 MDT-27 July 1972.	42
5.9 Same as Fig. 5.7 except at 25° azimuth for 0207 MDT-27 July 1972.	42
6.1 Samples of observations of the melting layer obtained with the chart recorder system.	55
6.2 Mean correlation as a function of reflectivity.	60
6.3 Scatter diagram of surface rain and hail reports with corresponding values of the CDR and reflectivity measured aloft by the radar, and including theoretical calculations of the CDR and reflectivity for rain.	62, 73
6.4 The contributions of each size interval of the drop size distribution to the CDR and Z for a rainfall rate of 100 mm/hr.	64
6.5 The diameter of the drops in the size interval contributing the most to the CDR and Z as a function of rain rate.	64

LIST OF PLATES

	Page
I. Main power PPI at 1° elevation for 0146 MDT-27 July 1972.	44
II. PPI display of the CDR at 1° elevation for 0146 MDT-27 July 1972.	45
III. PPI display of the correlation at 1° elevation for 0146 MDT-27 July 1972.	46
IV. Phase angle PPI at 1° elevation for 0149 MDT-27 July 1972.	47
V. Phase angle PPI at 1° elevation for 0152 MDT-27 July 1972.	48
VI. Main power PPI at 1° elevation for 0207 MDT-27 July 1972.	49
VII. PPI display of the CDR at 1° elevation for 0207 MDT-27 July 1972.	50
VIII. PPI display of the correlation at 1° elevation for 0207 MDT-27 July 1972.	51
IX. Phase angle PPI at 1° elevation for 0210 MDT-27 July 1972.	52
X. Phase angle PPI at 1° elevation for 0213 MDT-27 July 1972.	53
XI. Main power PPI at 1° elevation for 1748 MDT-23 June 1972.	65
XII. PPI display of the CDR at 1° elevation for 1748 MDT-23 June 1972.	66
XIII. PPI display of the correlation at 1° elevation for 1748 MDT-23 June 1972.	67
XIV. Phase angle PPI at 1° elevation for 1751 MDT-23 June 1972.	68
XV. Phase angle PPI at 4° elevation for 0156 MDT-27 July 1972.	69

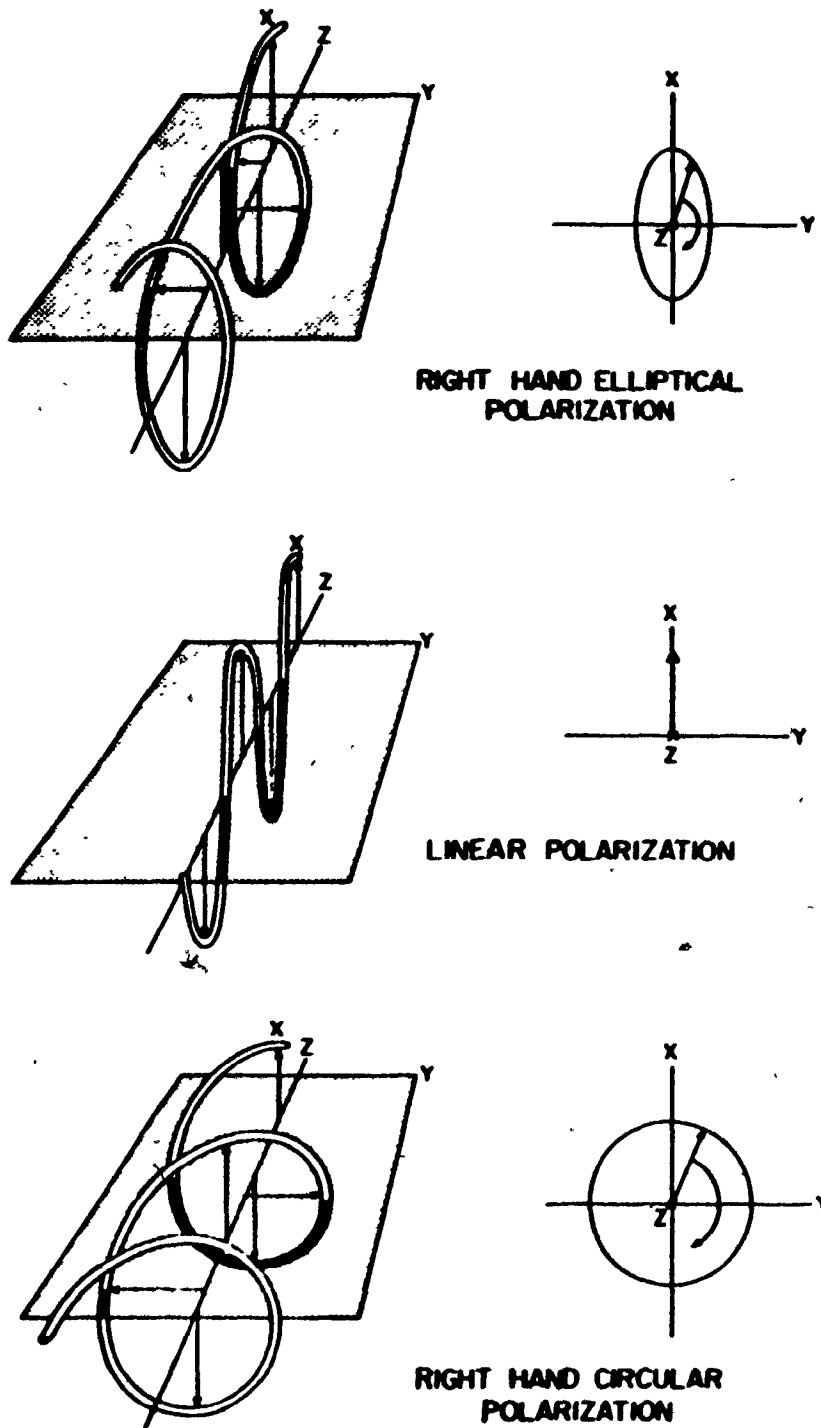


Fig. 1.1 Illustrations of elliptical, linear, and circular polarizations. The figures on the left represent the paths traced out by the electric field vectors as the waves propagate in the z direction. The figures on the right represent the paths traced out by the electric field vectors at a fixed point in space.

CHAPTER I

THE POLARIZATION PROPERTIES OF ELECTROMAGNETIC RADIATION

1.1 The Monochromatic Plane Wave

The polarization of a monochromatic plane wave refers to the time variation of the electric field vector at some fixed point in space. In general the electric vector will move periodically around an ellipse called the polarization ellipse and the wave is said to be elliptically polarized. When looking in the direction of propagation if the electric vector rotates clockwise the polarization is right hand elliptical (RHE) and counterclockwise rotation defines left hand elliptical (LHE). In the special case when the ellipse reduces to a straight line the wave is linearly polarized and when the electric vector traces out a circle the wave is circularly polarized. Fig. 1.1 illustrates the three types of polarization.

The complete polarization properties of the wave are specified by the shape or axial ratio of the polarization ellipse, its orientation, sense of rotation, and the maximum amplitude of the electric field vector describing the ellipse.

Consider a radar which transmits radiation with a known state of polarization and suppose that this radiation is scattered back by a region of precipitation. The backscattered radiation will generally be elliptically polarized and will therefore be described by the backscattered ellipse. Information about the scatterers is obtained by comparing the polarization properties of the backscattered ellipse to those of the

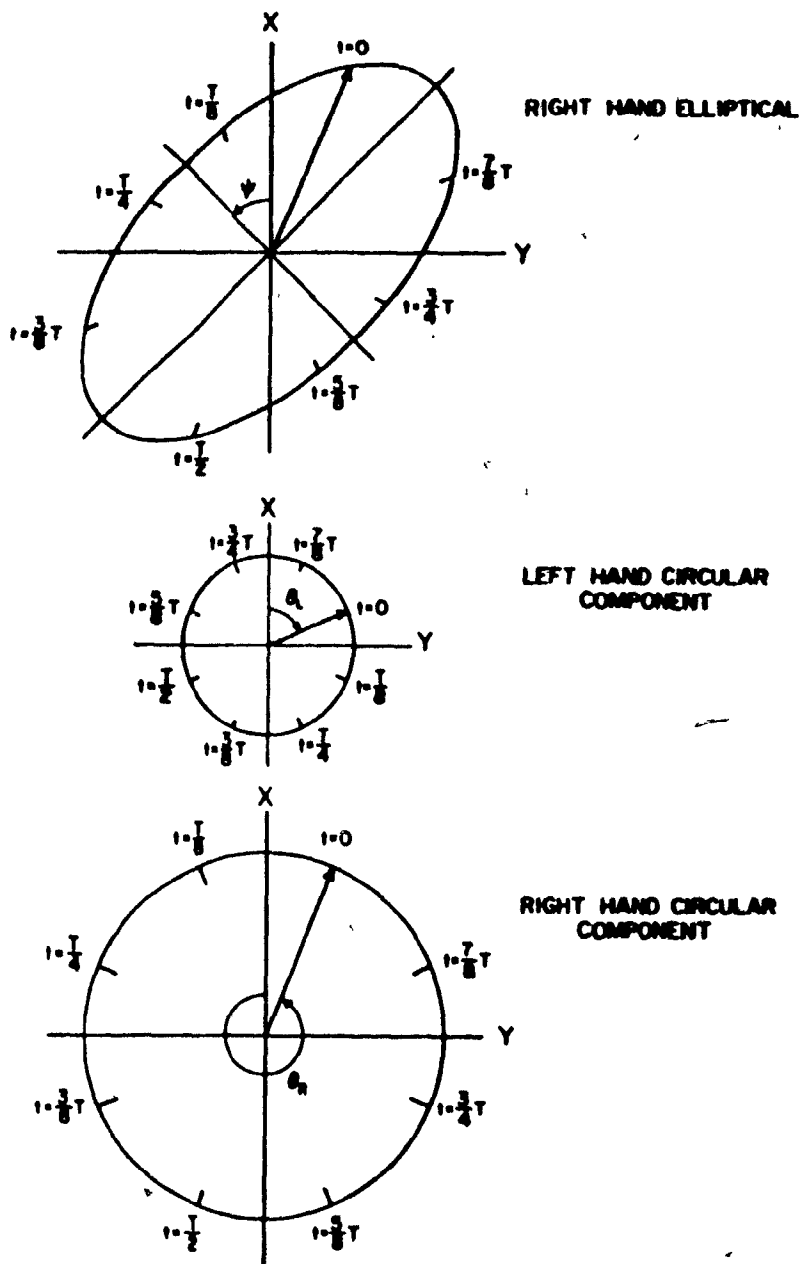


Fig. 1.2 The relationship of the orientation of the backscattered ellipse to the phase difference between the left hand circular and right hand circular components. The top figure represents one period of a right hand elliptically polarized wave propagating towards the radar (out of the page). ψ is the angle of the minor axis of the backscattered ellipse with respect to the x-axis as viewed from the radar. The two bottom figures represent the left hand circular and right hand circular components with their phase angles at time $t=0$.

transmitted wave. The polarization properties of the backscattered ellipse can be determined by resolving it into a main component and an orthogonal component and measuring the amplitudes and relative phases of these components.

If linear radiation is transmitted and the backscattered ellipse is resolved into orthogonal linear components then the main component lies in the same plane as the transmitted radiation and the orthogonal component is perpendicular to this plane. The ratio of the power of the orthogonal component to that of the main component will be called the linear depolarization ratio (LDR) and is related to the shape of the backscattered ellipse.

If circular radiation is transmitted then the backscattered ellipse can be resolved into a right hand circular (RHC) component and a left hand circular (LHC) component. In this case the main component has a sense of rotation opposite to that of the transmitted radiation and the orthogonal component has the same sense of rotation as the transmitted radiation. For circular components the ratio of the power of the orthogonal component to that of the main component will be called the circular depolarization ratio (CDR) and is related to the shape of the backscattered ellipse.

When circular components are used the orientation of the minor axis of the backscattered ellipse is related to half the phase difference between the RHC and LHC components. From Fig. 1.2 it can be seen that

$$\psi = \frac{\theta_R - \theta_L}{2} + m\left(\frac{\pi}{2}\right) \quad (1.1)$$

where ψ is the angle of orientation measured counterclockwise from the x-axis; $\theta_R - \theta_L$ is the phase difference between the RHC and LHC component; m is an integer chosen so that $-\frac{\pi}{2} \leq \psi \leq \frac{\pi}{2}$.

1.2 The Polarization Properties of a Quasi-Monochromatic Plane Wave

So far only monochromatic radiation has been considered. This type of radiation is always polarized which means that at each point in space the electric vector moves periodically around an ellipse. At the other extreme is unpolarized radiation where the electric vector moves irregularly. To avoid confusion, it should be noted at this point that the term depolarization refers to a change in the polarization state of a wave as a consequence of propagation, scattering, or any other interaction with matter. The wave, however, remains polarized. Thus the terms depolarized and unpolarized refer to two different wave properties.

The radiation backscattered from precipitation is usually quasi-monochromatic. This means that the radiation contains more than one frequency but the departures from the mean frequency \bar{f} are small. The various frequencies are a result of Doppler shifts due to the movement of the precipitation particles. In this case the movement of the electric vector is neither completely regular, nor completely irregular and the radiation is said to be partially polarized.

At some point in the wave field let the two orthogonal components of the backscattered ellipse be

$$E_1(t) = a_1(t) e^{j[2\pi\bar{f}t - \phi_1(t)]} \quad (1.2)$$

$$E_2(t) = a_2(t) e^{j[2\pi\bar{f}t - \phi_2(t)]} \quad (1.3)$$

where t is the time; \bar{f} is the mean frequency; $a_1(t)$ and $a_2(t)$ are the amplitudes; $\phi_1(t)$ and $\phi_2(t)$ are the phases. For a monochromatic wave a_1 , a_2 , ϕ_1 , and ϕ_2 would be constants and for a quasi-monochromatic wave these quantities are time dependent but the changes are relatively small in any time interval that is small compared to the inverse of the spectral width Δf .

The polarization properties of a quasi-monochromatic wave can be determined by using the coherency matrix introduced by Wolf (1954). The coherency matrix J is defined as

$$J = \begin{pmatrix} \langle E_1 E_1^* \rangle & \langle E_1 E_2^* \rangle \\ \langle E_2 E_1^* \rangle & \langle E_2 E_2^* \rangle \end{pmatrix} \quad (1.4)$$

where the bent brackets denote time average; the asterisks denote the complex conjugate. Substituting equations 1.2 and 1.3 into the coherency matrix yields

$$J = \begin{pmatrix} \langle a_1^2 \rangle & \langle a_1 a_2 e^{j(\phi_2 - \phi_1)} \rangle \\ \langle a_1 a_2 e^{-j(\phi_2 - \phi_1)} \rangle & \langle a_2^2 \rangle \end{pmatrix} \quad (1.5)$$

If RHC and LHC components are used then using the notation of McCormick (1968) the matrix elements will be written as

$$J = \begin{pmatrix} W_1 & W_3 + jW_4 \\ W_3 - jW_4 & W_2 \end{pmatrix} \quad (1.6)$$

where W_1 , W_2 , W_3 , and W_4 will be called the observables. The diagonal elements of the coherency matrix, W_1 and W_2 , represent the intensities of the two orthogonal circular components and

the non-diagonal elements, $W_1 + jW_2$, and $W_1 - jW_2$, express the correlation between the two components. Wolf (1959) derives a complex correlation factor ρ such that

$$\rho = |\rho| e^{j\phi} = \frac{W_1 + jW_2}{\sqrt{W_1 W_2}} \quad (1.7)$$

The absolute value $|\rho|$ is a measure of the degree of correlation between the two components and ϕ is the effective phase difference between them.

If $E_1(t)$ is the orthogonal/circular component and $E_2(t)$ is the main circular component then the circular depolarization ratio is

$$\text{CDR} = \frac{W_1}{W_2} \quad (1.8)$$

Having determined the coherency matrix for the backscattered radiation the next step is to relate the observables to properties of the scattering particles. This problem will be discussed in Chapter III.

CHAPTER II

A REVIEW OF POLARIZATION STUDIES OF PRECIPITATION

The polarization properties of non-spherical precipitation particles were first given theoretical consideration by Kerker and Hitschfeld (1950); Atlas, Kerker, and Hitschfeld (1953); Labrum (1952); and later by Shupiatskii (1959); and Gershenson and Shupiatskii (1961). The basis of these studies was Gans' extension of Rayleigh's scattering theory to ellipsoids (Gans, 1912). Results indicated the possibilities of determining the type of precipitation that the radar was detecting by measuring the polarization properties of the backscattered radiation.

Experimental procedures for measuring these polarization properties have been discussed by Newell et al. (1955), Marshall and Gordon (1957), and Shupiatskii and Morgunov (1963). McCormick (1968) described an antenna capable of simultaneous measurement of the main and orthogonal components of the backscattered radiation.

Early measurements of the polarization properties of radiation backscattered by precipitation were reported by Browne and Robinson (1952), Hunter (1954), Wexler (1955), and Newell et al. (1955). These investigations were involved with the measurement of the LDRs and cancellation ratios² of radiation

² The cancellation ratio is the ratio of the power of the orthogonal backscattered component when circular polarization is transmitted to that of the main backscattered component when linear polarization is transmitted.

backscattered from rain, snow, and the melting layer so that information about the shape of the backscattered ellipse was obtained. The depolarizations measured from snow were larger than predicted by Atlas, Kerker, and Hitschfeld (1953) who calculated negligible values for snow particles of low density.

Polarization observations of thunderstorms which produced hail have been reported by Newell et al. (1957) and Peter (1966). A comparison shows the results to be contradictory suggesting that measurements of the CDR or LDR were not sufficient to uniquely discriminate between hail and rain with a radar. Barge (1972) combined measurements of the reflectivity factor (Z_e) and the CDR and compared these values with ground observations of precipitation. It was found that the combination was more effective in distinguishing hail than either quantity taken alone.

Observations of polarization parameters including the phase angle and correlation between the main and orthogonal components at 16.5 GHz have been reported by McCormick and Hendry (1970, 1972). They have found that for rain the CDR increases as Z_e increases; for reflectivities greater than 30 dBz the correlation is around 80%, and the phase angle in rain suggests that the drops fall with their minor axis vertical. Barge (1972) also found that at 2.88 GHz the CDR increases with Z_e .

Propagation effects have primarily been the concern of people in communications. As radiation passes through a region of precipitation comprised of non-spherical drops with a preferred orientation the polarization may be altered.

Theoretical considerations of this problem have been reported by Oguchi (1960, 1964, 1966). He calculated the forward and backward scattering amplitudes at 19.3 and 34.8 GHz for non-spherical raindrops which were not small with respect to the wavelength. Watson and Arbabi (1973) calculated the differential attenuation and differential phase shift between horizontally polarized radiation and vertically polarized radiation for frequencies between 3 and 36 GHz for various rainfall rates. Their measurements were carried out at 11 GHz. At the Bell Laboratories, Morrison, Cross, and Chu (1973) have performed calculations similar to Oguchi's and obtained the differential attenuation and phase shift at 4, 18.1 and 30 GHz. They suggested that the differential phase shift in heavy rain could induce depolarization of an electromagnetic wave at 4 GHz. Propagation effects induced by precipitation at 16.5 and 2.88 GHz have been reported by McCormick et al. (1972). The observations indicated that at 16.5 GHz there was a significant propagation effect due to rain. The observation of a propagation effect at 2.88 GHz was attributed to the existence of hail in the propagation path.

The extent that rain may cause depolarization of an electromagnetic wave at 3 GHz has not been thoroughly investigated. Nor has there been significant observational evidence to show that a propagation effect due to rain has been observed at this frequency. Polarization observations at 3 GHz continue to be investigated as a means to distinguish between

rain and hail with a radar. Since depolarization caused by propagation through rain could significantly influence the interpretation of the data, the extent to which rain can induce a propagation effect at 3 GHz is a problem of prime importance.

CHAPTER III

THE SCATTERING PROBLEM

In this chapter, the observables discussed in Chapter I will be related to the propagation of a wave from the radar to the target; scattering from the target; and propagation back to the radar. These relationships will be made by using the scattering matrix whose elements are determined by the properties of the scattering particle. Rayleigh scattering theory is used to obtain the scattering matrix elements for ellipsoidal targets. Many of the developments in this chapter follow the work of McCormick (1968), Barge (1972), and the theories set forth in Van de Hulst (1957).

3.1 Components and Coordinate Systems

Consider a radar transmitting radiation of arbitrary elliptical polarization that is scattered by a precipitation particle. The transmitted elliptical wave can be resolved into components along the x and y axes of a basic xyz coordinate system. In this basic coordinate system the z-axis is along the direction of propagation pointing away from the radar, the y-axis is along the horizontal, and the x-axis is orthogonal to both. The wave may then be written as

$$\vec{E}_+ = E_x \hat{x} + E_y \hat{y} \quad (3.1)$$

where \hat{x} and \hat{y} are unit vectors in the direction of the axes; the plus sign indicates propagation away from the radar. If circular

components are considered then

$$\vec{E}_+ = E_{R+} \hat{R}_+ + E_{L+} \hat{L}_+ \quad (3.2)$$

where \hat{R}_+ and \hat{L}_+ are unit vectors for RHC and LHC polarization travelling away from the radar. The relationship between the unit vectors for circular and linear polarizations is discussed in Crispin and Siegel (1968, pp. 49-58) with the result

$$\begin{pmatrix} \hat{R}_+ \\ \hat{L}_+ \end{pmatrix} = \frac{1}{\sqrt{2}} \begin{pmatrix} 1 & -j \\ 1 & j \end{pmatrix} \begin{pmatrix} \hat{x} \\ \hat{y} \end{pmatrix} = U \begin{pmatrix} \hat{x} \\ \hat{y} \end{pmatrix} \quad (3.3)$$

where $j = \sqrt{-1}$. The components are then related by

$$\begin{pmatrix} E_{R+} \\ E_{L+} \end{pmatrix} = \frac{1}{\sqrt{2}} \begin{pmatrix} 1 & j \\ 1 & -j \end{pmatrix} \begin{pmatrix} E_{x+} \\ E_{y+} \end{pmatrix} = U^* \begin{pmatrix} E_{x+} \\ E_{y+} \end{pmatrix} \quad (3.4)$$

or

$$\begin{pmatrix} E_{x+} \\ E_{y+} \end{pmatrix} = \frac{1}{\sqrt{2}} \begin{pmatrix} 1 & 1 \\ -j & j \end{pmatrix} \begin{pmatrix} E_{R+} \\ E_{L+} \end{pmatrix} = U^T \begin{pmatrix} E_{R+} \\ E_{L+} \end{pmatrix} \quad (3.5)$$

where the asterisk denotes the complex conjugate and the T denotes the transpose.

To preserve the sense of rotation, as defined in Chapter I, for transmitted and backscattered radiation the relationship between the backscattered linear and circular components is

$$\begin{pmatrix} E_{R-} \\ E_{L-} \end{pmatrix} = \frac{1}{\sqrt{2}} \begin{pmatrix} 1 & -j \\ 1 & j \end{pmatrix} \begin{pmatrix} E_{x-} \\ E_{y-} \end{pmatrix} = U \begin{pmatrix} E_{x-} \\ E_{y-} \end{pmatrix} \quad (3.6)$$

or

$$\begin{pmatrix} E_{x-} \\ E_{y-} \end{pmatrix} = \frac{1}{\sqrt{2}} \begin{pmatrix} 1 & 1 \\ j & -j \end{pmatrix} \begin{pmatrix} E_{R-} \\ E_{L-} \end{pmatrix} = U^{*T} \begin{pmatrix} E_{R-} \\ E_{L-} \end{pmatrix} \quad (3.7)$$

where the minus sign indicates propagation towards the radar.

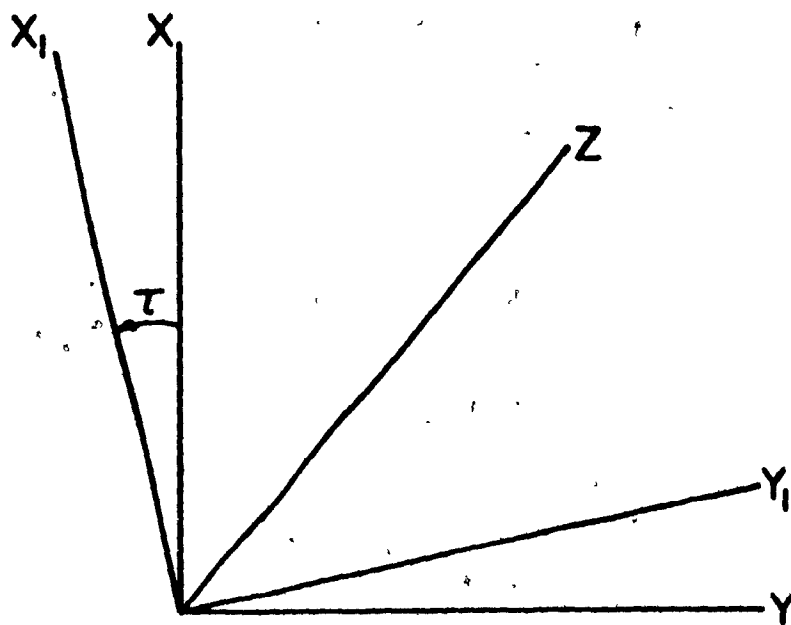


Fig. 3.1 Orientation of the symmetry axes of an anisotropic medium with respect to the basic xyz coordinate system. Propagation is along the z-axis.

3.2 Propagation Between the Radar and Scatterer

In an isotropic propagation medium the x and y components of the transmitted wave at a distance r from the radar may be written as

$$E_{x+} = \frac{A_x}{r} e^{j(-k_0 r + \omega t - \phi_x)} \quad (3.8)$$

$$E_{y+} = \frac{A_y}{r} e^{j(-k_0 r + \omega t - \phi_y)} \quad (3.9)$$

where k_0 is the propagation constant of the medium; ω is the angular frequency; ϕ_x and ϕ_y are phases.

A region of precipitation composed of ellipsoidal particles with a preferred orientation constitutes an anisotropic propagation medium. This anisotropy can be specified by propagation constants k' and k'' so that the components along a new set of axes x_1 and y_1 , which are the symmetry axes of the anisotropy, may be written as

$$E_{x_1+} = \frac{A_{x_1}}{r} e^{j(-k' r + \omega t - \phi_{x_1})} \quad (3.10)$$

$$E_{y_1+} = \frac{A_{y_1}}{r} e^{j(-k'' r + \omega t - \phi_{y_1})} \quad (3.11)$$

Retaining only the range dependent terms the components at the scatterer are expressed in terms of their values at the radar by

$$\begin{pmatrix} E_{x_1+} \\ E_{y_1+} \end{pmatrix}_{\text{scatterer}} = \frac{1}{r} \begin{pmatrix} e^{-jk' r} & 0 \\ 0 & e^{-jk'' r} \end{pmatrix} \begin{pmatrix} E_{x_1+} \\ E_{y_1+} \end{pmatrix}_{\text{radar}} \quad (3.12)$$

If the x_1 -axis of the $x_1 y_1 z$ coordinate system makes an angle τ with respect to the x -axis of the basic xyz coordinate system, as in Fig. 3.1, then the components in each system are related by the rotation

$$\begin{pmatrix} E_{x_1+} \\ E_{y_1+} \end{pmatrix} = \begin{pmatrix} \cos\tau & \sin\tau \\ -\sin\tau & \cos\tau \end{pmatrix} \begin{pmatrix} E_{x_1+} \\ E_{y_1+} \end{pmatrix} = R_1 \begin{pmatrix} E_{x_1+} \\ E_{y_1+} \end{pmatrix} \quad (3.13)$$

or

$$\begin{pmatrix} E_{x_1+} \\ E_{y_1+} \end{pmatrix} = \begin{pmatrix} \cos\tau & -\sin\tau \\ \sin\tau & \cos\tau \end{pmatrix} \begin{pmatrix} E_{x_+} \\ E_{y_+} \end{pmatrix} = R_1^T \begin{pmatrix} E_{x_+} \\ E_{y_+} \end{pmatrix} \quad (3.14)$$

Therefore the components at the scatterer in the xyz coordinate system are

$$\begin{pmatrix} E_{x_+} \\ E_{y_+} \end{pmatrix}_{\text{scatterer}} = R_1 \frac{1}{r} \begin{pmatrix} e^{-jk'r} & 0 \\ 0 & e^{-jk''r} \end{pmatrix} R_1^T \begin{pmatrix} E_{x_+} \\ E_{y_+} \end{pmatrix}_{\text{radar}} \quad (3.15)$$

When circular components are used equations (3.4) and (3.5) must be applied to equation (3.15) with the result

$$\begin{pmatrix} E_{R_+} \\ E_{L_+} \end{pmatrix}_{\text{scatterer}} = U^* R_1 \frac{1}{r} \begin{pmatrix} e^{-jk'r} & 0 \\ 0 & e^{-jk''r} \end{pmatrix} R_1^T \begin{pmatrix} E_{R_+} \\ E_{L_+} \end{pmatrix}_{\text{radar}} \quad (3.16)$$

which upon expansion becomes

$$\begin{pmatrix} E_{R_+} \\ E_{L_+} \end{pmatrix}_{\text{scatterer}} = \frac{1}{r} \frac{e^{-jkr}}{\sqrt{1-(pe^{j\chi})^2}} \begin{pmatrix} 1 & pe^{j(\chi-2\tau)} \\ pe^{j(\chi+2\tau)} & 1 \end{pmatrix} \begin{pmatrix} E_{R_+} \\ E_{L_+} \end{pmatrix}_{\text{radar}} \quad (3.17)$$

where

$$pe^{j\chi} = \tanh\left[j\left(\frac{k''-k'}{2}\right)r\right], \quad k = \frac{k'+k''}{2} \quad (3.18)$$

Equation (3.17) can be rewritten as

$$\begin{pmatrix} E_{R_+} \\ E_{L_+} \end{pmatrix}_{\text{scatterer}} = \frac{e^{-jkr}}{r} P \begin{pmatrix} E_{R_+} \\ E_{L_+} \end{pmatrix}_{\text{radar}} \quad (3.19)$$

with P referred to as the propagation matrix.

For a wave travelling from the target to the radar τ appears to change sign so that for radiation originating at the target the field in circular components at the radar is

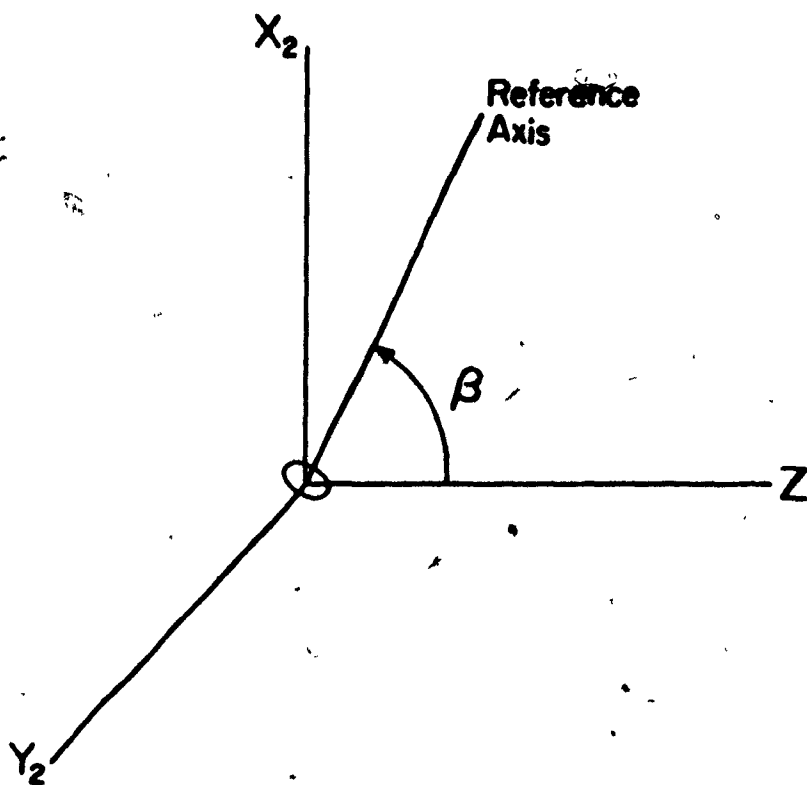
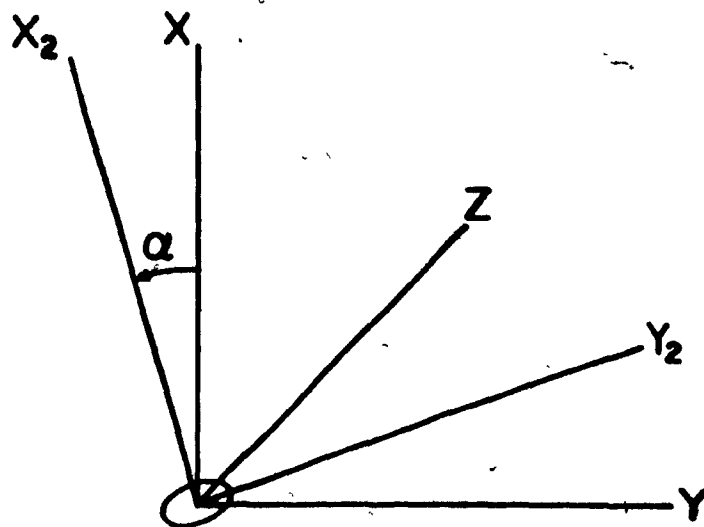


Fig. 3.2 The coordinate systems defining the orientation of the scatterer. The top figure relates the x_2y_2z coordinate system to the basic xyz coordinate system. The bottom figure relates the reference axis of the scatterer to the x_2y_2z coordinate system. The reference axis lies in the x_2z plane.

$$\begin{pmatrix} E_{R-} \\ E_{L-} \end{pmatrix}_{\text{radar}} = \frac{e^{-jkr}}{r} P^T \begin{pmatrix} E_{R-} \\ E_{L-} \end{pmatrix}_{\text{scatterer}} \quad (3.20)$$

3.3 Scattering From the Target

A reference axis, say an axis of symmetry, may be attached to the scattering particle and an x_2y_2z coordinate system defined so that this axis lies in the x_2z plane and makes an angle β with the z -axis. The x_2 -axis is inclined at an angle α with respect to the basic x -axis (see Fig. 3.2).

After resolving the incident and scattered wave into components along the x_2 and y_2 axes a scattering matrix is defined so that

$$\begin{pmatrix} E_{x_2-} \\ E_{y_2-} \end{pmatrix}_{\text{scatterer}} = \begin{pmatrix} S_{11} & S_{12} \\ S_{21} & S_{22} \end{pmatrix} \begin{pmatrix} E_{x_2+} \\ E_{y_2+} \end{pmatrix}_{\text{scatterer}} \quad (3.21)$$

where the S_{ij} are elements of the scattering matrix which will be discussed in Section 3.7 and where it will be shown that for ellipsoids $S_{12} = S_{21}$.

The components in the x_2y_2z coordinate system are related to the components in the xyz coordinate system by the rotation

$$\begin{pmatrix} E_x \\ E_y \end{pmatrix} = \begin{pmatrix} \cos\alpha & \sin\alpha \\ -\sin\alpha & \cos\alpha \end{pmatrix} \begin{pmatrix} E_{x_2} \\ E_{y_2} \end{pmatrix} = R_2 \begin{pmatrix} E_{x_2} \\ E_{y_2} \end{pmatrix} \quad (3.22)$$

or

$$\begin{pmatrix} E_{x_2} \\ E_{y_2} \end{pmatrix} = \begin{pmatrix} \cos\alpha & -\sin\alpha \\ \sin\alpha & \cos\alpha \end{pmatrix} \begin{pmatrix} E_x \\ E_y \end{pmatrix} = R_2^T \begin{pmatrix} E_x \\ E_y \end{pmatrix} \quad (3.23)$$

The scattering equation (3.21) can now be written as

$$\begin{pmatrix} E_{x-} \\ E_{y-} \end{pmatrix}_{\text{scatterer}} = R_2 \begin{pmatrix} S_{11} & S_{12} \\ S_{12} & S_{22} \end{pmatrix} R_2^T \begin{pmatrix} E_{x+} \\ E_{y+} \end{pmatrix}_{\text{scatterer}} \quad (3.24)$$

To obtain the result of scattering with circular components equations (3.5) and (3.6) are applied to equation (3.24) to yield

$$\begin{pmatrix} E_{R-} \\ E_{L-} \end{pmatrix}_{\text{scatterer}} = UR_2 \begin{pmatrix} S_{11} & S_{12} \\ S_{12} & S_{22} \end{pmatrix} R_2^T U^T \begin{pmatrix} E_{R+} \\ E_{L+} \end{pmatrix}_{\text{scatterer}} \quad (3.25)$$

which upon expansion becomes

$$\begin{pmatrix} E_{R-} \\ E_{L-} \end{pmatrix}_{\text{scatterer}} = \frac{S_{11} + S_{22}}{2} \begin{pmatrix} v^+ & 1 \\ 1 & v^- \end{pmatrix} \begin{pmatrix} E_{R+} \\ E_{L+} \end{pmatrix}_{\text{scatterer}} \quad (3.26)$$

with

$$v^\pm = \frac{(S_{11} - S_{22} \mp 2jS_{12})}{S_{11} + S_{22}} e^{\pm 2j\alpha} \quad (3.27)$$

The scattering term v^\pm can also be written as

$$v^\pm = \left| \frac{S_{11} - S_{22} \mp 2jS_{12}}{S_{11} + S_{22}} \right| e^{j(\delta_\pm \pm 2\alpha)} \quad (3.28)$$

where δ_\pm is the scattering differential phase shift. For symmetric particles $S_{12} = 0$ and therefore $\delta_+ = \delta_-$ so that

$$v^\pm = \left| \frac{S_{11} - S_{22}}{S_{11} + S_{22}} \right| e^{j(\delta \pm 2\alpha)} = v e^{j(\delta \pm 2\alpha)} \quad (3.29)$$

3.4 The Received Signals

Expressions have now been obtained that describe the effects on the transmitted radiation as it travels to the target, scatters from the target, and travels back to the radar. The net result of these interactions is obtained by combining equations

(3.19), (3.20) and (3.26) to yield

$$\begin{pmatrix} E_{R-} \\ E_{L-} \end{pmatrix}_{\text{radar}} = \frac{e^{-2jkr}}{2r^2} (S_{11} + S_{22}) P^T \begin{pmatrix} v^+ & 1 \\ 1 & v^- \end{pmatrix} P \begin{pmatrix} E_{R+} \\ E_{L+} \end{pmatrix}_{\text{radar}} \quad (3.30)$$

Expansion of this equation results in

$$\begin{pmatrix} E_{R-} \\ E_{L-} \end{pmatrix}_{\text{radar}} = \frac{e^{-2jkr}}{2r^2} (S_{11} + S_{22}) \begin{pmatrix} v^+ + 2pe^{j(\chi+2\tau)} & 1 \\ 1 & v^- + 2pe^{j(\chi-2\tau)} \end{pmatrix} \begin{pmatrix} E_{R+} \\ E_{L+} \end{pmatrix}_{\text{radar}} \quad (3.31)$$

where terms involving the propagation factor to higher than the first order have been dropped. This is based on the assumption that $p \ll 1$ which is valid only as long as propagation effects do not dominate scattering effects.

If circularly polarized radiation of unit amplitude is transmitted then from equation (3.31) the orthogonal component, at the radar, of the radiation backscattered by a single particle is

$$E_{11} = \frac{e^{-2jkr_1}}{2r_1^2} (S_{111} + S_{221}) [v_1 e^{j(\delta_1 + 2\alpha_1)} + 2pe^{j(\chi + 2\tau)}] \quad (3.32)$$

where the upper plus sign refers to transmission of RHC polarization and the lower minus sign to transmission of LHC polarization; the 1 identifies the scattering particle. The main component is

$$E_{21} = \frac{e^{-2jkr_1}}{2r_1^2} (S_{111} + S_{221}) \quad (3.33)$$

For an ensemble of N scatterers the orthogonal and main components received at the radar are

$$E_1 = \sum_1^N E_{11}, \quad E_2 = \sum_1^N E_{21} \quad (3.34)$$

where single scattering is assumed.

3.5 The Observables

Having obtained expressions for the main and orthogonal circular components of the backscattered radiation it is now possible to find expressions for the observables W_1 , W_2 , W_3 and W_4 introduced in (1.6).

The main backscattered power, W_2 , is obtained by taking the time average of $E_2 E_2^*$ so that

$$W_2 = \langle E_2 E_2^* \rangle$$

$$= \left\langle \sum_1 \frac{e^{-2jkr_1}}{2r_1^2} (S_{111} + S_{221}) \times \sum_l \frac{e^{2jk^*r_l}}{2r_l^2} (S_{11l} + S_{22l})^* \right\rangle \quad (3.35)$$

Letting

$$B_1 = \frac{e^{-2jkr_1}}{2r_1^2} \quad (3.36)$$

and assuming the scatterers to be distributed randomly in space then the products of phase terms $B_1 B_l$, with $l \neq 1$, average to zero. Therefore equation (3.35) becomes

$$W_2 = \left\langle \sum_1 |B_1|^2 |S_{111} + S_{221}|^2 \right\rangle \quad (3.37)$$

Applying the same arguments to the orthogonal backscattered power, W_1 , yields

$$W_1 = \langle E_1 E_1^* \rangle$$

$$= \left\langle \sum_1 |B_1|^2 |S_{111} + S_{221}|^2 |ve^{j(\delta_1 \pm 2\alpha_1)} + 2pe^{j(\chi \pm 2\tau)}|^2 \right\rangle \quad (3.38)$$

Instead of working with $W_3 + jW_4 = \langle E_1 E_2^* \rangle$ it is convenient to consider the expression

$$\frac{W_3 + jW_4}{W_2}$$

$$= \frac{\left\langle \sum_1 |B_1|^2 |S_{111} + S_{221}|^2 [ve^{j(\delta_1 \pm 2\alpha_1)} + 2pe^{j(\chi \pm 2\tau)}] \right\rangle}{\left\langle \sum_1 |B_1|^2 |S_{111} + S_{221}|^2 \right\rangle} \quad (3.39)$$

McCormick (1968) has suggested a model where the fraction ρ_α of the scatterers have mean scattering parameters $\bar{\nu}$, $\bar{\delta}$, and orientation $\bar{\alpha}$. The fraction $1-\rho_\alpha$ are randomly oriented and thus make a null contribution to the term containing $e^{\pm j2\alpha}$. Equation (3.39) then reduces to

$$\frac{W_3 + jW_4}{W_2} = \rho_\alpha \bar{\nu} e^{j(\bar{\delta} \pm 2\bar{\alpha})} + 2\rho e^{j(\chi \pm 2\tau)} \quad (3.40)$$

Recall equation (1.7)

$$\rho = |\rho| e^{j\phi} = \frac{W_3 + jW_4}{\sqrt{W_1 W_2}}$$

where $|\rho|$ is a measure of the degree of correlation and ϕ is the effective phase difference between the main and orthogonal components. It can be seen that the effective phase difference is given by

$$\tan \phi = \frac{W_4}{W_3} \quad (3.41)$$

and in an isotropic medium

$$\frac{W_4}{W_3} = \tan (\bar{\delta} \pm 2\bar{\alpha}) \quad (3.42)$$

For ellipsoidal Rayleigh scatterers $\delta=0$ so that

$$\phi = \arctan \frac{W_4}{W_3} = \pm 2\bar{\alpha} \quad (3.43)$$

which states that the orientation of the backscattered ellipse is the same as the orientation of the contributing scatterers. This is not true in an anisotropic medium where propagation effects become important.

The CDR is given by

$$\frac{W_1}{W_2} = \frac{\langle \sum_1 |B_1|^2 |S_{111} + S_{221}|^2 |ve^{j(\delta_1 \pm 2\alpha_1)} + 2pe^{j(\chi \pm 2\tau)}|^2 \rangle}{\langle \sum_1 |B_1|^2 |S_{111} + S_{221}|^2 \rangle}$$

$$= \frac{|ve^{j(\delta \pm 2\alpha)} + 2pe^{j(\chi \pm 2\tau)}|^2}{|ve^{j(\delta \pm 2\alpha)} + 2pe^{j(\chi \pm 2\tau)}|^2} \quad (3.44)$$

The correlation is

$$|\rho| = \left(\frac{W_3^2 + W_4^2}{W_1 W_2} \right)^{\frac{1}{2}} = \left(\frac{(W_3^2 + W_4^2)(W_2)}{W_1} \right)^{\frac{1}{2}} \quad (3.45)$$

Therefore, combining equations (3.40) and (3.44) with (3.45) yields

$$|\rho| = \frac{|\rho_\alpha \bar{v} e^{j(\bar{\delta} \pm 2\bar{\alpha})} + 2pe^{j(\chi \pm 2\tau)}|}{\left(|ve^{j(\delta \pm 2\alpha)} + 2pe^{j(\chi \pm 2\tau)}|^2 \right)^{\frac{1}{2}}} \quad (3.46)$$

which in an isotropic medium reduces to

$$|\rho| = \frac{\rho_\alpha |\bar{v} e^{j(\bar{\delta} \pm 2\bar{\alpha})}|}{\left(|ve^{j(\delta \pm 2\alpha)}|^2 \right)^{\frac{1}{2}}} \quad (3.47)$$

This shows that the correlation is a measure of the fraction of scatterers with a preferred orientation. In general $|\rho| \leq \rho_\alpha$. As the propagation term, $2pe^{j(\chi \pm 2\alpha)}$, begins to dominate the scattering term, $ve^{j(\delta \pm 2\alpha)}$, the correlation will increase and in the limit approach unity.

The observables have now been related to the effect of scattering and the influence of an anisotropic propagation medium. The scattering effect is described by the scattering matrix elements. The propagation effect will now be treated as a forward scattering problem and related to the scattering matrix elements.

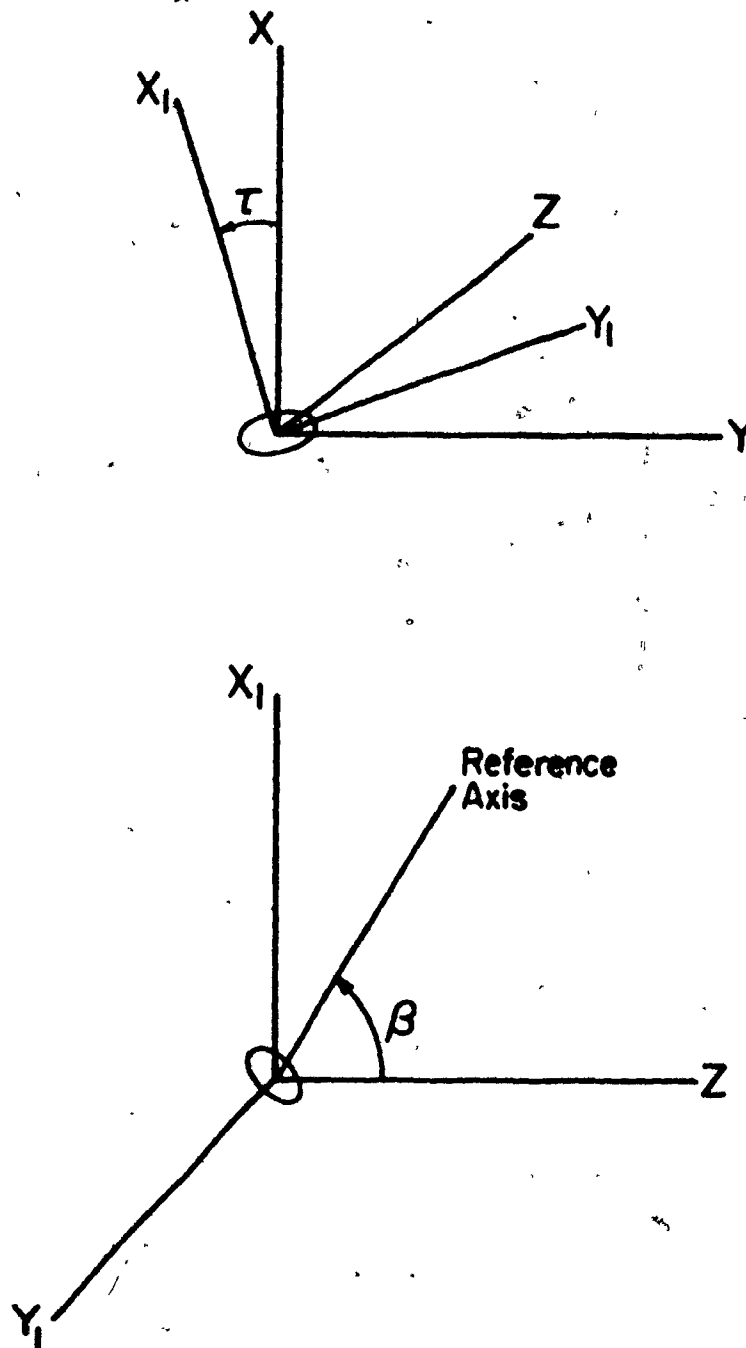


Fig. 3.3 Coordinate systems defining the orientation of water drops forming an anisotropic medium. The top figure relates the symmetry axes of the anisotropy to the basic xyz coordinate system. The bottom figure relates the reference axis of the water drop to the symmetry axes of the anisotropy.

3.6 Forward Scattering and Propagation

Let a single water drop shaped like an oblate spheroid be oriented so that in an x_1, y_1, z coordinate system its symmetry axis lies in the x_1, z plane as in Fig. 3.3. Consider an incident plane wave of unit amplitude linearly polarized in the x_1 direction. This wave may be written as

$$E_o = e^{-jk_o z} \quad (3.48)$$

where k_o is the propagation constant of the medium; the time dependent term has been omitted.

On the z -axis at a distance r from the particle the spherical scattered wave is of the form

$$E_s = S_{11}(\theta) \frac{e^{-jk_o r}}{r} = \frac{S_{11}(\theta)}{r} e^{-jk_o(r-z)} E_o \quad (3.49)$$

where $S_{11}(\theta)$ is the scattering amplitude (an element of the scattering matrix); $\theta=0^\circ$ for forward scattering and $\theta=180^\circ$ for backscattering.

In the forward direction the resultant field is the sum of the scattered field plus the incident field so that

$$E_R = E_s + E_o = E_o \left(1 + \frac{S_{11}(0)}{r} e^{-jk_o(r-z)} \right) \quad (3.50)$$

Now consider a plane parallel slab of depth l containing many identical drops with identical orientations. At some point P where $OP=z$ the resultant field is

$$E_R = E_o \left[1 + S_{11}(0) \sum \frac{e^{-jk_o(r-z)}}{r} \right] \quad (3.51)$$

where the sum is carried over all N drops in a unit volume.

Fig. 3.4 shows the geometry of the situation. For z

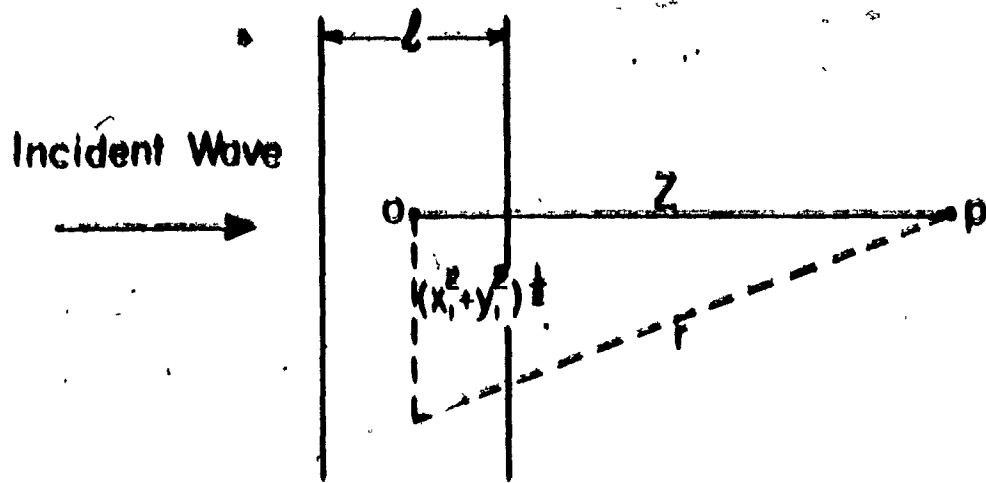


Fig. 1.4 Forward scattering of a plane wave from a plane-parallel slab containing many raindrops with identical orientations.

sufficiently large $r = z + (x_1^2 + y_1^2)/2z$ and $r - z = (x_1^2 + y_1^2)/2r$ so that equation (3.51) becomes

$$E_R = E_0 \left[1 + S_{11}(0) \sum e^{-jk_0 \frac{(x_1^2 + y_1^2)}{2r}} \right] \quad (3.52)$$

If N is large the summation may be replaced by $\int N dx_1 dy_1 dz$ to yield

$$E_R = E_0 \left[1 - j \frac{2\pi}{k_0} N l S_{11}(0) \right] \quad (3.53)$$

The slab of drops can be replaced with a homogeneous material with complex refractive index $m = k'/k_0$. The field with the slab in place is

$$E_R = e^{-jk'l} \quad (3.54)$$

and with it removed

$$E_0 = e^{-jk_0 l} \quad (3.55)$$

Therefore, the presence of the medium decreases the field by

$$\frac{E_R}{E_0} = e^{-jk_0 l [(k'/k_0) - 1]} = e^{-jk_0 l (m-1)} \quad (3.56)$$

which for m close to unity reduces to

$$\frac{E_R}{E_0} = 1 - jk_0 l (m-1) \quad (3.57)$$

Comparing equations (3.53) and (3.57) it can be seen that

$$m = 1 + S_{11}(0) 2\pi N k_0^{-2} \quad (3.58)$$

or in terms of the propagation constant

$$k' = k_0 + S_{11}(0) 2\pi N k_0^{-1} \quad (3.59)$$

In general $S_{11}(0)$ will be complex so that $k' = k'_r - jk'_j$. The real part determines the phase lag of the wave travelling through the medium. In a distance l the phase changes by

$$\phi_1 = \frac{180}{\pi} k_r' l \quad \text{degrees.} \quad (3.60)$$

The imaginary part determines the attenuation of the wave in the medium. In a distance l the intensity decreases by

$$A_1 = 8.686 k_j' l \quad \text{dB} \quad (3.61)$$

For a plane wave of arbitrary polarization, resolved into linear components in the x_1 and y_1 directions, the relation between the incident and scattered wave is given by equation (3.21). It will be shown in Section (3.7) that in the case of scattering from an oblate spheroid $S_{12}=0$ so that

$$\begin{pmatrix} E_{x_1+} \\ E_{y_1+} \end{pmatrix}_{\text{After}}^{\text{scatterer}} = \begin{pmatrix} S_{11}(0) & 0 \\ 0 & S_{22}(0) \end{pmatrix} \begin{pmatrix} E_{x_1+} \\ E_{y_1+} \end{pmatrix}_{\text{Before}}^{\text{scatterer}} \quad (3.62)$$

If the identically oriented drops have a drop size distribution, then the propagation constants for the components of the field along the x_1 and y_1 axes are

$$k' = k_0 + \frac{2\pi}{k_0} \int S_{11}(0) N(D) dD \quad (3.63)$$

$$k'' = k_0 + \frac{2\pi}{k_0} \int S_{22}(0) N(D) dD \quad (3.64)$$

where $N(D) dD$ is the number of drops per unit volume with diameter between D and $D+dD$.

Except for spherical drops, $k' \neq k''$ and the component in the x_1 direction will attenuate and change phase at a rate different from the component in the y_1 direction. The differential attenuation in a path length l is

$$\Delta A = 8.686 l (k_j'' - k_j') \quad \text{dB} \quad (3.65)$$

and the differential phase shift is

$$\Delta \phi = \frac{180}{\pi} (k_r'' - k_r') \quad \text{degrees.} \quad (3.66)$$

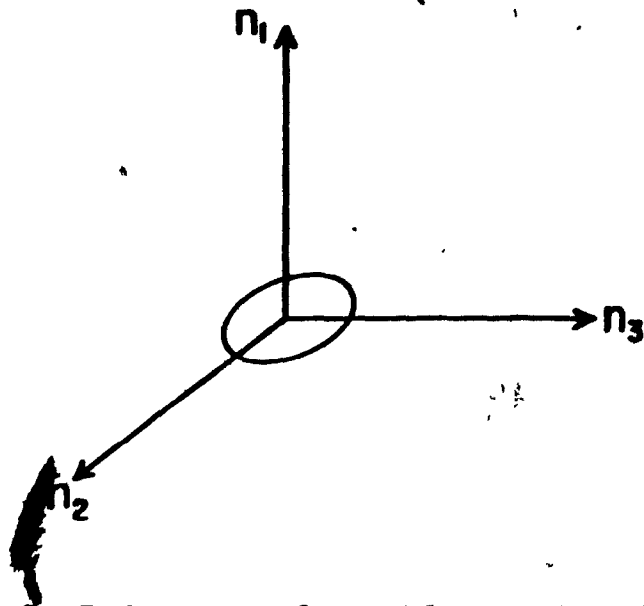


Fig. 3.5 Body axes of an oblate spheroid.

Recalling the expression for the propagation term

$$pe^{jX} = \tanh\left\{j\left(\frac{k''-k'}{2}\right)r\right\} \quad (3.67)$$

and substituting equations (3.65) and (3.66) into this expression yields

$$pe^{jX} = \tanh\left[0.0575\Delta A + j\frac{\pi}{360}\Delta\phi\right] \quad (3.68)$$

3.7 The Scattering Matrix Elements

The development in this section follows that of Atlas et al. (1953) and Van de Hulst (1957, ch. 6).

Consider an arbitrarily oriented water drop shaped like an ellipsoid. A coordinate system (n_1, n_2, n_3) is set up along the body axes of the drop as in Fig. 3.5. Resolving an incident wave into components along the body axes results in

$$\vec{E}_+ = E_{1+}\hat{n}_1 + E_{2+}\hat{n}_2 + E_{3+}\hat{n}_3 \quad (3.69)$$

where $\hat{n}_1, \hat{n}_2, \hat{n}_3$ are unit vectors in the direction of the axes. This incident wave sets up a dipole moment in the drop

$$\vec{p} = \alpha_1 E_1 \hat{n}_1 + \alpha_2 E_2 \hat{n}_2 + \alpha_3 E_3 \hat{n}_3 \quad (3.70)$$

where $\alpha_1, \alpha_2, \alpha_3$ are the polarizabilities of the drop along the body axes. In matrix form equation (3.70) is

$$\begin{pmatrix} p_1 \\ p_2 \\ p_3 \end{pmatrix} = \begin{pmatrix} \alpha_1 & 0 & 0 \\ 0 & \alpha_2 & 0 \\ 0 & 0 & \alpha_3 \end{pmatrix} \begin{pmatrix} E_{1+} \\ E_{2+} \\ E_{3+} \end{pmatrix} \quad (3.71)$$

At some distance r the scattered wave, according to Van de Hulst (1957, p. 64), is

$$\begin{pmatrix} E_{1-} \\ E_{2-} \\ E_{3-} \end{pmatrix} = k_0^2 \frac{e^{-jk_0 r}}{r} \begin{pmatrix} p_1 \\ p_2 \\ p_3 \end{pmatrix} \quad (3.72)$$

and substituting equation (3.71) into (3.72) yields

$$\begin{pmatrix} E_{1-} \\ E_{2-} \\ E_{3-} \end{pmatrix} = k_0^2 \frac{e^{-jk_0 r}}{r} \begin{pmatrix} \alpha_1 & 0 & 0 \\ 0 & \alpha_2 & 0 \\ 0 & 0 & \alpha_3 \end{pmatrix} \begin{pmatrix} E_{1+} \\ E_{2+} \\ E_{3+} \end{pmatrix} \quad (3.73)$$

The $n_1 n_2 n_3$ coordinate system can be related to the $x_2 y_2 z$ coordinate system by the orthogonal transformation

$$\begin{pmatrix} n_1 \\ n_2 \\ n_3 \end{pmatrix} = \begin{pmatrix} c_{1x} & c_{1y} & c_{1z} \\ c_{2x} & c_{2y} & c_{2z} \\ c_{3x} & c_{3y} & c_{3z} \end{pmatrix} \begin{pmatrix} x_2 \\ y_2 \\ z \end{pmatrix} = C \begin{pmatrix} x_2 \\ y_2 \\ z \end{pmatrix} \quad (3.74)$$

where c_{1x} is the direction cosine of the n_1 -axis with respect to the x_2 -axis etc. In terms of the components of the electric field the relationship is

$$\begin{pmatrix} E_1 \\ E_2 \\ E_3 \end{pmatrix} = C \begin{pmatrix} E_{x_2} \\ E_{y_2} \\ E_z \end{pmatrix} \quad (3.75)$$

Rewriting equation (3.73) in terms of the components in the $x_2 y_2 z$ coordinate system yields

$$\begin{pmatrix} E_{x_2-} \\ E_{y_2-} \\ 0 \end{pmatrix} = k_0^2 \frac{e^{-jk_0 r}}{r} C^T \begin{pmatrix} \alpha_1 & 0 & 0 \\ 0 & \alpha_2 & 0 \\ 0 & 0 & \alpha_3 \end{pmatrix} C \begin{pmatrix} E_{x_2+} \\ E_{y_2+} \\ 0 \end{pmatrix} \quad (3.76)$$

where $E_z = 0$ since propagation is along the z -axis. For spheroidal scatterers with n_1 along the symmetry axis $\alpha_2 = \alpha_3$, and equation (3.76) becomes

$$\begin{pmatrix} E_{x_2-} \\ E_{y_2-} \end{pmatrix} = k_0^2 \frac{e^{-jk_0 r}}{r} \begin{pmatrix} (\alpha_1 - \alpha_2) c_{1x}^2 + \alpha_2 & (\alpha_1 - \alpha_2) c_{1x} c_{1y} \\ (\alpha_1 - \alpha_2) c_{1x} c_{1y} & (\alpha_1 - \alpha_2) c_{1y}^2 + \alpha_2 \end{pmatrix} \begin{pmatrix} E_{x_2+} \\ E_{y_2+} \end{pmatrix} \quad (3.77)$$

Now the $x_2 y_2 z$ coordinate system was previously defined so that the symmetry axis, n_1 , lies in the $x_2 z$ plane and makes an angle β with the z -axis. Thus $c_{1x} = \sin\beta$ and $c_{1y} = 0$ so that

$$\begin{pmatrix} E_{x_2-} \\ E_{y_2-} \end{pmatrix} = k_0^2 \frac{e^{-jk_0 r}}{r} \begin{pmatrix} (\alpha_1 - \alpha_2) \sin^2 \beta + \alpha_2 & 0 \\ 0 & \alpha_2 \end{pmatrix} \begin{pmatrix} E_{x_2+} \\ E_{y_2+} \end{pmatrix} \quad (3.78)$$

This defines the scattering matrix with elements

$$\begin{aligned} S_{11} &= k_0^2 [(\alpha_1 - \alpha_2) \sin^2 \beta + \alpha_2] \\ S_{22} &= k_0^2 \alpha_2 \\ S_{12} &= S_{21} = 0 \end{aligned} \quad (3.79)$$

The $x_2 y_2 z$ coordinate system is related to the basic xyz coordinate system by the rotation defined in equation (3.22) so that for a spheroidal scatterer with $\beta = 90^\circ$

$$\begin{pmatrix} E_{x-} \\ E_{y-} \end{pmatrix}_{\text{at } r} = \frac{e^{-jk_0 r}}{r} R_2 \begin{pmatrix} k_0^2 \alpha_1 & 0 \\ 0 & k_0^2 \alpha_2 \end{pmatrix} R_2^T \begin{pmatrix} E_{x+} \\ E_{y+} \end{pmatrix}_{\text{scatterer}} \quad (3.80)$$

The polarizabilities α_1, α_2 are given by

$$\frac{V}{4\pi\alpha_i} = L_i + \frac{1}{m^2 - 1} \quad i = 1, 2 \quad (3.81)$$

where V is the volume of the drop; m^2 is the dielectric constant of the drop. For oblate spheroids the shape factor L_1 is given by Van de Hulst (1957, p. 71) as

$$\begin{aligned} L_1 &= \frac{1+f^2}{f^2} \left[1 - \frac{1}{f} \arctan f \right] \\ f^2 &= \left(\frac{b}{a} \right)^2 - 1, \quad L_2 = \frac{(1-L_1)}{2} \end{aligned} \quad (3.82)$$

where a is the length of the symmetry axis and b is the axis perpendicular to a .

3.8 Summary

In this chapter it has been shown that radiation, transmitted by a radar and scattered back to it by precipitation particles, is influenced by the propagation medium and by scattering from the particles. The observables W_1, W_2, W_3 and

W_i were related to the propagation and scattering effects. The observables can be manipulated to obtain information about the shape-CDR, orientation- α , and the fraction of scatterers with a preferred orientation- $|\rho|$. The scattering and propagation effects were related to the scattering matrix elements which were related to the polarizabilities of the particles.

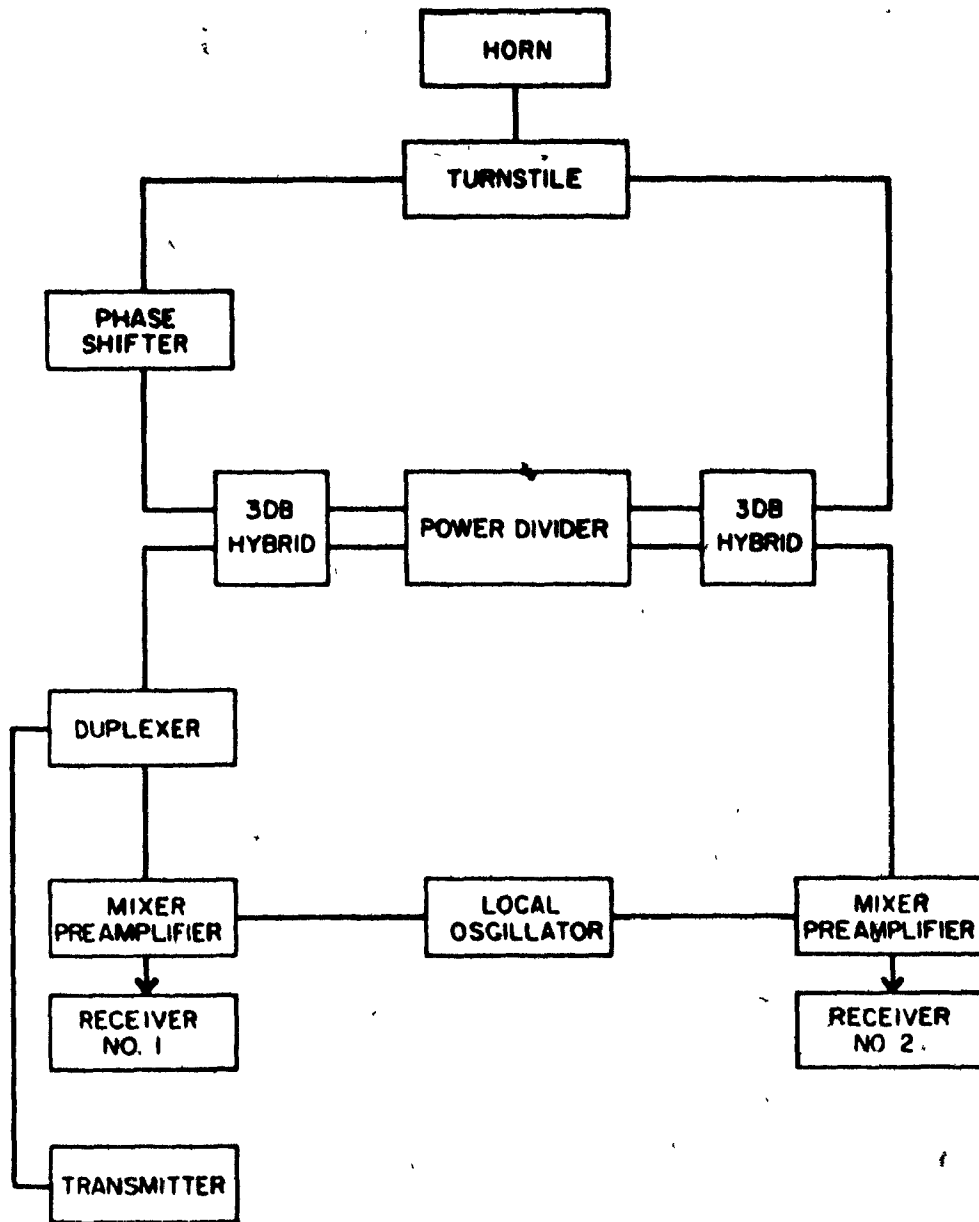


Fig. 4.1 Block diagram of the antenna microwave circuitry of the Alberta Hail Studies radar.

CHAPTER IV

THE RADAR FACILITIES

4.1 The Alberta Hail Studies Radar

All the data for this thesis were obtained with the Alberta Hail Studies radar.¹ This radar is equipped with a variable polarization antenna and a dual channel receiving system. The antenna is capable of transmitting elliptically polarized radiation of any chosen axial ratio and orientation. The received radiation is resolved by the antenna system into its main and orthogonal components. A complete description of the antenna is given by Allan et al. (1967) and by McCormick (1968). A block diagram of the antenna microwave circuit is shown in Fig. 4.1. The hybrid circuits and the power divider determine the shape and sense of rotation of the transmitted ellipse, the phase shifter determines the orientation of the transmitted ellipse. Normally the phase shifter is set to 0° and the microwave circuit is set to transmit LHC polarization. The received radiation is then resolved into RHC (main) and LHC (orthogonal) components. These components go into separate

¹ peak power	250 kw
pulse duration	1.75 μ sec
PRF	480 sec^{-1}
frequency	2.88 GHz
beam width	1.15° (all planes)
antenna gain	43.2 dB (at pedestal)
antenna rotation rate	8 RPM
elevation program	spiral scan: increases at .133° sec^{-1} to 8° or 20° with immediate return to 0°--complete cycle time 1.5 or 3 min.

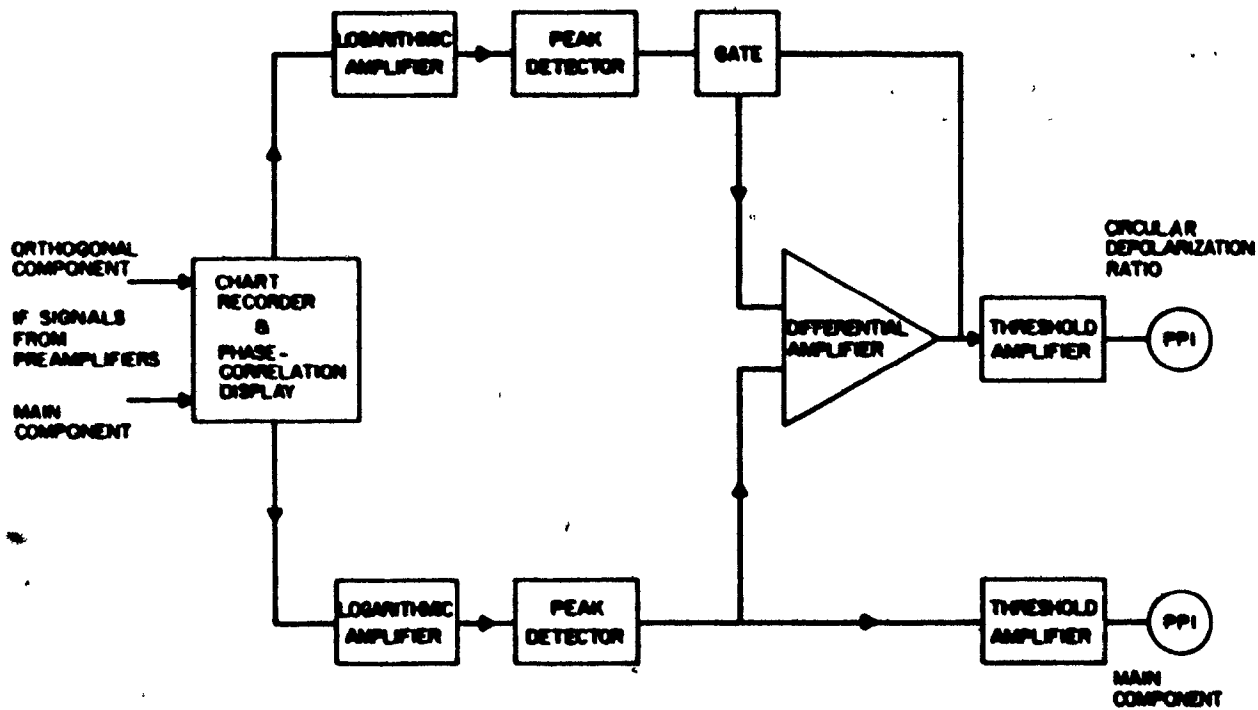


Fig. 4.2 Block diagram of the two channel receiving system.

receiving channels (see Fig. 4.2).

In each channel the IF signals from the preamplifiers are logarithmically amplified and the peak signal in each 0.7 mile range interval is detected and retained. The peak detected main signal is next passed through a threshold amplifier and converted to a grey shaded display. There are five levels of grey shade corresponding to 10 dB increments in the main signal. The darkest shade corresponds to powers between -90 to -80 dBm and the brightest shade corresponds to powers between -50 to -40 dBm.

To obtain a display of the CDR the peak detected main and orthogonal signals are differenced and the result is passed through a threshold amplifier and converted to a grey shaded display. There are five levels of grey shade, four of which correspond to 5 dB increments in the CDR from -25 dB to -5 dB. The other grey shade represents CDRs less than -25 dB. A gate ensures that the CDR is not displayed when the orthogonal signal is less than receiver noise. Both the main power and the CDR were displayed on PPI scopes which were continuously photographed with 35 mm cameras. The scopes were monitored with Polaroid cameras to maintain a consistent level of brightness. A description of the receiver system and calibration procedures is given by Barge (1972).

4.2 The Chart Recorder System

Until the summer of 1972 only the main power and the CDR were displayed on PPI scopes. To obtain the phase and

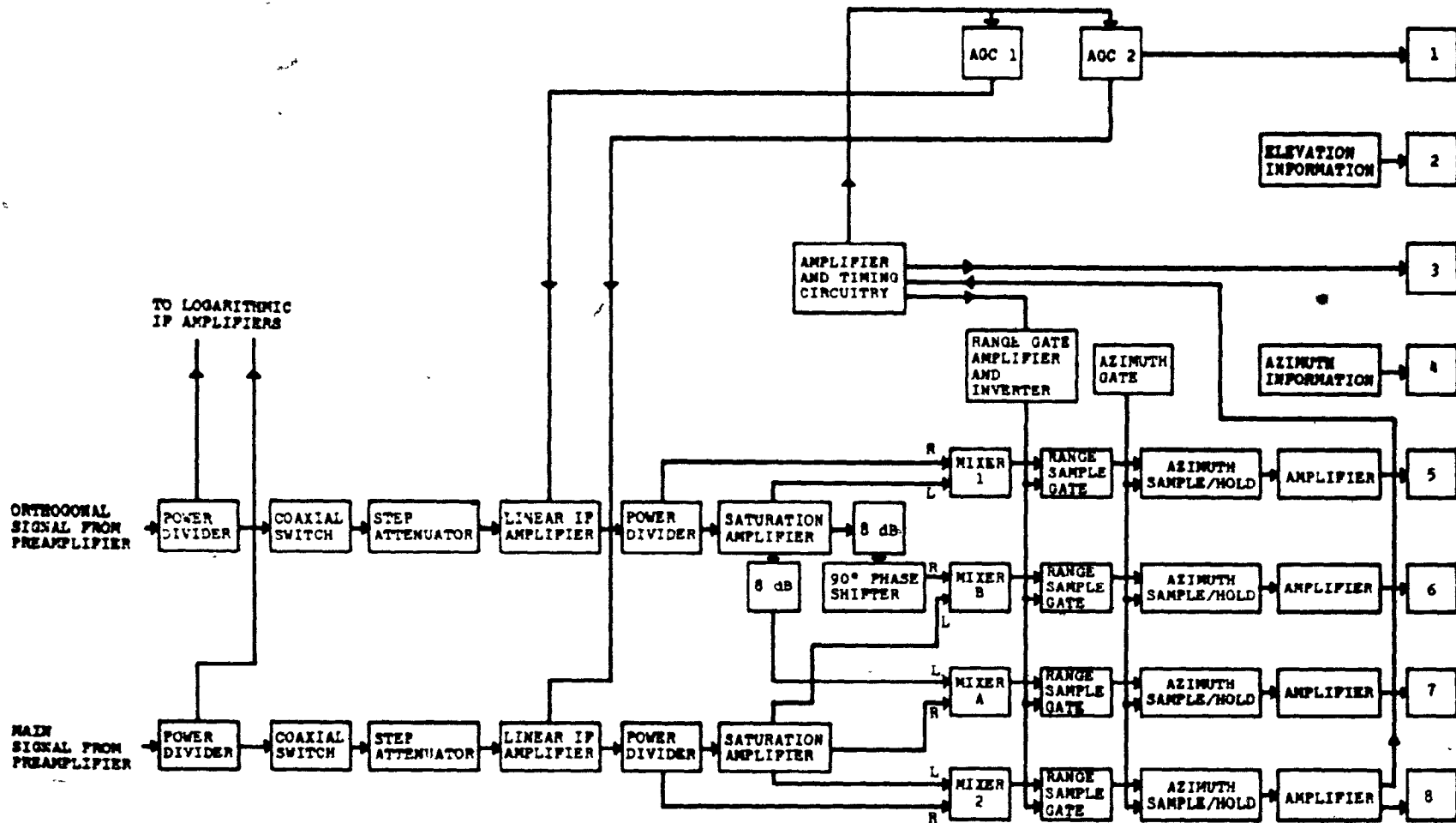


Fig. 4.3 Block diagram of the chart recorder system.

correlation information a chart recorder system was used. A block diagram of this system is shown in Fig. 4.3.

The signals from the preamplifiers first go through step attenuators into linear amplifiers. The attenuators as well as an automatic gain control prevent the linear amplifier from reaching saturation. The output from this stage goes through a two-way power divider with half the signal going to one of the inputs of a double balanced mixer and half going through a saturation amplifier. The output of the saturation amplifier has constant amplitude and a fixed phase relationship with the input.

For mixers 1 and 2 the reference input (L-port) is limited and the signal input (R-port) is proportional to the orthogonal or main component. The output of these mixers is

$$V = KE \cos\psi \quad (4.1)$$

where ψ is the phase angle between the two inputs; E is the amplitude of the signal at the R-port; K is a constant dependent on the mixer gain. The cable lengths are adjusted so that $\psi=0^\circ$ for the inputs of mixers 1 and 2, and therefore the outputs are

$$V_1 = K_1 E_1 \quad (4.2)$$

$$V_2 = K_2 E_2 \quad (4.3)$$

Thus V_1 and V_2 are the envelopes of the corresponding IF signals and therefore V_1^2 and V_2^2 are measures of the powers of the orthogonal and main components.

In the case of mixer A both inputs are limited and the output is

$$V_A = K_A \cos\theta \quad (4.4)$$

where θ is the phase difference between the main and orthogonal components. The input to the R-port of mixer B is shifted in phase by 90° so that the output is

$$V_B = K_B \sin \theta \quad (4.5)$$

Normally the chart recorder system is calibrated and adjusted so that $K_1 = K_2 = K_A = K_B$.

The outputs of the four mixers are fed into range gates and then into azimuth sample hold circuits. This allows the signals to be sampled and averaged within a specified range interval (usually 1 mile long) and azimuth interval (usually 1° wide) and then held for one revolution of the antenna. For the Alberta radar a range interval of 1 mile is equivalent to approximately 6 half-pulse lengths and 1° in azimuth contains 10 pulses spanning 21 milliseconds. Since the time required for the scatterers to shuffle from one array to another independent array is of the order of 10^{-2} second, the number of independent samples averaged by the range gate and azimuth sample hold circuits is probably between 12 and 24. This means that the measured average main and orthogonal powers are within ± 30 or 40 percent of the correct average powers 80 percent of the time. It is not known whether or not these limits also apply to the phase angle and correlation measurements.

When the antenna is not in a spiral scan but fixed for observations the azimuth sample hold circuitry is set to sample continuously. The four gated outputs along with range, elevation, azimuth, and automatic gain information are displayed on an eight-track chart recorder.

The chart recorder system has limitations in that information from only one small area of the storm is obtained during each revolution. Furthermore, these data must be reduced to obtain the standard polarization parameters and thus a real-time evaluation is not possible.

4.3 The Phase/Correlation PPI

For the summer of 1972, equipment developed by the National Research Council (Hendry and Allan, 1973) enabled the phase angle and correlation to be displayed on a PPI scope. The system was designed so that either the phase angle or the correlation could be displayed. Mixers A and B provide the signals so that when the display is turned on these two outputs are not available for the chart recorder.

The outputs from mixers A and B are averaged and the smoothed voltages may be written as

$$\bar{V}_A = KC \cos \theta \quad (4.6)$$

$$\bar{V}_B = KC \sin \theta \quad (4.7)$$

where K is a gain constant and C is related to the correlation. The correlation is then represented by displaying the voltage $\sqrt{\bar{V}_A^2 + \bar{V}_B^2}$ in five levels of grey shade. The brightest shade corresponds to correlations between 100 and 83% with the other shades representing correlations between 83 and 67%, 67 and 50%, 50 and 33%, and 33 and 17%. Correlations less than 17% are not displayed.

The phase angle is represented by displaying the voltage $\theta = \arctan(\bar{V}_B/\bar{V}_A)$ which is quantized into ten 36° sectors.

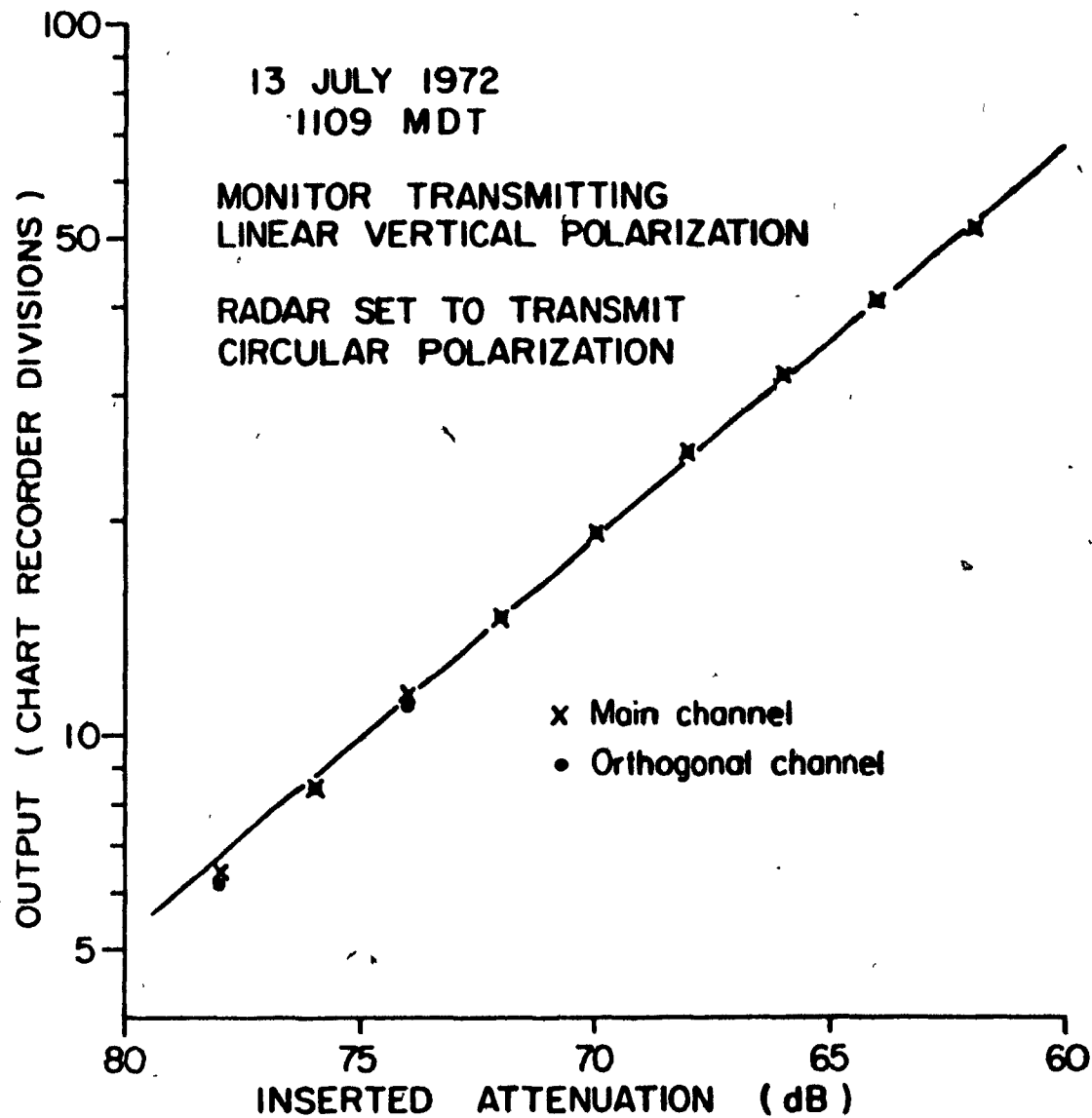


Fig. 4.4 Transfer characteristics of the main and orthogonal signal channels of the chart recorder system.

A selector switch enables any five sequential sectors to be displayed in five shades of grey. For example, if the selector switch is set to 0° the brightest shade corresponds to phase angles between 0 and 36° with the darkest corresponding to angles between 144 and 180° .

The PPI display of the correlation or phase angle was manually photographed with a standard single lens reflex 35 mm camera. As a result, the quantity of data obtained was adequate but not large.

4.4 Calibration

The calibration of the chart recorder and phase display was carried out with the aid of a remote transmitter, or monitor, situated on top of a 90 ft mast located 1300 ft from the radar. This monitor was capable of transmitting LHC or RHC polarization as well as linear polarization of any orientation.

To calibrate the main and orthogonal output channels of the chart recorder, equal signals are injected into the preamplifiers by setting the antenna to transmit circular polarization while the monitor is transmitting linear vertical polarization. The gains in the chart recorder system are adjusted so that the main and orthogonal channels have equal outputs for equal inputs. Since the monitor power is constant the transfer characteristics of the chart recorder are obtained by using the step attenuators (see Fig. 4.4). The power received from the monitor is determined by comparing its output at the

chart recorder with the signal injected by an RF generator into the waveguide of the antenna.

There are two methods of calibrating the phase angle outputs of the chart recorder and phase angle display. In the first method the antenna is set to transmit circular polarization while the monitor transmits linear vertical polarization. The RF phase shifter (see Fig. 4.1) is then rotated which changes the phase of one of the received components with respect to the other. The phase of the RF phase shifter is then recorded with the outputs of mixers A and B. The phase angle display chassis has ten lamps on the front panel corresponding to each of the ten 36° sectors. As the phase shifter is rotated it is only necessary to see that each of the ten lamps light up for the appropriate phase angle.

The second method entails setting the phase shifter to zero and rotating the monitor while it is transmitting linear polarization. The orientation of the monitor then corresponds to the orientation of a dipole scatterer. The monitor orientation is then recorded with the outputs of mixers A and B. Fig. 4.5 shows the mixer outputs for both types of calibration.

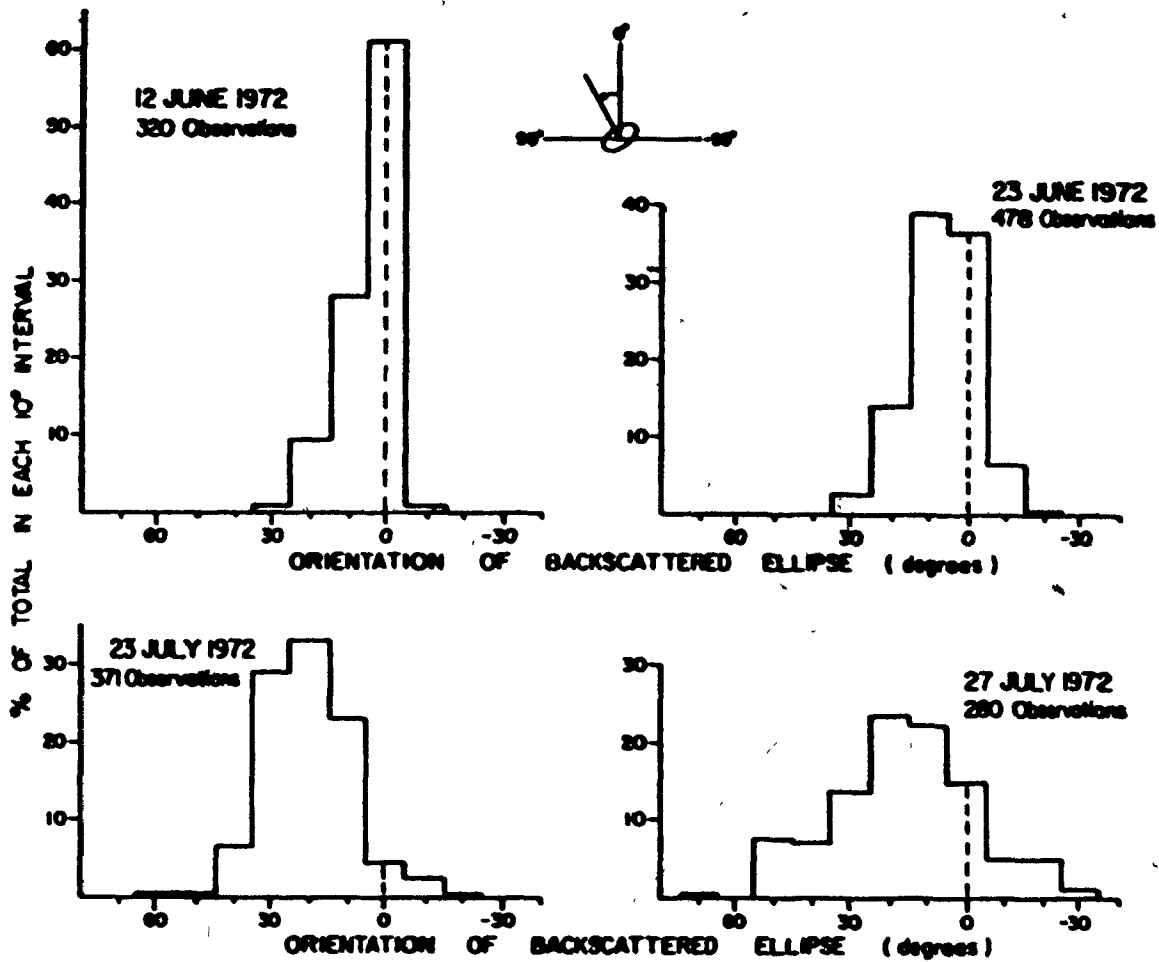


Fig. 5.1 Frequency distribution of orientations of the backscattered ellipse for observations above and below the melting level.

CHAPTER V

PROPAGATION

5.1 Phase Angle Observations

Frequency distributions of the orientation of the backscattered ellipse measured during four days in 1972 are shown in Fig. 5.1. The observations were made with the chart recorder system and measurements were obtained from many areas within the precipitation. The days of 12 June and 23 June 1972 were stratiform rain situations for which a bright band was observed on the PPI display. There were no reports of hail in the area where the data were taken. The days of 23 July and 27 July 1972 were convective situations with reports of hail.

The interesting feature is that the frequency distributions for the two days in June are centered close to an orientation angle of 0° whereas the distributions for the convective July days are shifted to about 20° .

At this point recall the following expression that was obtained in section 3.5

$$\frac{W_3 + jW_4}{W_2} = \rho_\alpha \bar{v}_e J(\bar{\delta} + 2\bar{\alpha}) + 2pe^{j(\chi + 2\tau)} \quad (5.1)$$

From this equation it was shown that the phase angle, which is related to the orientation of the backscattered ellipse, is given by $\theta = \arctan(W_4/W_3)$. Thus the orientation of the backscattered ellipse is a function of the mean orientation of the scatterers ($\bar{\alpha}$), the non-Rayleigh scattering phase shift ($\bar{\delta}$),

and propagation through an anisotropic medium (χ) with orientation τ .

Since the two days in June were stratiform rain situations for which the observed reflectivities were generally quite small it is reasonable to assume light to moderate rain was being observed. Furthermore, on 23 June 1972 a truck from the Alberta Hail Studies was measuring the rainfall rates directly under the region being sampled by the chart recorder system and the rainfall rates measured were never greater than 5.3 mm/hr. For this situation the propagation effects are expected to be small and since the raindrops satisfy the conditions for Rayleigh scattering theory at 3 GHz the differential phase shift upon scattering, δ , \approx zero. Therefore, the orientation of the backscattered ellipse for the two June days is the same as the mean orientation of the raindrops-- distributed narrowly about 0° . More evidence to support this conclusion is given in Chapter 6.

As previously mentioned the frequency distributions for 23 July and 27 July 1972 are shifted to about 20° . It seems unlikely that the shifted peak in the distributions is a result of the orientation of the scatterers because if positive orientations were measured when the storms were west of the radar then negative orientations would be expected when the storms were east of the radar. Such was not the case. Furthermore, these were convective showers containing hail so that propagation and non-Rayleigh scattering effects were probably present.

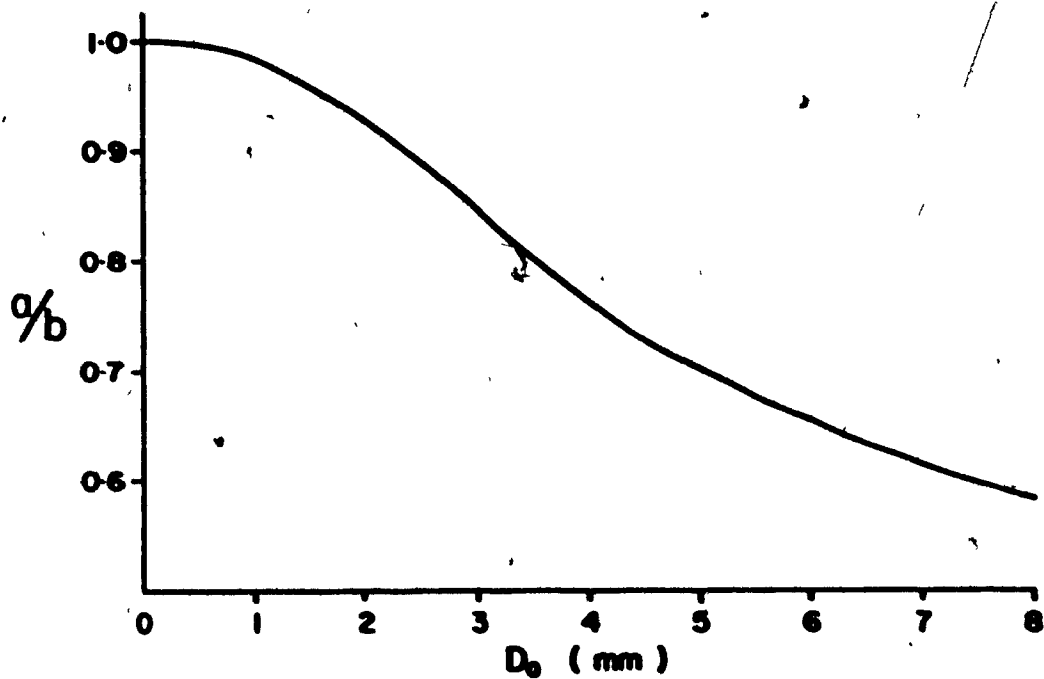


Fig. 5.2 Size-shape relationship for freely falling water drops. a/b is the axial ratio where a is the distance between the top and the silhouette base of the drop (the silhouette shape is the shape as it appears to an observer looking at the drop from the side) and b is the greatest width of the drop. D_0 is the equivalent diameter, defined as the diameter of a sphere with the same volume as the deformed drop. The curve is reproduced from Pruppacher and Pitter (1971).

The problem then, is to determine which effects contribute significantly to the phase angle, i.e. the orientation of the backscattered ellipse.

5.2 Calculations of the Propagation Effect

To determine whether propagation through rain could seriously influence 3 GHz circularly polarized radiation, Rayleigh theory calculations were made to determine the scattering matrix elements for raindrops. The drops were assumed to be oblate spheroids falling with their minor axes vertical ($\alpha=0^\circ$). The drop size distribution of Marshall and Palmer (1948) was used and the size-shape relationship was that of Pruppacher and Pitter (1971) (see Fig. 5.2). The dielectric constant primarily used in the calculations was that of water at 0°C ($79.0-j26.4$) although the values for water at 10°C and 20°C were used to check that there were not any significant changes in the results.

Once the scattering matrix elements were determined the effective propagation constants for various rainfall rates were calculated for vertical and horizontal linear polarizations. The difference in attenuation between the vertical and horizontal polarizations was then determined. This differential attenuation is shown in Fig. 5.3 as a function of the rainfall rate. It can be seen that even at a rain rate of 200 mm/hr the differential attenuation is only 0.024 dB/km and thus insignificant.

The difference in phase between the vertical and horizontal polarizations was calculated next. This differential

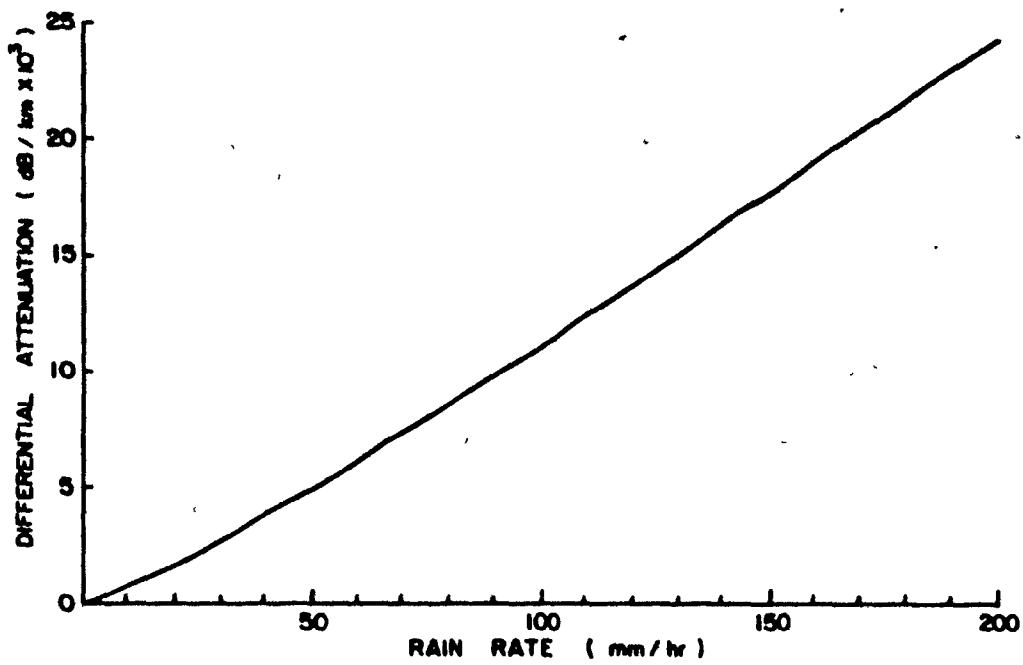


Fig. 5.3 The rain induced differential attenuation.

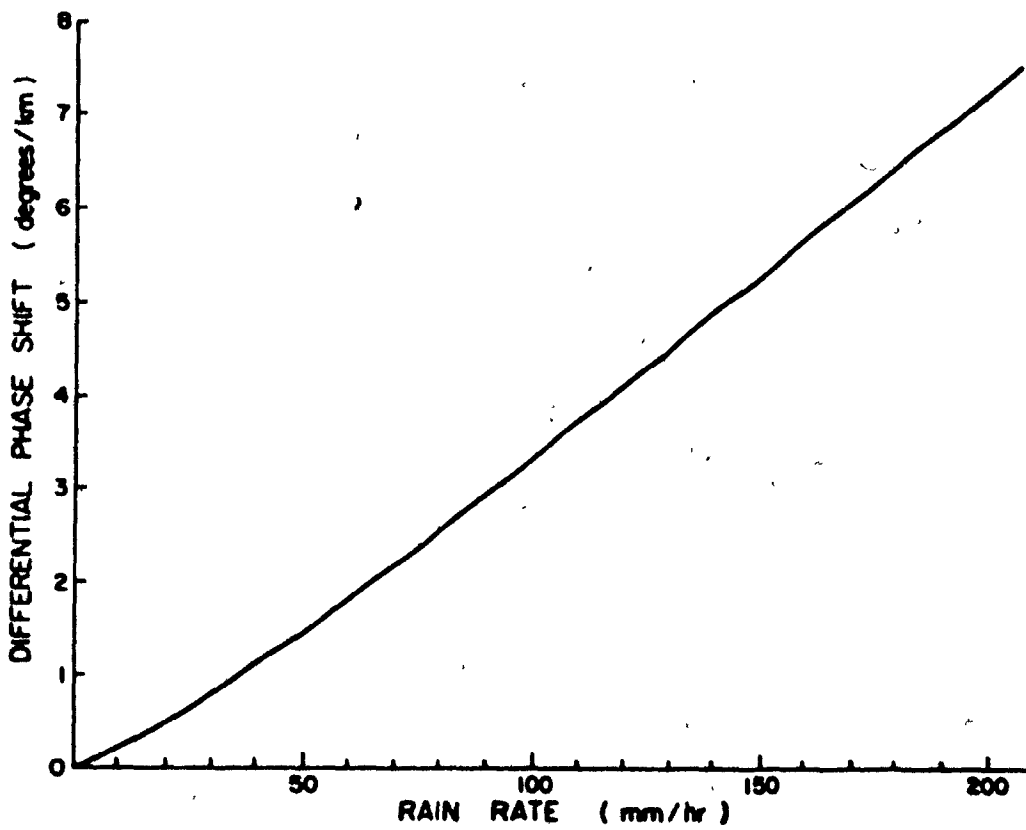


Fig. 5.4 The rain induced differential phase shift.

phase shift is shown in Fig. 5.4 where it can be seen that for large rainfall rates the differential phase shift is significant.

To understand how the rain induced differential phase shift can influence the polarization of the transmitted radiation consider a LHC polarized wave propagating through a region of uniform rain. Resolving the circular wave into vertical and horizontal components it can be seen in Fig. 5.5 that as the wave propagates through the rain the phase of the horizontal component will lag the phase of the vertical component. The result is that the wave becomes elliptical (LHE) with an orientation of 45° . When the total differential phase shift becomes 90° the wave will be linearly polarized. As the wave propagates even further it becomes elliptical again but with the opposite sense of rotation (RHE). Thus propagation through rain could alter the polarization of the wave to the extent that CDRs obtained from the back of the rain region would not be related to the shape of the scatterers.

To determine the effect of propagation on measurements of the CDR recall equation (3.44) for the case of Rayleigh scatterers ($\delta=0^\circ$) with orientation $\alpha=0^\circ$ and anisotropy orientation $\tau=0^\circ$ so that

$$\text{CDR} = \frac{1}{|v+2pe^{jX}|^2} \quad (5.2)$$

Since the rain induced differential attenuation is negligible equation (3.68) becomes

$$\begin{aligned} pe^{jX} &= \tanh\left[j\frac{\pi}{360}\Delta\phi\right] \\ &= j \tan\left[\frac{\pi}{360}\Delta\phi\right] \end{aligned} \quad (5.3)$$

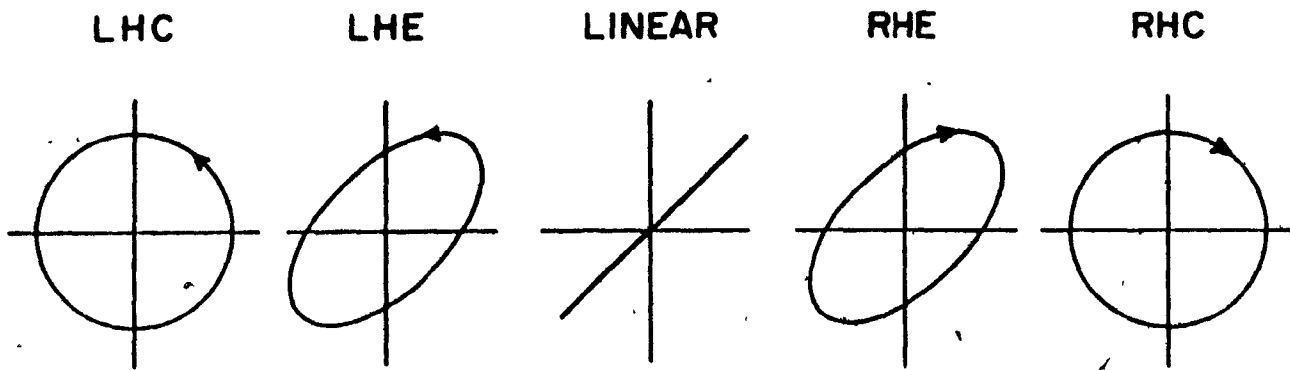


Fig. 5.5 Depolarization of a wave due to propagation through rain. Each figure represents the path traced out by the electric field vector, as viewed from the radar, at successive points in the rain region. The total differential phase shift increases for each successive figure (from left to right).

where $\Delta\phi$ is the total differential phase shift. Then equation (5.2) becomes

$$\text{CDR} = |\nu|^2 + 4\tan^2\left[\frac{\pi}{360}\Delta\phi\right] \quad (5.4)$$

Now consider the situation where the transmitted wave propagates through a region of heavy rain into a region of light rain. At the front of the heavy rain region the propagation term is negligible and the $\text{CDR} = |\nu|^2$. In the light rain on the far side the propagation term becomes dominant and the $\text{CDR} = 4\tan^2\left[\frac{\pi}{360}\Delta\phi\right]$.

To determine how propagation affects the phase angle consider equation (5.1) with $\alpha = \tau = \delta = 0^\circ$ so that

$$\begin{aligned} \frac{W_4}{W_2} &= \frac{W_3 + jW_4}{W_2} = \rho_\alpha \bar{\nu} + j \rho_\alpha \nu X \\ &= \rho_\alpha \bar{\nu} + 2j \tan\left[\frac{\pi}{360}\Delta\phi\right] \end{aligned} \quad (5.5)$$

At the front of the rain region when the propagation term is small ($\Delta\phi = 0^\circ$) $W_4/W_2 = 0$ and $\theta = \arctan(W_4/W_2) = 0^\circ$. As $\Delta\phi$ increases W becomes complex and $\theta > 0^\circ$. In the light rain at the far side of the precipitation region the drops are small and spherical so that $W_3/W_2 = 0$ and $\theta = 90^\circ$ with the result that the orientation of the backscattered ellipse is $\theta/2 = 45^\circ$. If further on in range the radiation again encounters heavy rain W_3/W_2 and W_4/W_2 will both be nonzero and $0 < \theta < 90^\circ$ so that the orientation of the backscattered ellipse will be between 0 and 45° .

In order to establish the sensitivity of the calculations of the differential phase shift to the drop size distribution a monodispersive distribution was used. For each

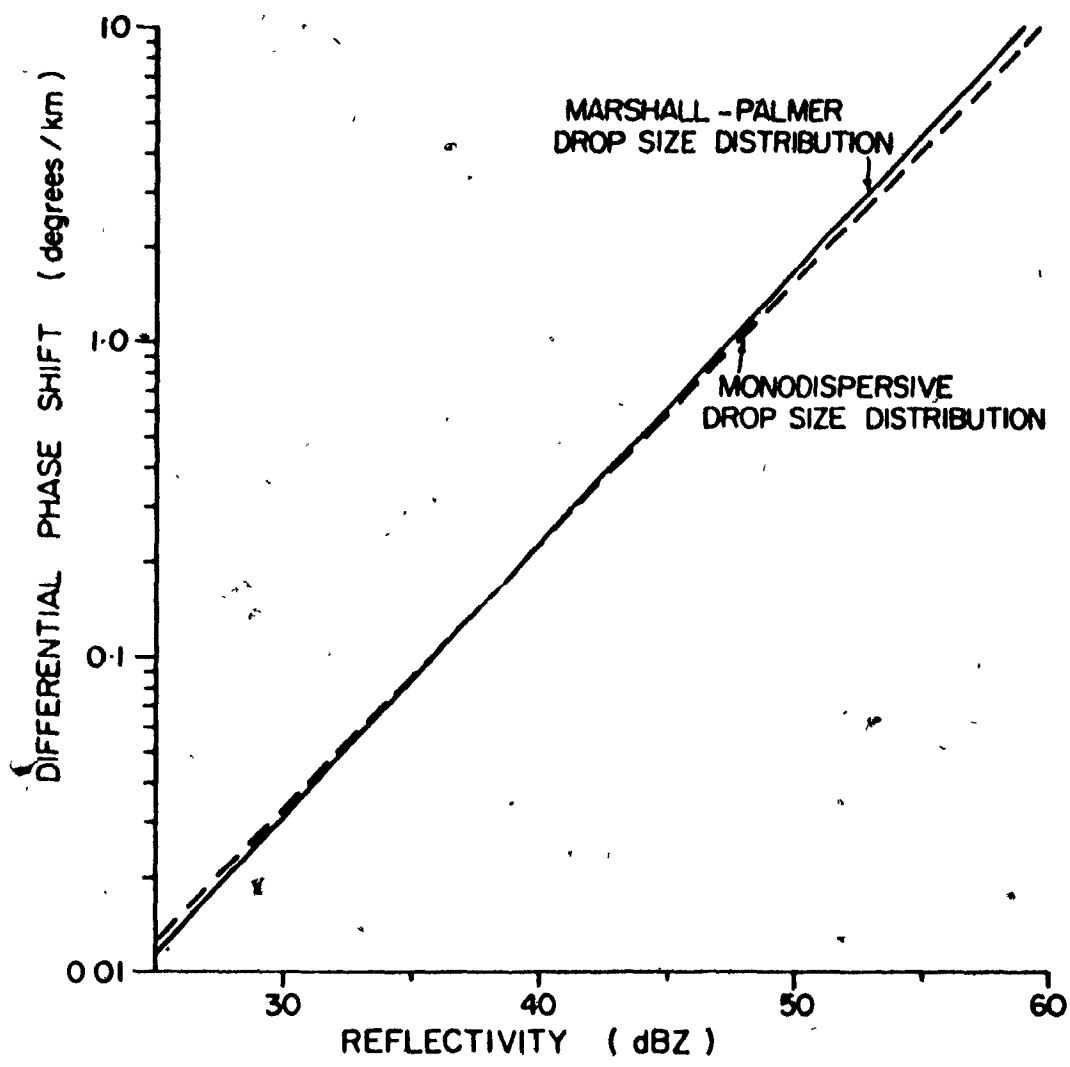


Fig. 5.6 The rain induced differential phase shift as a function of the reflectivity. The calculations were carried out for the drop size distribution of Marshall and Palmer (1948) (solid line) and for a monodispersive drop size distribution (dashed line).

rainfall rate the drop size was used which contributed the most to the reflectivity in the Marshall-Palmer distribution. The number of drops was increased so that the reflectivity was the same as for the Marshall-Palmer distribution. The results are shown in Fig. 5.6 and it can be seen that the sensitivity is not great.

5.3 The Storm of 27 July 1972

On 27 July 1972 a large thunderstorm developed northwest of the radar site and passed within 30 km to the north of the radar. The high reflectivity regions were on the side nearest the radar with the far side of the storm containing the low reflectivity regions. Plate I shows the main power PPI display at 1° elevation for 0146 MDT. The correlation PPI for this time (Plate III) shows that the high reflectivity regions had a high degree of correlation indicating that a large fraction of the scatterers had similar orientations. The situation was ideal for a propagation effect to be prominent. If indeed a propagation effect was present it would be expected that the orientation of the backscattered ellipse would be 0° on the front side of the storm and progress with range towards 45° in the low reflectivity regions on the back.

Plates IV and V show the phase angle PPI display for two different grey scale calibrations. In Plate IV three shades are visible. The darkest shade along the front of the storm corresponds to orientations of the backscattered ellipse between

0 and 18°. The next shade corresponds to orientations between 18 and 36° and the large area of the third, brightest, shade corresponds to orientations between 36 and 54°. In Plate V, which was taken 3 minutes after Plate IV, the grey scale calibration has been adjusted to emphasize the front edge of the storm. Now only the two brightest shades are visible with the darker one corresponding to orientations of the backscattered ellipse between 0 and 18° and the brightest corresponding to orientations between 18 and 36°. Therefore, the orientation does progress with range from 0 to 45° indicating the presence of a propagation effect. Plates VI, VIII, IX and X show the main power, correlation, and phase angle PPI displays for 0207 MDT.

To estimate the extent of the propagation effect several radial paths were chosen through the storm. The grey shades along each of the paths were noted from the main power PPI and the corresponding reflectivities were determined. Since the grey shades are in 10 dB steps the reflectivities were calculated for the upper and lower limits of each shade displayed so that estimates could be obtained of the maximum and minimum propagation effects through rain.

The reflectivities were related to the rainfall rate by the relationship of Marshall and Palmer (1948)

$$Z_e = 220R^{1.6} \quad (5.6)$$

where Z_e is in mm^6m^{-3} and R is in mmhr^{-1} . Then based on the drop size distribution of Marshall and Palmer (1948) and the size-

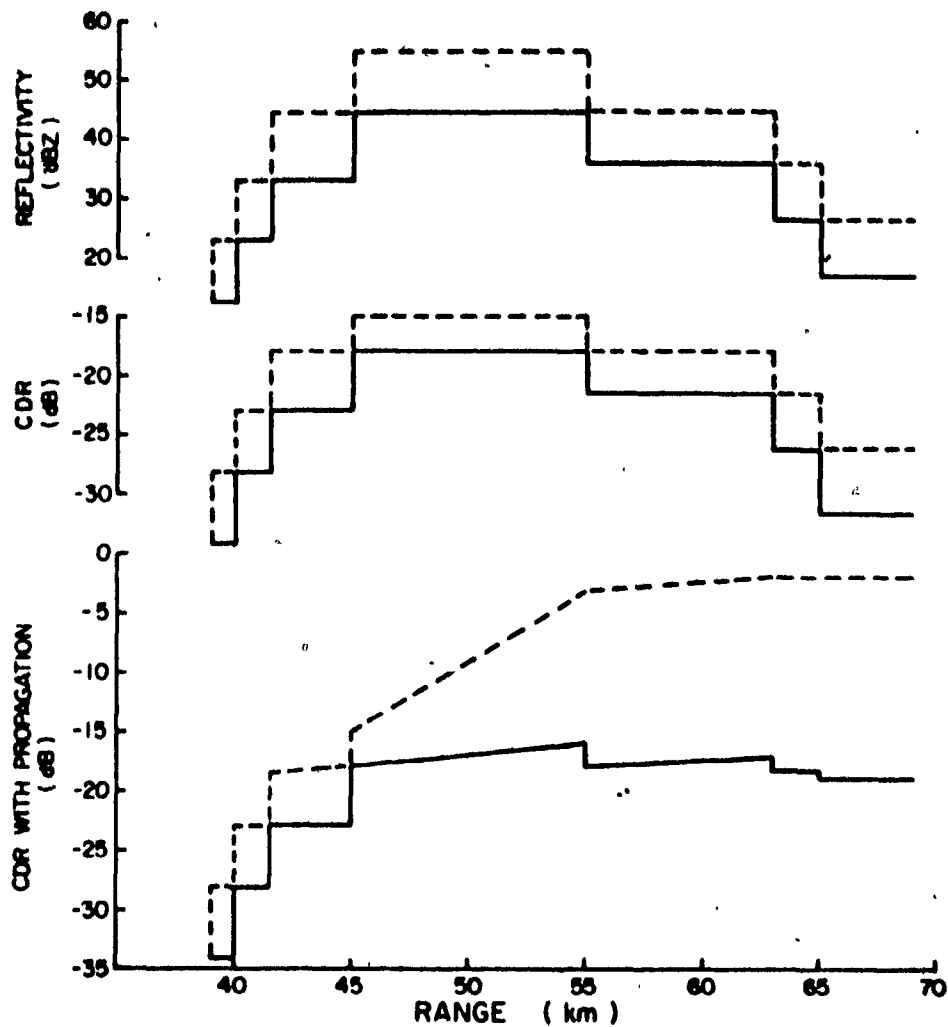


Fig. 5.7 Calculations of the intrinsic CDR and the CDR with the propagation term included, along a radial path at 350° azimuth for 0146 MDT-27 July 1972. The calculations were based on the upper (dashed) and lower (solid) limits of the reflectivity along the path as determined from the main power PPI at 1° elevation.

shape relationship of Pruppacher and Pitter (1971) the CDRs were calculated along each path without the propagation term. These will be called the intrinsic CDRs and are related directly to the shape of the scatterers. The CDRs were then calculated with the propagation term included. The results for a path through one intense region of the storm at 0146 MDT and for paths through two intense regions at 0207 MDT are shown in Figs. 5.7, 5.8, and 5.9.

It can be seen that the upper and lower estimates of the intrinsic CDR drop to -25 dB or less in the low reflectivity regions at the back of the storm. However, when the propagation term is included even the lower estimates of the CDR are greater than -20 dB. Observing the CDR display shown in Plate II, for 0146 MDT, and VII, for 0207 MDT, it is seen that once the beam has passed through the high reflectivity regions at 350° azimuth, at 0146 MDT, and at 5 and 25° azimuth, at 0207 MDT, the CDRs do not drop below -10 dB even in the low reflectivity regions.

An interesting feature is the notch surrounded by bright shade between 35 and 45 miles at 350° azimuth in Plate II and at 5° azimuth in Plate VII. This could possibly be a region where the propagation effect has accumulated to the point that the CDR exceeded -5 dB and hence was not displayed since the brightest shade of the grey scale corresponds to CDRs between -10 and -5 dB. In Plates II and VII it can be seen that the notch is along a radial line from the radar. Furthermore, the development of the notch coincided with the development of the

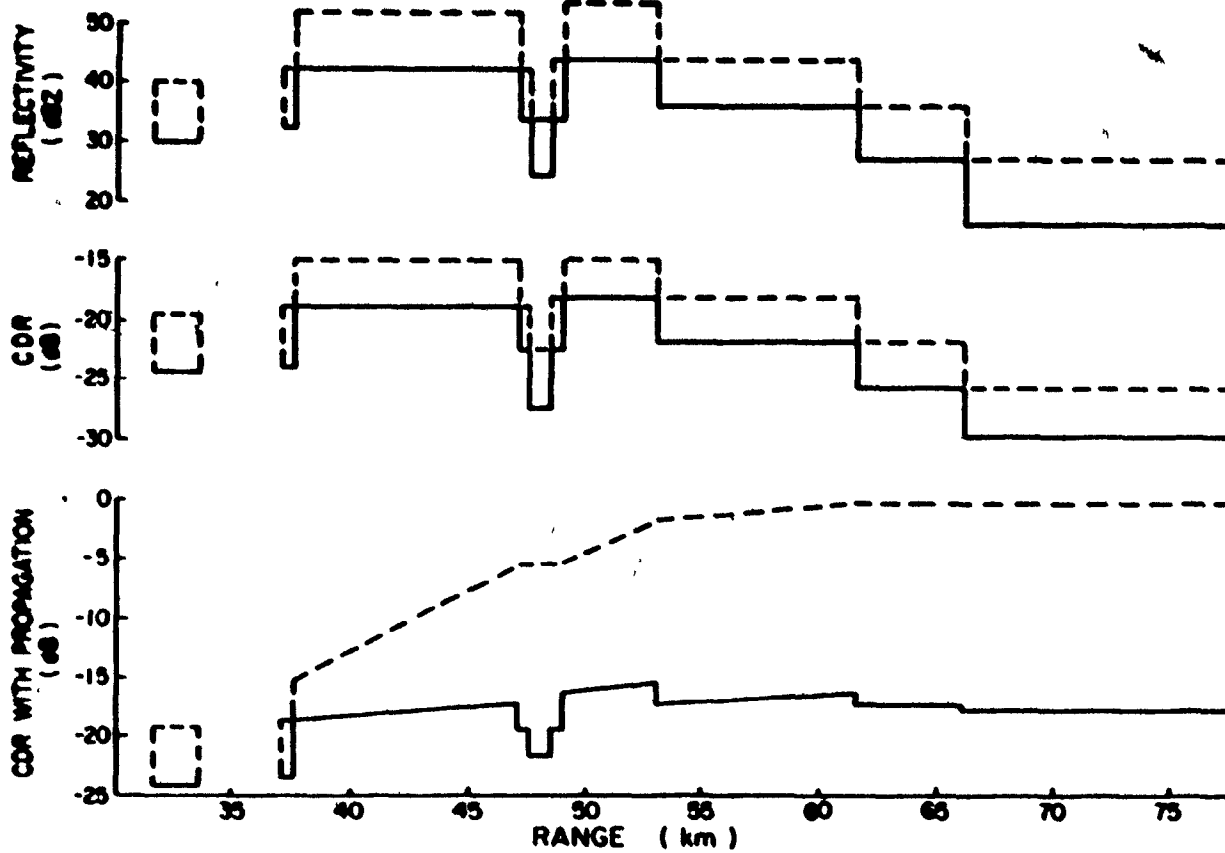


Fig. 5.8 Same as Fig. 5.7 except at 5° azimuth for 0207 MDT-27 July 1972.

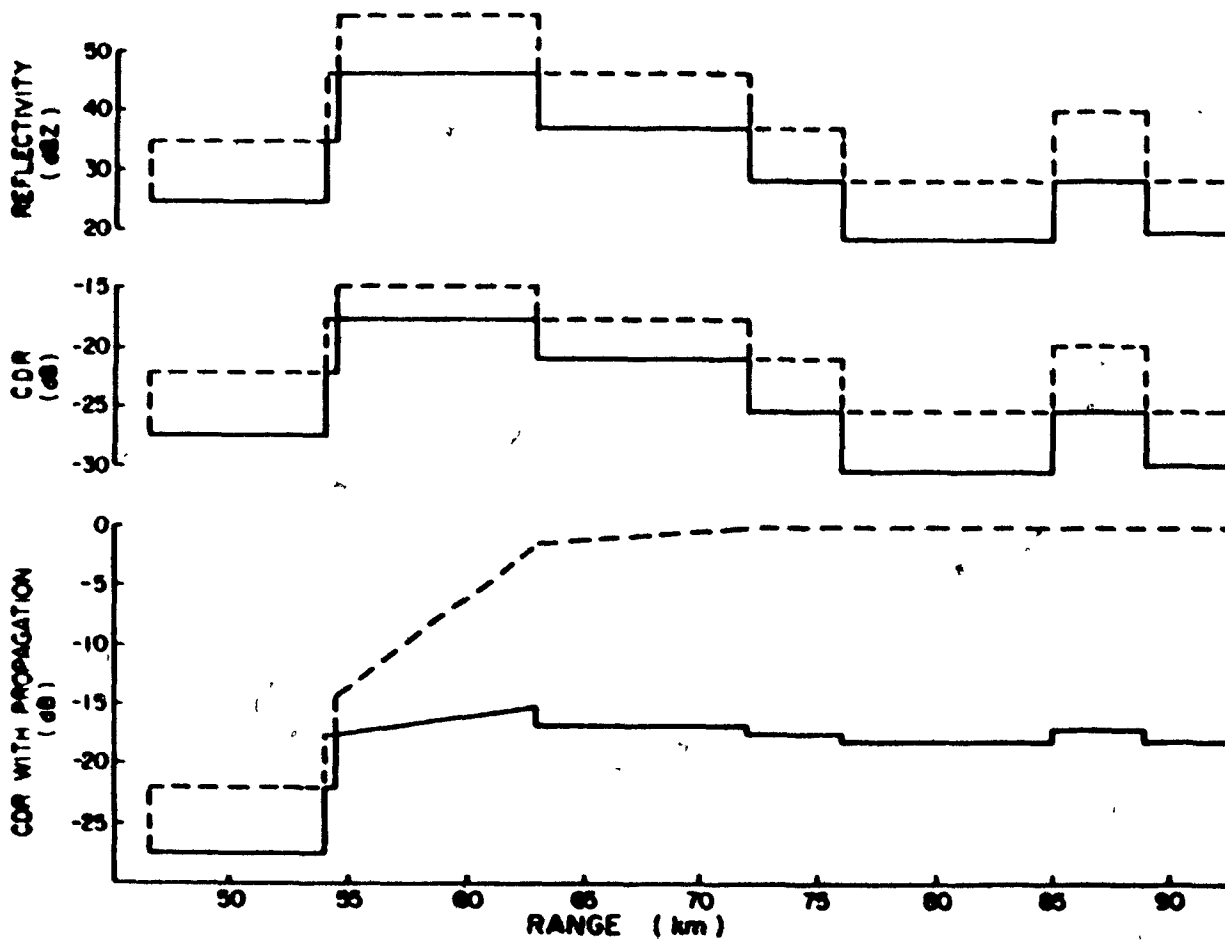


Fig. 5.9 Same as Fig. 5.7 except at 25° azimuth for 0207 MDT-27 July 1972.

high reflectivity region directly between it and the radar. If this interpretation of the notch is correct then this is an example of a very large propagation effect. Regardless of the notch there is strong evidence of a significant propagation effect. Therefore, observations and theoretical calculations indicate that at 3 GHz circularly polarized transmitted radiation can be significantly depolarized by propagation through heavy precipitation.

5.4 Propagation Through Hail

The extent that propagation through hail may alter the polarization of the beam is a difficult problem to solve. Whereas raindrops may be dealt with by Rayleigh scattering theory for 3 GHz radiation, scattering by hailstones must be handled with Mie theory.

Unpublished scattering amplitudes for a collection of hailstones have been calculated by Oguchi³. The stones were assumed to be oblate spheroids of ice at 0°C. The difficulty with applying these calculations to the propagation problem is that the number density of the hailstones is not known nor is there a simple size-shape relationship for hailstones as there is for raindrops.

Table 5.1 lists the maximum and minimum dimensions of the oblate hailstones for which the calculations were made along

³ These calculations were passed on to the author by Dr. G.C. McCormick.

with the differential phase shift and attenuation. To obtain the differential phase shift and attenuation for each hailstone a number density of one stone per cubic meter was assumed. English (1972) estimates that for large hailstones such as those in Table 5.1 the number density is between 10^{-1} and 10^{-2} m^{-3} . If these estimates are used then the differential phase shifts and attenuations are reduced by a factor of 10 to 10^2 . The results indicate that it is possible for hail to significantly alter the polarization of radiation by propagation effects. Note that for hailstone (2) even the differential attenuation is large.

TABLE 5.1. The minimum and maximum diameters of four hailstones and their corresponding differential phase shift and attenuation at 3 GHz based on scattering amplitudes calculated by Oguchi for oblate spheroids of ice at 0°C. The number density was assumed to be one hailstone per cubic meter.

	MINIMUM DIAMETER (cm)	MAXIMUM DIAMETER (cm)	DIFFERENTIAL PHASE SHIFT (deg/km)	DIFFERENTIAL ATTENUATION (dB/km)
(1)	3.05	3.71	6.7	0.6
(2)	2.54	4.11	160.4	14.4
(3)	2.16	3.30	80.2	4.0
(4)	1.27	1.91	12.0	0.1

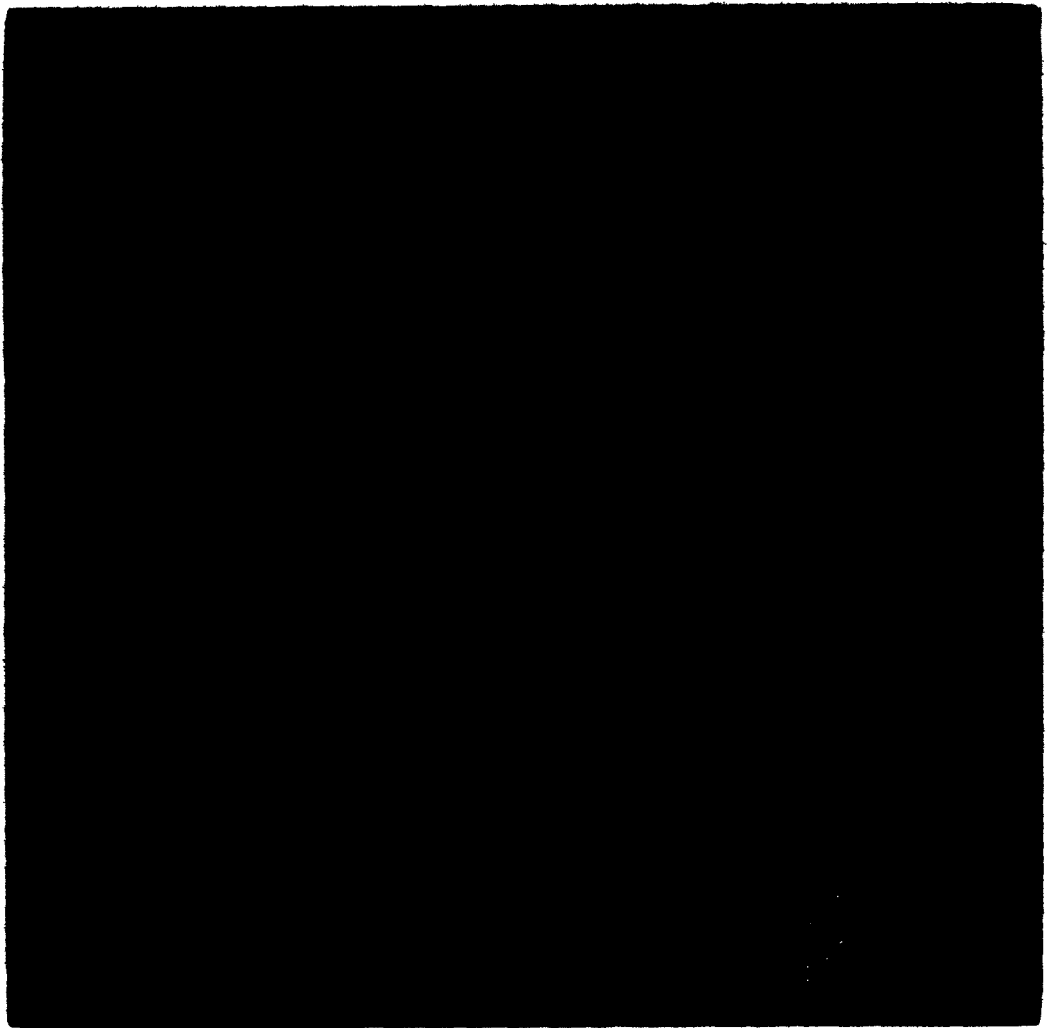


PLATE I.

Main power PPI at 1° elevation for 0146 MDT-27 July 1972. The grey shade scale is in 10 dB steps with the darkest shade corresponding to values between -90 and -80 dBm and the brightest to values between -50 and -40 dBm. The range rings are at 10 mile (=16.1 km) intervals.

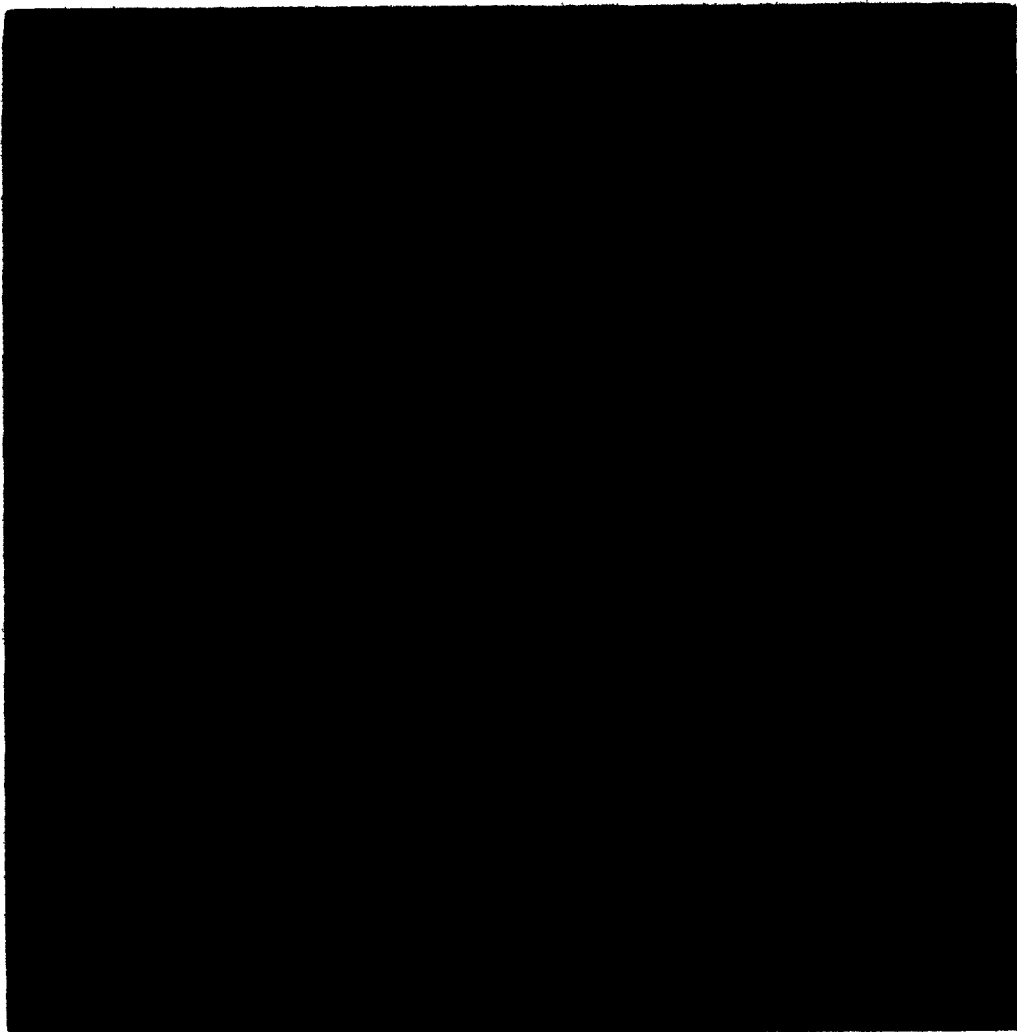


PLATE II. PPI display of the CDR at 1° elevation for 0146 MDT-27 July 1972. The grey shade scale is in 5 dB steps with the darkest shade corresponding to values of the CDR less than -25 dB and the brightest to values between -10 and -5 dB. The range rings are at 10 mile (=16.1 km) intervals. At 80 miles is an azimuth display of attenuation (Zawadzki and Rogers, 1969).

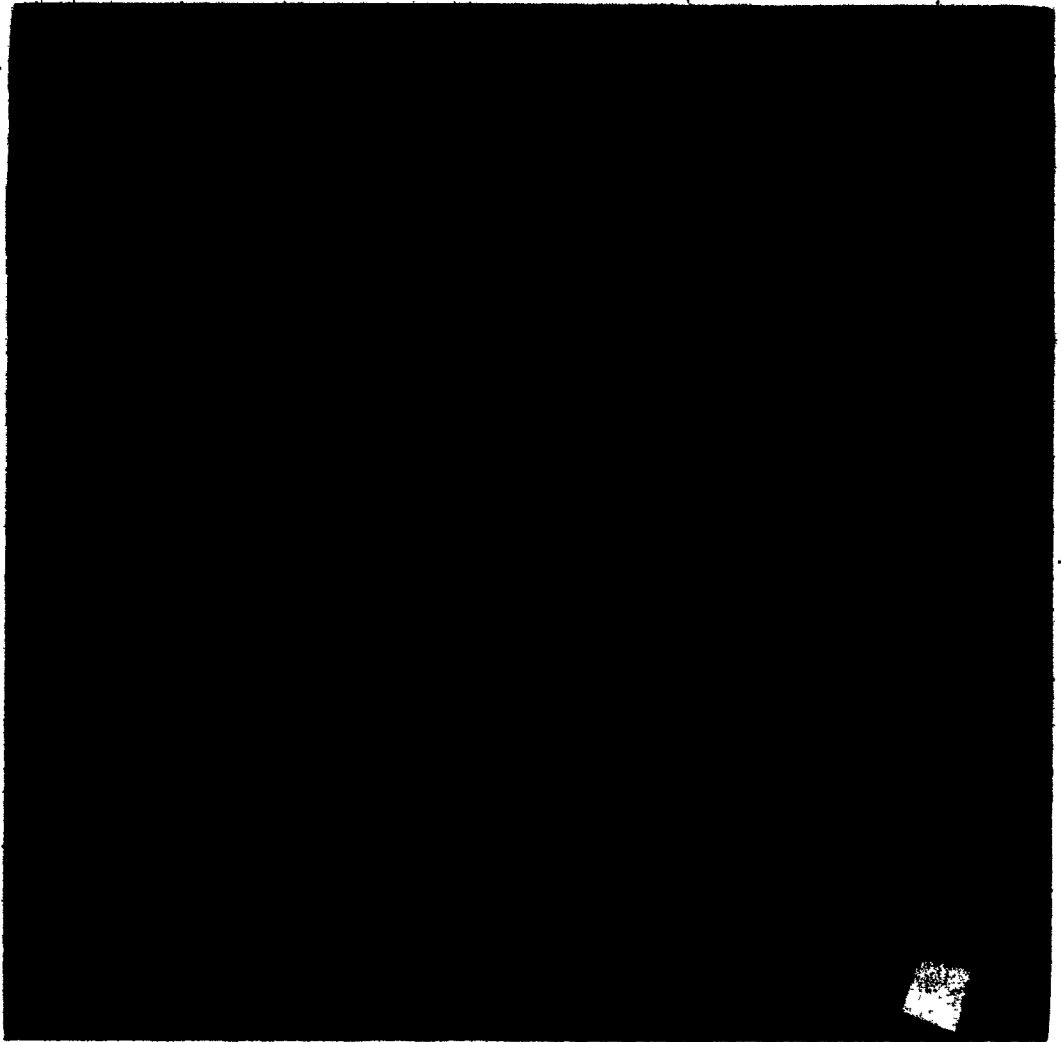


PLATE III. PPI display of the correlation at 1° elevation for 0146 MDT-27 July 1972. The darkest shade of the grey shade scale corresponds to correlations between 17 and 33%. The other shades correspond to correlations between 33 and 50%, 50 and 67%, 67 and 83%, with the brightest 83 and 100%. The range rings are at 10 mile (≈ 16.1 km) intervals.

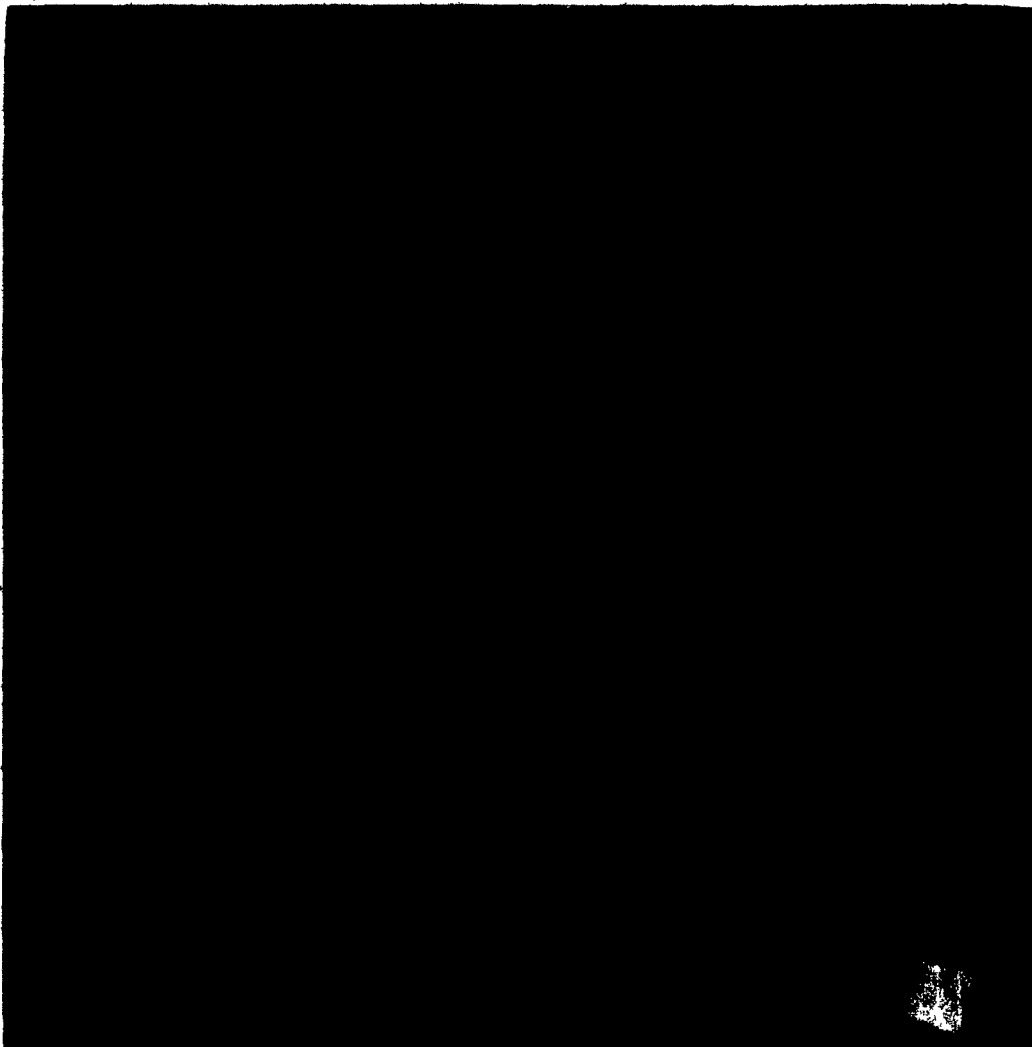


PLATE IV. Phase angle PPI at 1° elevation for 0149 MDT-27 July 1972. The darkest shade of the grey shade scale corresponds to orientations of the minor axis of the backscattered ellipse between 0 and 18°. The other shades correspond to orientations between 18 and 36°, 36 and 54°, 54 and 72°, with the brightest 72 and 90°. The orientations of the minor axis of the backscattered ellipse are measured counterclockwise from the vertical as viewed from the radar. The range rings are at 10 mile (=16.1 km) intervals.

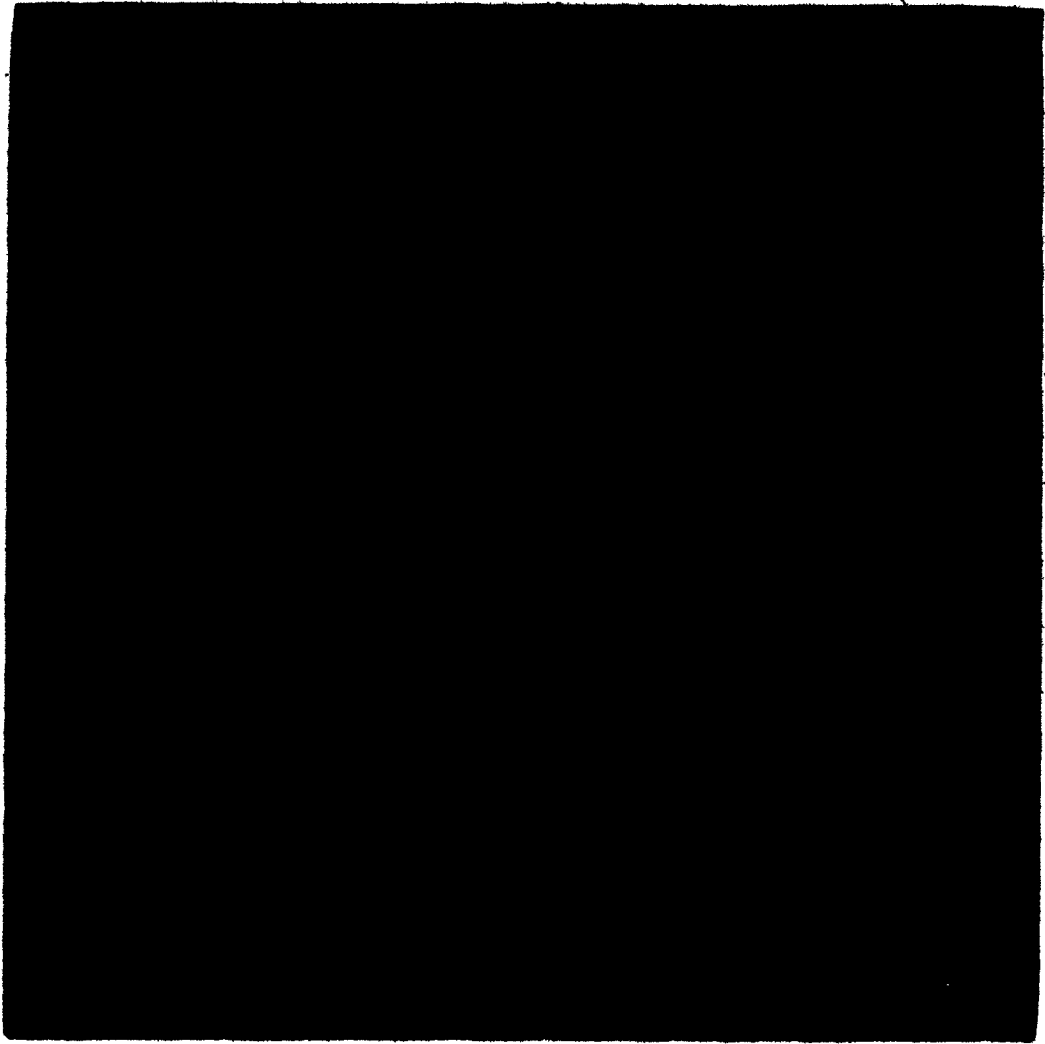


PLATE V.

Phase angle PPI at 1° elevation for 0152 MDT-27 July 1972. The grey shade scale has been adjusted so that the darkest shade corresponds to orientations of the minor axis of the backscattered ellipse between -54 and -36° . The other shades correspond to orientations between 36 and -18° , -18 and 0° , 0 and 18° , with the brightest 18 and 36° . The orientations of the minor axis of the backscattered ellipse are measured counterclockwise from the vertical as viewed from the radar. The range rings are at 10 mile (≈ 16.1 km) intervals.

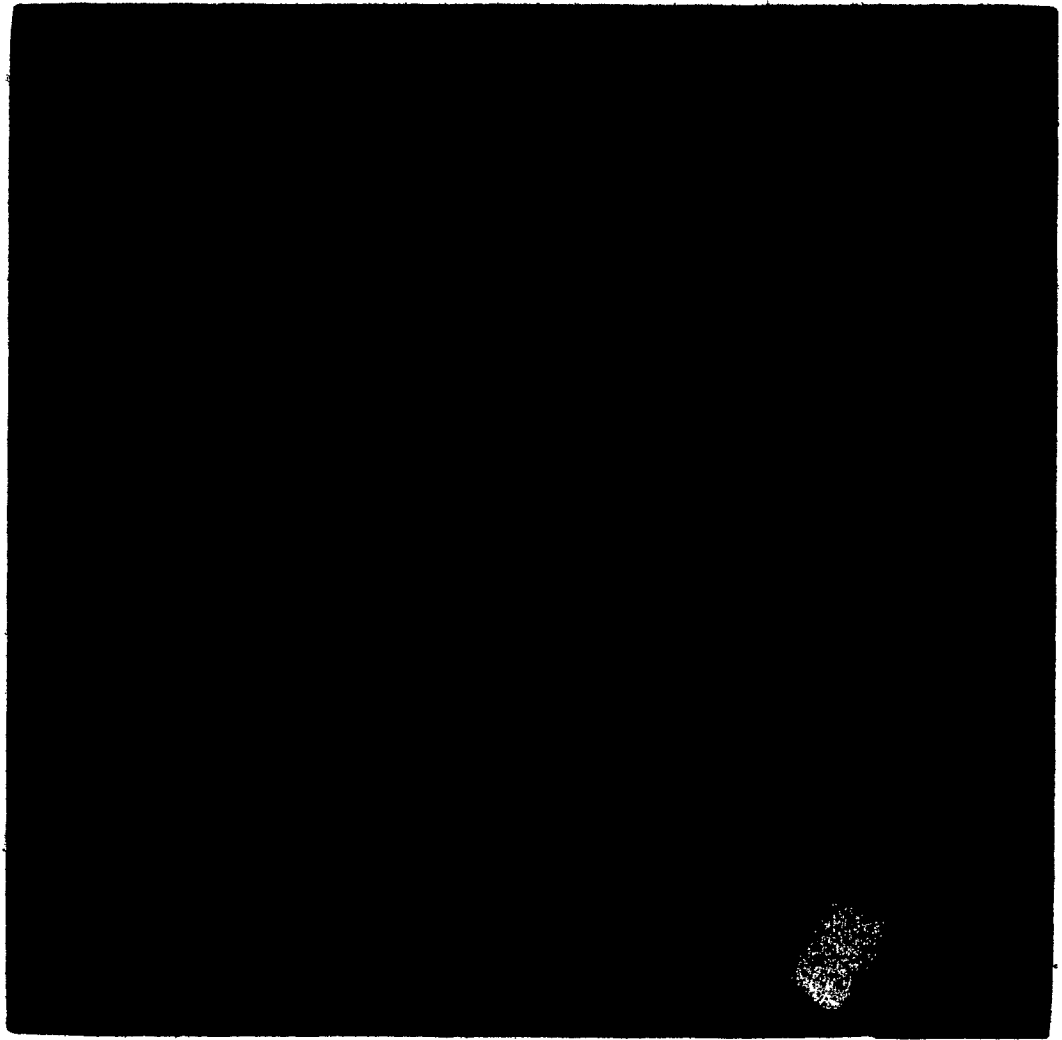


PLATE VI. Main power PPI at 1° elevation for 0207 MDT-
27 July 1972. The grey shade scale is in 10 dB
steps with the darkest shade corresponding to
values between -90 and -80 dBm and the brightest
to values between -50 and -40 dBm. The range
rings are at 10 mile (≈16.1 km) intervals.

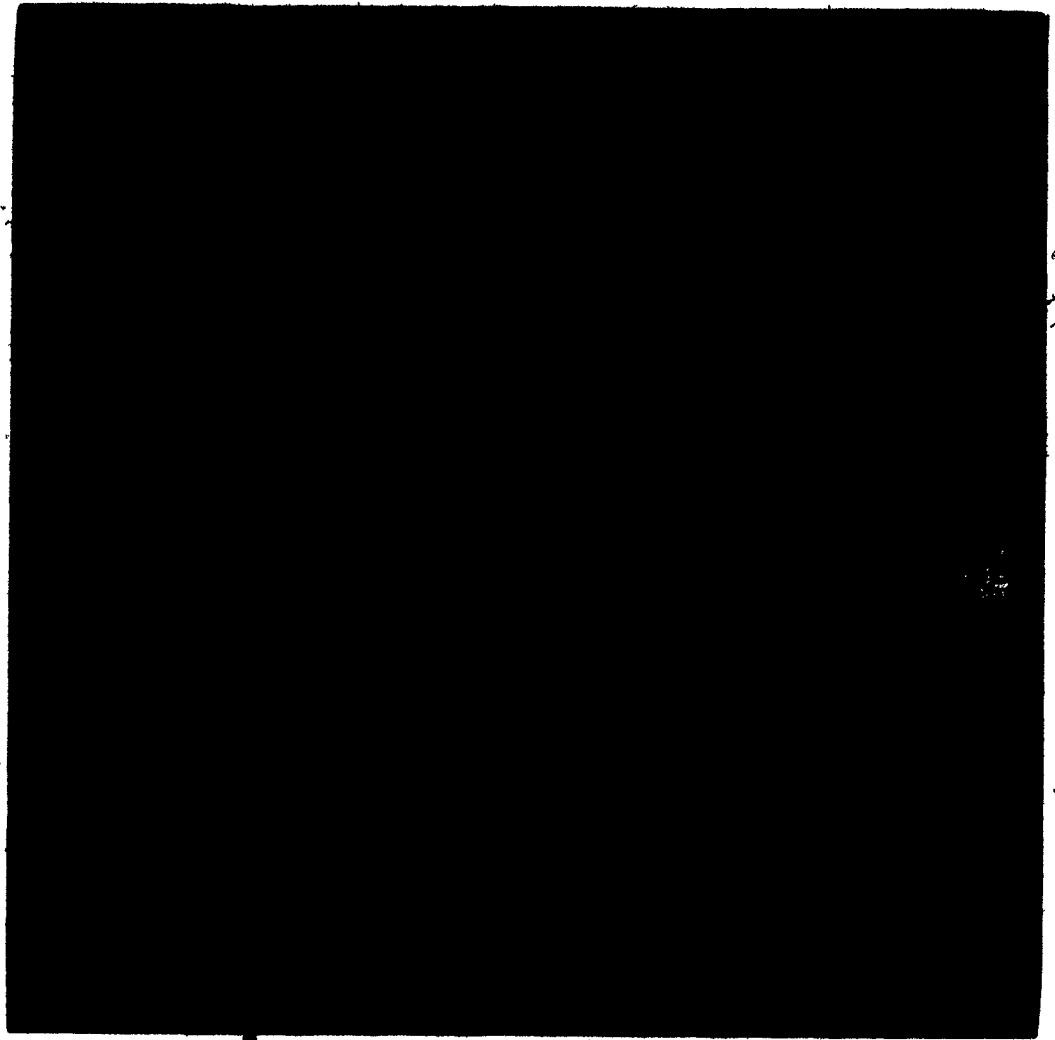


PLATE VII. PPI display of the CDR at 1° elevation for 0207 MDT-27 July 1972. The grey shade scale is in 5 dB steps with the darkest shade corresponding to values of the CDR less than -25 dB and the brightest to values between -10 and -5 dB. The range rings are at 10 mile (≈ 16.1 km) intervals.

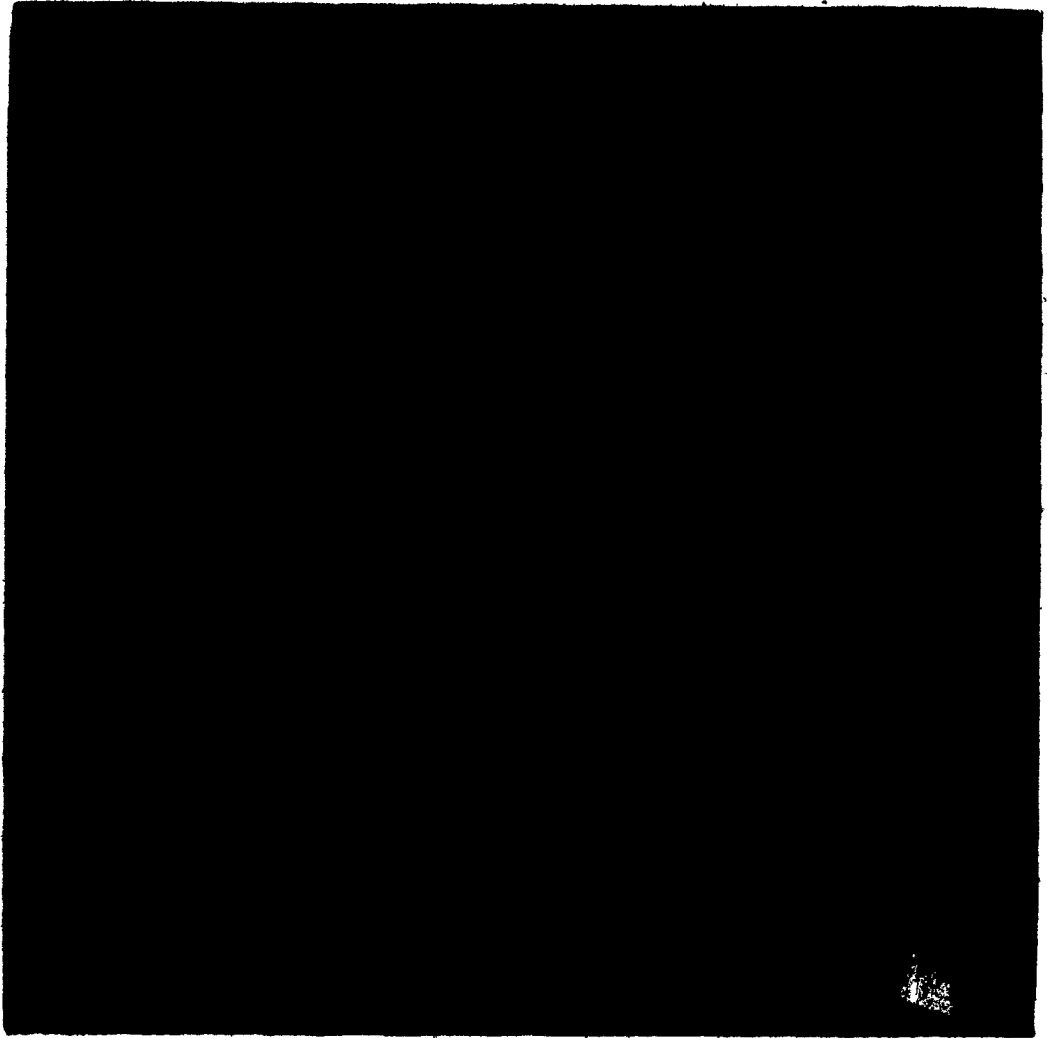


PLATE VIII. PFI display of the correlation at 1° elevation for 0207 MDT-27 July 1972. The darkest shade of the grey shade scale corresponds to correlations between 17 and 33%. The other shades correspond to correlations between 33 and 50%, 50 and 67%, 67 and 83%, with the brightest 83 and 100%. The range rings are at 10 mile (=16.1 km) intervals.

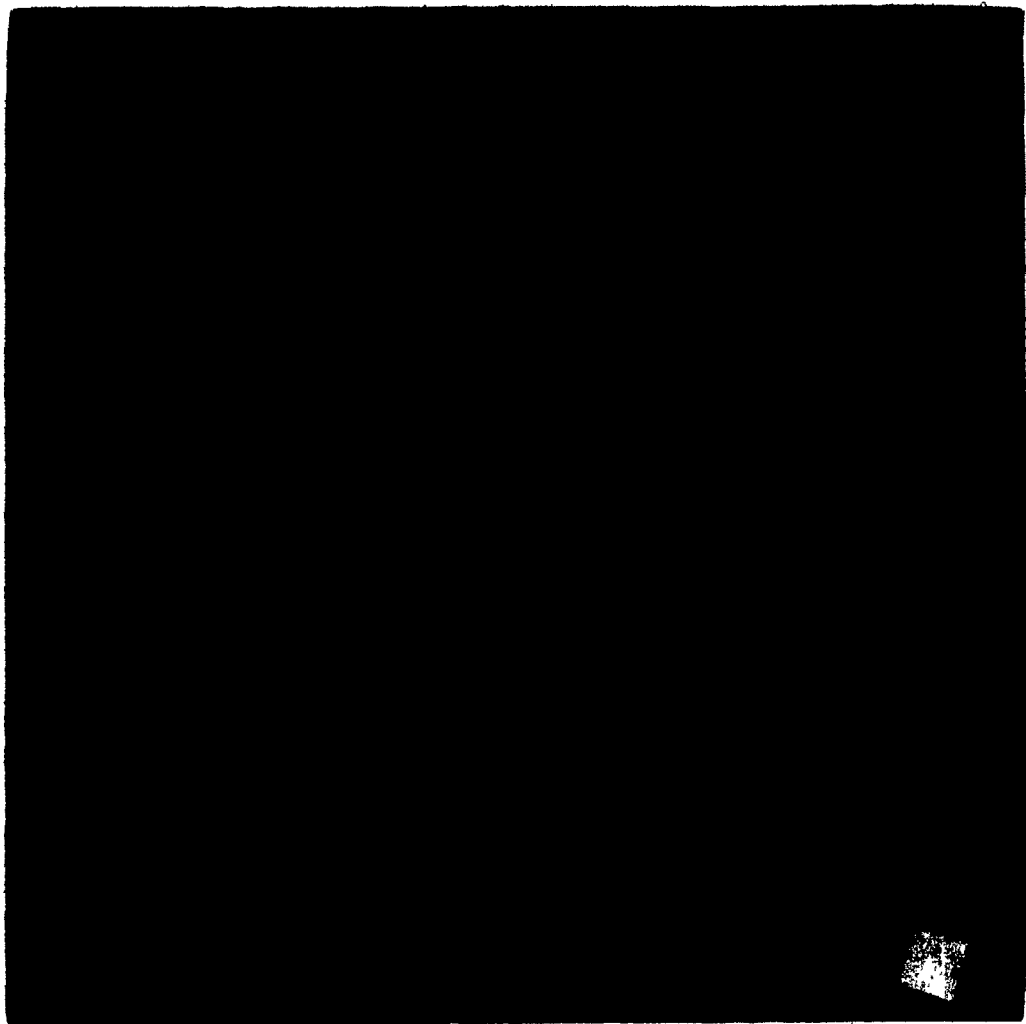


PLATE IX. Phase angle PPI at 1° elevation for 0210 MDT-27 July 1972. The darkest shade of the grey shade scale corresponds to orientations of the minor axis of the backscattered ellipse between 0 and 18°. The other shades correspond to orientations between 18 and 36°, 36 and 54°, 54 and 72°, with the brightest 72 and 90°. The orientations of the minor axis of the backscattered ellipse are measured counterclockwise from the vertical as viewed from the radar. The range rings are at 10 mile (=16.1 km) intervals.

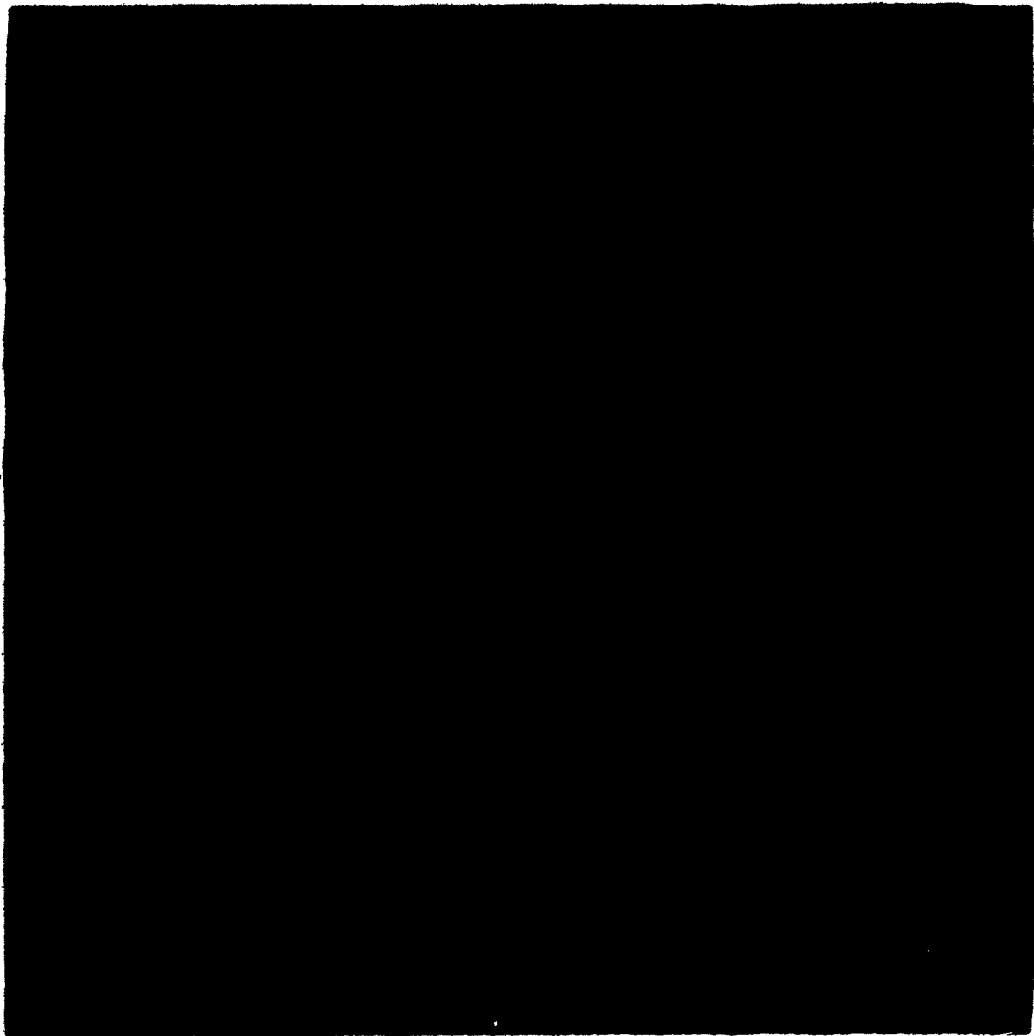


PLATE X.

Phase angle PPI at 1° elevation for 0213 MDT-27 July 1972. The grey shade scale has been adjusted so that the darkest shade corresponds to orientations of the minor axis of the backscattered ellipse between -54 and -36° . The other shades correspond to orientations between -36 and -18° , -18 and 0° , 0 and 18° , with the brightest 18 and 36° . The orientations of the minor axis of the backscattered ellipse are measured counterclockwise from the vertical as viewed from the radar. The range rings are at 10 mile (≈ 16.1 km) intervals.

CHAPTER VI

BACKSCATTER EFFECTS

6.1 The Orientation of Raindrops

In Chapter 5 it was noted that for the low rainfall rates observed in widespread precipitation the propagation effect is small and since, at 3 GHz, raindrops behave as Rayleigh scatterers, the differential phase shift upon scattering is negligible. As a result the orientation of the backscattered ellipse is the same as the orientation of the scatterers. The observations of the phase angle shown in Fig. 5.1 illustrate that for the two days in June the orientation of the backscattered ellipse was predominantly about 0° which is consistent with the idea that raindrops fall as oblate spheroids with a vertical symmetry axis. During the summers of 1971 and 1972 phase angle data were collected for several days with stratiform rain like 12 June and 23 June 1972. For these occasions the frequency distributions of the orientation of the backscattered ellipse were asymmetric with the peak occurring near 0° and the tail between 0 and 45° . The tail between 0 and 45° indicates the influence of a propagation effect but not so strong as to shift the peak away from 0° .

If the conclusion is correct that raindrops tend to fall with a vertical symmetry axis then even for convective situations it would be expected that the orientation of the backscattered ellipse would be close to 0° at the front edge of

18 MAY 1972 ELEVATION 3.1
0542 - 0553 MDT AZIMUTH 80°

25 MAY 1972 ELEVATION 2.8
0028 - 0034 MDT AZIMUTH 186°

25 MAY 1972 ELEVATION 5.1
0035 - 0039 MDT AZIMUTH 186°

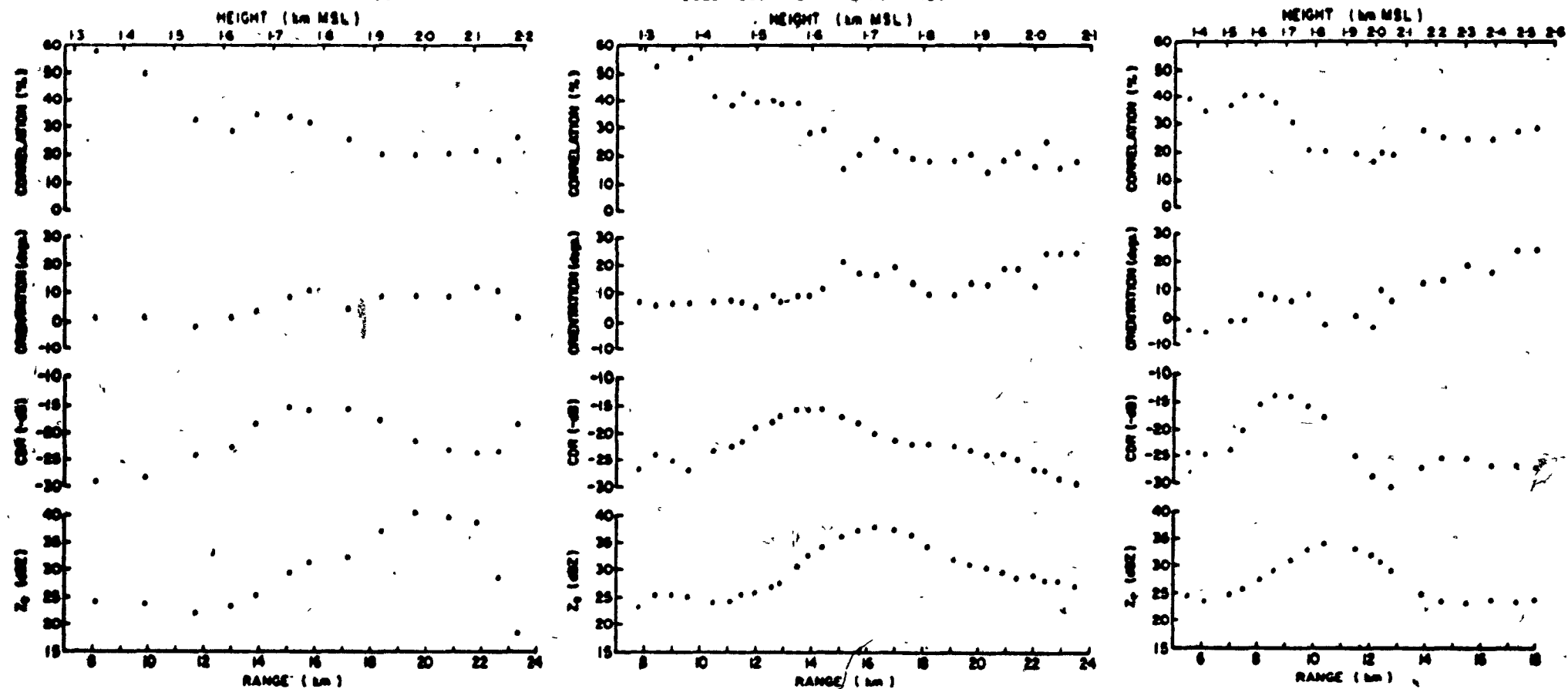


Fig. 6.1 Samples of observations of the melting layer obtained with the chart recorder system. The antenna was at a fixed azimuth as the range gate was moved out in range. The observations are along a slant path and the top scale gives the height of each observation along the path.

the precipitation where the propagation term is small. Plates IV, V, IX and X of the phase angle PPI display show that along the front edge of the convective storm of 27 July 1972 the orientation of the backscattered ellipse was indeed between 0 and 18°.

(6.) Bright Band Observations

On several occasions during May and June 1972 chart recorder and PPI observations were made on days when there was widespread precipitation with a bright band present. The chart recorder data were obtained with the antenna fixed in position so that the range gate could be moved back and forth to obtain a range profile of the precipitation. If the precipitation is horizontally uniform then this slant range profile can also be interpreted as a height profile. Some examples of observations of the melting level obtained with the chart recorder system are shown in Fig. 6.1. It should be noted that there were several cases when neither the reflectivity nor the CDR had peaks below the melting level. However, when the CDR and reflectivity did show a peak, such as those illustrated in Fig. 6.1, the peak in the CDR was often below the peak in the reflectivity. This phenomenon has also been reported by Newell et al. (1955). Lhermitte and Atlas (1963) concluded that the falloff in reflectivity below the melting layer is partly the result of drop breakup. This line of reasoning suggests that when the drops are breaking up, thus decreasing the reflectivity,

they may be oscillating and quite deformed, thus yielding a high CDR. Therefore, as drop breakup decreases the reflectivity. It increases the CDR so that the peak in the CDR occurs below the peak in the reflectivity.

Measurements of the phase angle in general show orientations of the backscattered ellipse starting out near 0° and slowly increasing up through the melting level indicating the presence of a weak propagation effect.

The correlation measurements usually show a drop off to about 20 percent as the range gate is moved out through the melting level. This suggests that the scatterers may be oscillating or tumbling in this region.

The PPI displays for the main power, CDR, correlation, and phase angle are shown in Plates XI, XII, XIII, XIV for the widespread rain situation of 23 June 1972. Although the melting level does not stand out on the main power display it is readily discernible on the other displays.

Plate XII reveals that in the melting level, at about 40 miles range, the values of the CDR although not uniform are generally higher than in the rain below. The CDR is not displayed in the light precipitation regions because the orthogonal signal is too close to the receiver noise.

The correlation PPI display (Plate XIII) is somewhat speckled in the melting layer but by going out in range through the bright band a decrease in correlation can be observed. In Plate XI two cells of heavier precipitation can be seen at 20

miles from the radar, one to the south-southwest and the other to the southeast. These cells stand out on the correlation PPI (Plate XIII) and show higher correlations than in the bright band. The correlation is not displayed in the light precipitation areas since the CDRs are small and the orthogonal signal is too close to the receiver noise.

The phase angle PPI display is quite speckled in the melting layer which is partly a result of the phase angle not being displayed when the correlation is low since the phase information then becomes random. However, the orientation of the backscattered ellipse can be observed to progress with range from 0 to 45°. This progression with range is most evident in the heavier precipitation regions at 20 miles to the south-southwest of the radar.

In Plate XI there is a long region of high reflectivities between 25 and 55 miles to the north-northeast of the radar. Plate XIII shows the correlation to be high in this region and Plate XIV shows the orientation of the backscattered ellipse to progress rapidly with range from 0 to 45°. Furthermore, Plate XII shows the CDR increasing with range and thus indicating a propagation effect. It is difficult to calculate the propagation term in this situation since the propagation path is through the melting level where the size, shape, dielectric constant, and number density of the scatterers are unknown.

6.3 Non-Rayleigh Scattering

With the orientation of the scatterers, α , and the orientation of the anisotropy, τ , set to 0° the expression obtained in Section 4.5 to determine the phase angle becomes

$$\frac{W_2 + jW_3}{W_1} = \rho_a \bar{v}_e j\delta + j\rho_e jX \quad (6.1)$$

In this case the phase angle, $\theta = \arctan(W_3/W_2)$, is directly related to the differential phase shift upon scattering (δ) when the propagation term is small. Applying Rayleigh theory to scattering from small ellipsoids yields $\delta = 0^\circ$. However, for 3 GHz radiation hailstones can not be considered as small and δ may no longer be zero. Therefore, the phase angle may be different for rain and hail because of possible differential phase shifts upon scattering by hail. With this in mind the chart recorder data and photographs of the phase PPI display were examined to see if unusual phase angle measurements were obtained from hailstorms. For observations below the melting level the orientation of the backscattered ellipse was always between 0 and 45° . Unfortunately the propagation term can also cause the backscattered ellipse to have these orientations. Furthermore, the regions in the storm with high reflectivities and CDRs where hail would be expected happen to be the regions that contribute the most to the propagation term.

Using the unpublished scattering amplitudes for hailstones calculated by Oguchi the differential scattering phase shift was calculated for each hailstone. The results are

given in Table 6.1 where the orientation of the backscattered ellipse for each hailstone is tabulated with dimensions, assuming their shapes to be oblate spheroids. The table shows that scattering from a region containing only identical hailstones would yield an orientation of the backscattered ellipse that lies within the range of values that can be attributed to propagation effects. The presence of rain would shift the orientations towards 0° .

TABLE 6.1. The minimum and maximum diameters of four oblate hailstones and the orientation of the backscattered ellipse for a region containing only that type of hailstone.

	MINIMUM DIAMETER (cm)	MAXIMUM DIAMETER (cm)	ORIENTATION OF BACKSCATTERED ELLIPSE (deg)
(1)	3.05	3.71	22
(2)	2.54	4.11	21
(3)	2.16	3.30	12
(4)	1.27	1.91	2

The only regions where unusual phase angles have been observed were above the melting level. Plate XV shows the 4° elevation phase angle PPI for 27 July 1972. This photograph was taken about four minutes after Plate V. The grey shade is calibrated so that the darkest shade corresponds to orientations between 72° and 90° , changing in 18° steps (-90 to -72° , -72 to -54° , -54 to -36°) to the brightest shade for -36 to -18° . At

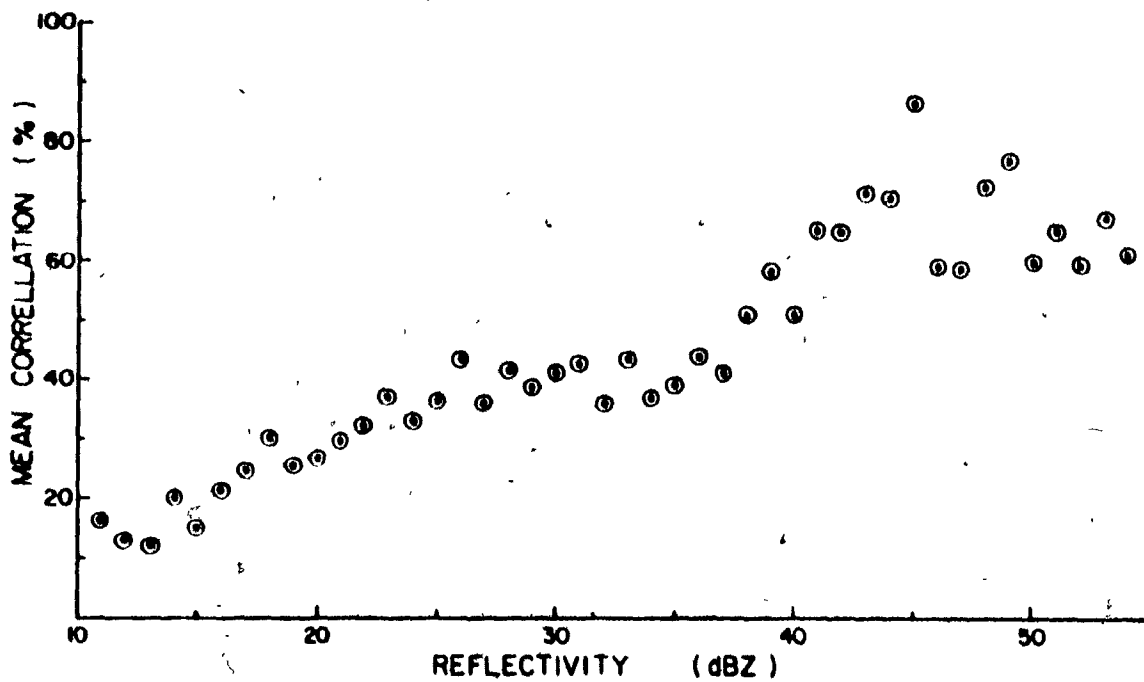


Fig. 6.2 Mean correlation as a function of reflectivity. The points represent the average values of the correlation in reflectivity intervals of 1 dBZ. The data were taken with the chart recorder system during the summer of 1972. All observations were below the melting level and above 1° elevation.

4° elevation the orientation falls between -36° and -18° with a few small areas with orientations between -54° and -36° but below this elevation the phase angle PPIs gave orientations between 0 and 45° in this region. It is not obvious what has caused such an orientation of the backscattered ellipse but the situation is not unique since a few similar observations have been made at the top of other thunderstorms.

6.4 Correlation Observations

McCormick and Hendry (1972) presented the correlation averaged over many observations as a function of the reflectivity as measured by a 16.5 GHz polarization diversity radar. Their graph shows that the correlation at reflectivities greater than 20 dBz is between 70 and 85%. Measurements of the correlation with the 3 GHz Alberta Hall Studies radar tend to be lower than this except for intense thunderstorms. Fig. 6.2 shows the correlation averaged over the observations for the summer of 1972 as a function of the reflectivity. The measurements were obtained with the chart recorder system which was gated over many regions of the various storms and widespread precipitation areas that were observed. All the measurements that were used for this graph were made below the melting level and above 1° elevation. The graph shows that for reflectivities less than 40 dBz the mean correlation is less than 60%. The correlation increases with the reflectivity suggesting that the higher rainfall rates contain a larger fraction of drops with similar

orientations. The number of observations for reflectivities greater than 44 dBz are relatively few so that fluctuations are to be expected. Since the correlations measured at 3 GHz are generally lower than those measured at 16.5 GHz the question is whether or not this is a frequency dependent phenomenon. The propagation effect, which tends to increase the correlation, is stronger at 16.5 GHz than at 3 GHz so that this may explain the difference between the two correlation-reflectivity relationships.

The correlation PPI display shows that storms in Alberta can have a high correlation. Plates III and VIII illustrate that the correlation is between 63 and 80% over a large region of the intense storm of 27 July 1972. However, the propagation term is probably influencing the correlation on the far side of the storm.

6.5 Backscatter Calculations

Based on the theoretical developments given in Chapter III calculations were made to determine some of the backscatter polarization parameters for rain. To do this the drop size distribution of Marshall and Palmer (1948) was divided into 80 intervals of diameter from 0.1 to 8.0 mm. An axial ratio was assigned to each drop size interval based on the size-shape relationship for raindrops of Pruppacher and Pitter (1971). The scattering matrix elements were then calculated for each of the eighty drop classes and from these the CDR was calculated as

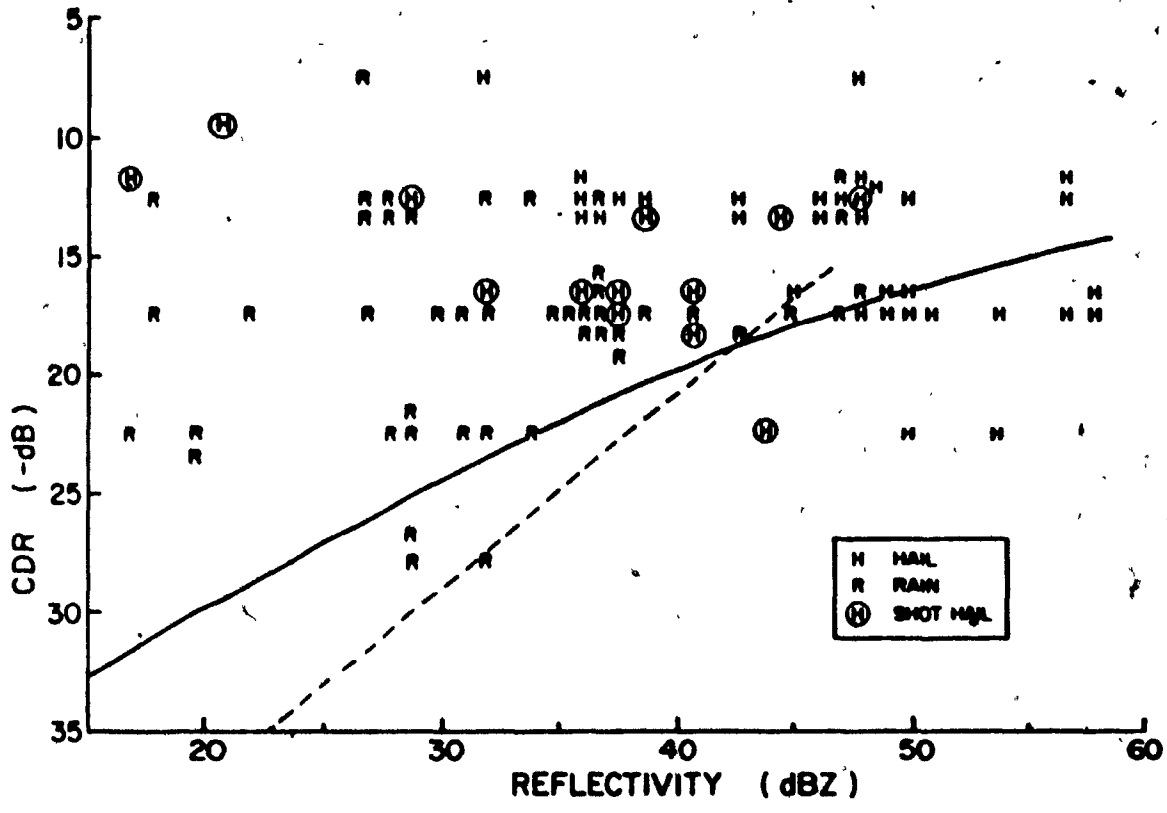


Fig. 6.3 Scatter diagram of surface rain and hail reports with corresponding values of the CDR and reflectivity measured aloft by the radar and including theoretical calculations of the CDR and reflectivity for rain. The solid line corresponds to the results of this present work and the dashed line corresponds to the results of Barge (1972). The scatter diagram is reproduced from Barge (1972).

a function of rainfall rate. Using the scattering matrix elements the reflectivity was also calculated for each rainfall rate so that the CDR could be directly related to the reflectivity. The result is the solid curve in Fig. 6.3 which includes the results of Barge (1972) who compared the reflectivity and CDR measurements in storms to the observations of rain or hail falling at the ground. Barge (1972) also calculated the CDR and reflectivity for rain samples collected by various authors and fitted a straight line to the results which is the dashed line in Fig. 6.3.

The present calculations show that using just the Marshall-Palmer distribution causes the CDR versus reflectivity line to decrease in slope as the reflectivity increases thus limiting the value of the CDR. The curve of the line is due in part to the shape of the Pruppacher-Pitter curve (see Fig. 5.6) which begins to level out as the drop size increases. It seems reasonable that the CDR for rain should approach a limiting value as the rainfall rate increases since there is a limit to the drop size and thus the drop shape as a result of drop breakup. The maximum diameter used in the present calculations was 8.0 mm since this is approximately the largest size raindrop that can exist without breaking up (Fournier and Hidayetulla, 1955). Therefore, since the axial ratio of oblate raindrops decreases as their size increases, an upper limit in the CDR would be attained if the majority of the drops were 8.0 mm in diameter. The CDR in this case would be -10.6 dB. Observations of CDRs

larger than this have either been influenced by the propagation term or indicate the presence of scatterers which are not raindrops.

During the computations of the CDR and reflectivity for various rainfall rates of the Marshall-Palmer distribution it was noted that the results were sensitive to the magnitude of the size interval used. If the number of intervals in the drop size distribution is decreased, that is if the width of the size interval is increased, then for a given rainfall rate the CDR decreases and the reflectivity increases. As a result the gap is reduced between the present CDR-reflectivity curve and the line of Barge (1972). The sensitivity of the calculations to the drop size interval diminishes as the rainfall rate increases.

Many of the rain points in Fig. 6.3 have CDRs that lie above the theoretical CDR-reflectivity curve for rain. Barge (1972) attributed these observations to small hail that was observed aloft by the radar but which melted by the time it reached the ground. This is still a possibility but on the basis of the results reported in Chapter V it is suggested that some of these points may have been influenced by the propagation effect. As a result the observed CDRs were not the intrinsic values but a combination of the intrinsic CDR and the altered polarization of the beam due to propagation through rain.

To determine which drops contribute most to the reflectivity and which contribute most to the CDR the percentage contribution of each drop size interval was calculated. The

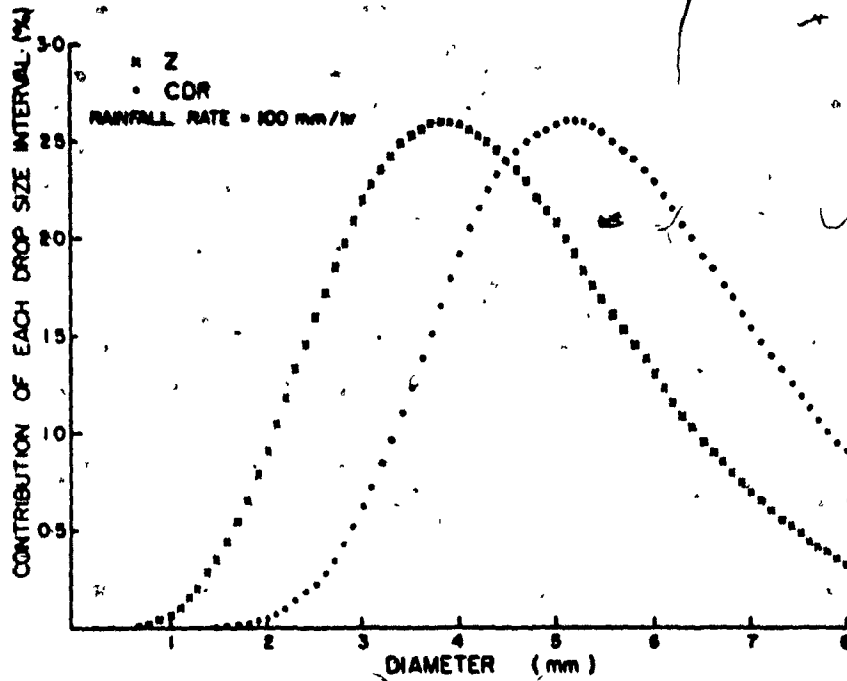


Fig. 6.4 The contribution of each size interval of the drop size distribution to the CDR and Z for a rainfall rate of 100 mm/hr. There were 80 size intervals for drop diameters between 0 and 8 mm.

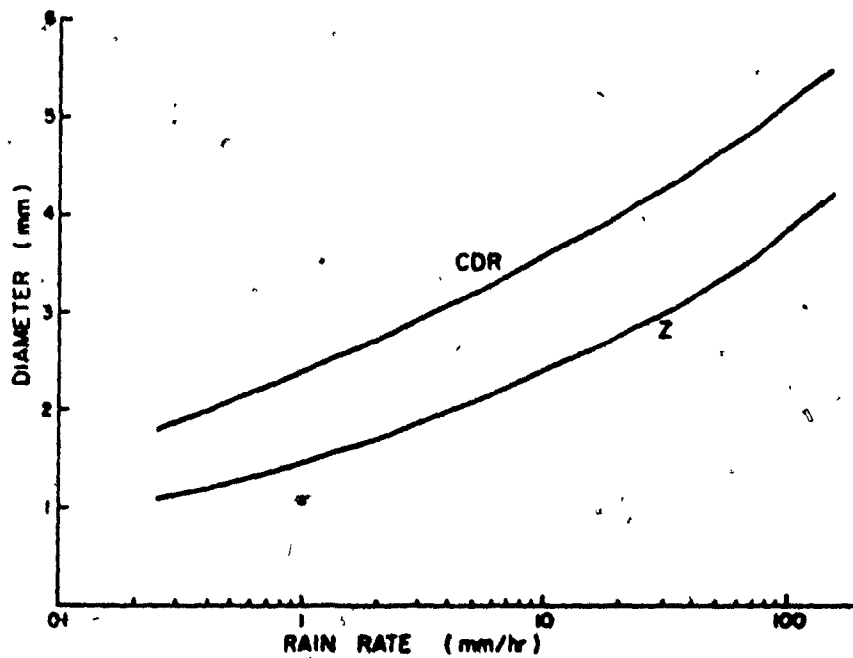


Fig. 6.5 The diameter of the drops in the size interval contributing the most to the CDR and Z as a function of rain rate.

results are shown in Fig. 6.4 for a rainfall rate of 100 mm/hr. It is evident that the drops contributing most to the CDR are larger and therefore more deformed than the drops contributing most to the reflectivity. The size intervals with the largest contributions to the CDR and reflectivity are plotted versus the rainfall rate in Fig. 6.5. The graph shows a slight increase in separation between the two lines as the rainfall rate increases.

An estimate of the types of drop size distributions that occur in Alberta rain could be obtained by fitting various drop size distributions to observations of the CDR and reflectivity in rain which were not influenced by propagation effects. Since the CDR and reflectivity are sensitive to different size intervals of the drop size distribution, the fitting procedure is not as ambiguous as it would be if the same size intervals were involved for both quantities. If this type of fitting procedure is employed it should be kept in mind that the calculations are sensitive to the magnitude of the drop size interval used.



PLATE XI.

Main power PPI at 1° elevation for 1748 MDT-23 June 1972. The grey shade scale is in 10 dB steps with the darkest shade corresponding to values between -90 and -80 dBm and the brightest to values between -50 and -40 dBm. The range rings are at 10 mile (≈ 16.1 km) intervals.



PLATE XII. PPI display of the CDR at 1° elevation for 1748 MDT-23 June 1972. The grey shade scale is in 5 dB steps with the darkest shade corresponding to values of the CDR less than -25 dB and the brightest to values between -10 and -5 dB. The range rings are at 10 mile (=16.1 km) intervals.



PLATE XIII. PPI display of the correlation at 1° elevation for 1748 MDT-23 June 1972. The darkest shade of the grey shade scale corresponds to correlations between 17 and 33%. The other shades correspond to correlations between 33 and 50%, 50 and 67%, 67 and 83%, with the brightest 83 and 100%. The inside edge of the grey shade scale is at 70 miles (=113 km). Ground clutter extends out to approximately 10 miles (=16.1 km).

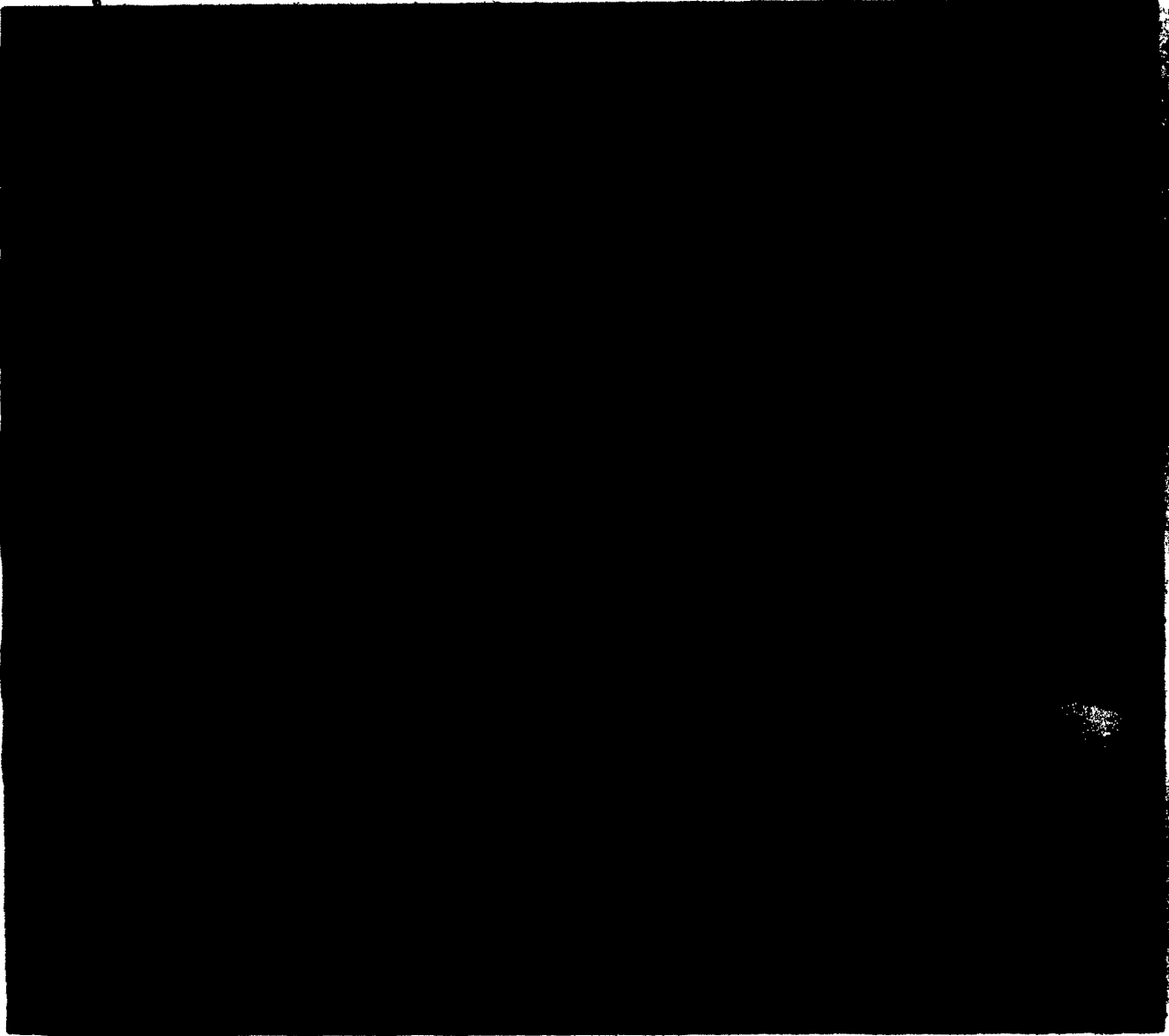


PLATE XIV.

Phase angle PPI at 1° elevation for 1751, MDT-
23 June 1972. The darkest shade of the grey shade
scale corresponds to orientations of the minor axis
of the backscattered ellipse between -36 and -18° .
The other shades correspond to orientations between
 -18 and 0° , 0 and 18° , 18 and 36° , with the
brightest 36 and 54° . The orientations of the
minor axis of the backscattered ellipse are
measured counterclockwise from the vertical as
viewed from the radar. The inside edge of the grey
shade scale is at 70 miles (≈ 113 km). Ground
clutter extends out to approximately 10 miles
(≈ 16.1 km).

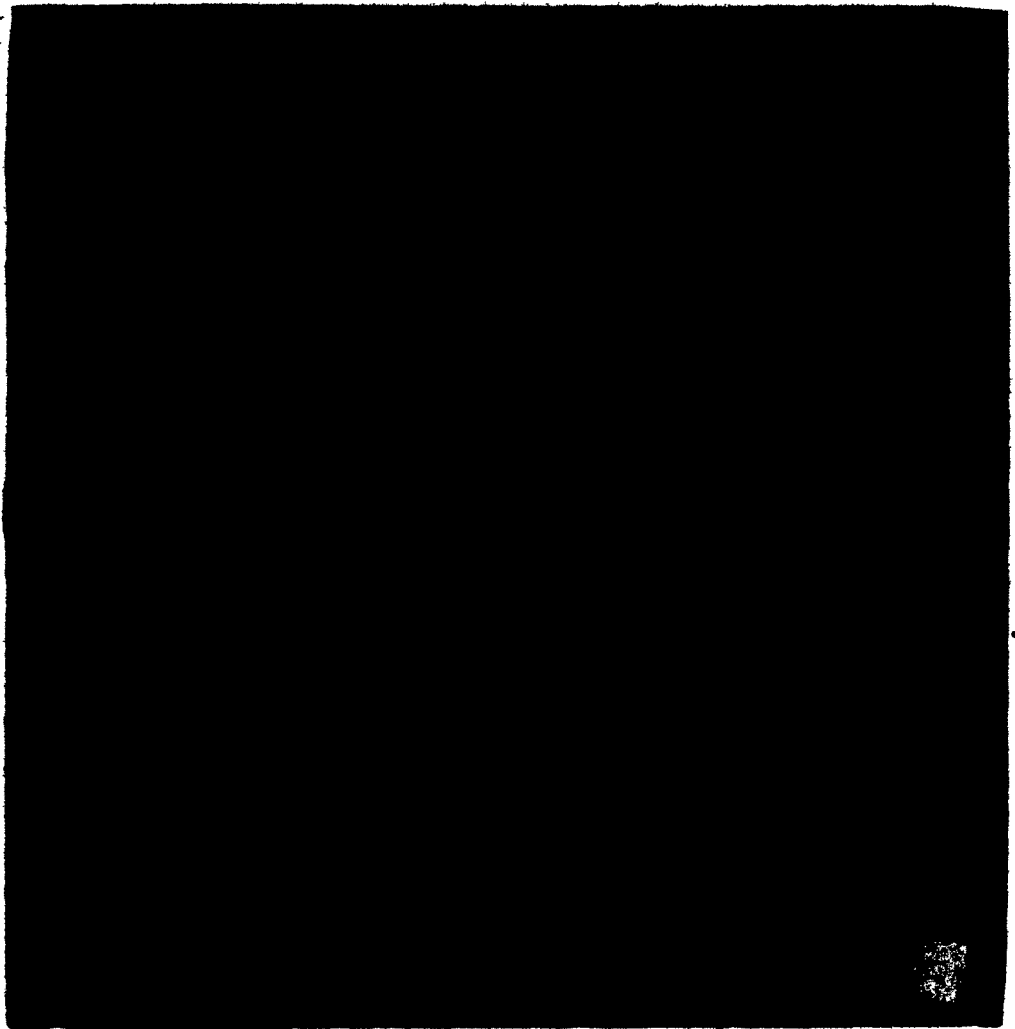


PLATE XV.

Phase angle PPI at 4° elevation for 0156 MDT-27 July 1972. The darkest shade of the grey shade scale corresponds to orientations of the minor axis of the backscattered ellipse between 72 and 90° . The other shades correspond to orientations between -90 and -72° , -72 and -54° , -54 and -36° , with the brightest -36 and -18° . The orientations of the minor axis of the backscattered ellipse are measured counterclockwise from the vertical as viewed from the radar. The inside edge of the grey shade scale is at 70 miles (≈ 113 km).

CHAPTER VII

SUMMARY AND CONCLUSIONS

7.1 Summary

The review in Chapter II pointed out that although the CDR and reflectivity have been studied with respect to precipitation observations, the phase difference and correlation between the main and orthogonal components have received little attention. Polarization studies involving parameters other than the CDR and reflectivity have been restricted to the field of communications at frequencies higher than 3 GHz. Polarization studies with the Alberta Hail Studies radar have been primarily concerned with discriminating between rain and hail on the basis of measurements of the CDR and reflectivity. It was therefore thought that a study of the phase angle and correlation measurements would prove helpful in the attempt to discriminate between hail and rain.

Chapters I and III related the various polarization properties of the backscattered radiation to the observables measured by the radar. These observables were related to the number density and the forward and backward scattering properties of the precipitation particles. The scattering properties were seen to be a function of the particle size, shape, and dielectric constant.

Chapter IV briefly described the radar facilities at the Alberta Hail Studies. For the summer of 1972 a new piece of

equipment developed by the National Research Council enabled the phase angle and correlation to be presented on a PPI display.

In Chapter V it was pointed out that certain observations of the phase angle could not be attributed to the orientation of the scatterers and therefore propagation effects or non-Rayleigh scattering effects must have been present. Calculations indicated that rain can introduce a differential phase shift between the vertical and horizontal components of a wave that was initially circularly polarized. This differential phase shift alters the polarization of the transmitted radiation so that measurements of the CDR are no longer directly related to the backscatter properties of the precipitation particles. The storm of 27 July 1972 demonstrated that the propagation effect is important at 3 GHz and that measurements of the CDR behind regions of high reflectivity can be dominated by the propagation term. The clue that a propagation effect was present came from the phase angle PPI display which shows the orientation of the backscattered ellipse quickly progressing with range from 0 to 45°. Furthermore, the correlations in this storm were high indicating that a large fraction of the scatterers had similar orientations thus forming an anisotropic medium. Theoretical calculations for hailstones suggest that propagation through hail could depolarize the transmitted radiation more than rain.

In Chapter VI it was demonstrated that when the propagation term is small the observed values of the phase angle in rain are consistent with the idea that raindrops fall as

oblate spheroids with their minor axis vertical. The phase angle measurements at 16.5 GHz of McCormick and Hendry (1970) are also consistent with this conclusion. Observations through the melting layer of widespread precipitation have shown that when a peak occurs in both the reflectivity and CDR the peak in the CDR often appears below the peak in the reflectivity. It was suggested that this may be partly the result of drop breakup inducing oscillations and distortions. The correlation was observed to decrease up through the melting layer, signifying that the scatterers have no preferred orientation. An attempt was made to see if the phase angle could uniquely distinguish between rain and hail. The observations and theoretical calculations show that it is very difficult to separate the non-Rayleigh scattering effects from the propagation effects. The only unusual phase angle observations were obtained from the upper regions of thunderstorms. It was shown that although the correlation is generally high below the melting level in convective storms and convective cells imbedded in widespread precipitation, the average correlation measured at 3 GHz in Alberta for a given reflectivity appears to be lower than that measured at 16.5 GHz in Ottawa. Finally it was argued, through calculations of the CDR as a function of reflectivity, that the CDR tends toward a limiting value (≈ -11 dB) as the rainfall rate increases. Observations of the CDR higher than this limiting value are probably the result of scatterers other than raindrops or else the CDR is dominated by propagation effects. Further

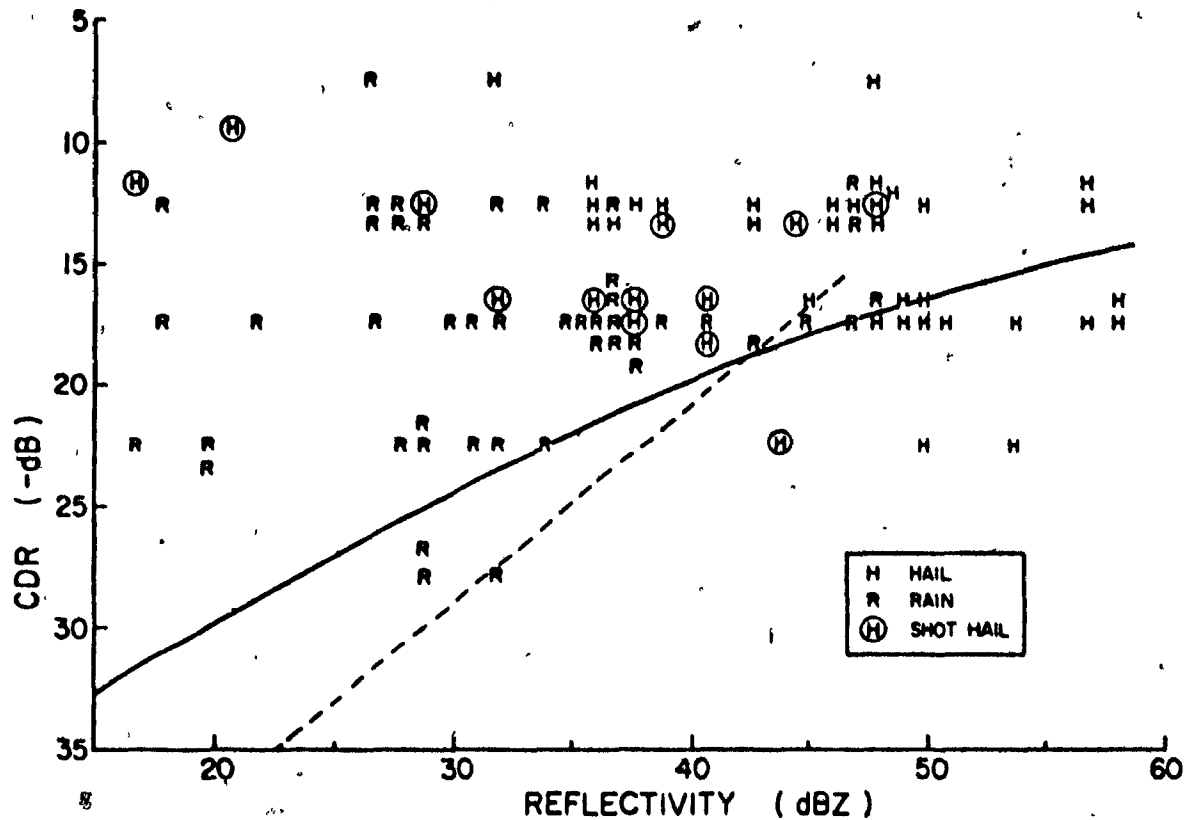


Fig. 6.3 Scatter diagram of surface rain and hail reports with corresponding values of the CDR and reflectivity measured aloft by the radar and including theoretical calculations of the CDR and reflectivity for rain. The solid line corresponds to the results of this present work and the dashed line corresponds to the results of Barge (1972). The scatter diagram is reproduced from Barge (1972).

calculations demonstrated that the CDR and reflectivity are sensitive to different size intervals of the drop size distribution. Also it was found that the calculations are sensitive to the width that was used for the drop size intervals.

7.2 Conclusions

Observations and theoretical calculations show that propagation through rain can depolarize a circularly polarized wave so that CDR measurements are dominated by this propagation effect and not by the backscatter properties of the precipitation particles. Before considering the consequences of this result the observations of a previous polarization study using the Alberta Hail Studies radar will be reviewed.

In the research of Barge (1972) observations of the CDR and reflectivity were compared with ground observations of the occurrence of rain or hail. The results were presented in a scatter diagram which is shown in Fig. 6.3. It can be seen that when the reflectivity was greater than 48 dBZ hail was always observed on the ground. For reflectivities between 34 and 48 dBZ, the likelihood of hail being observed on the ground increases with the CDR. In this study Barge also calculated the CDRs and reflectivities for various raindrop size spectra that have been reported in the literature. Compared to the drop size distribution of Marshall and Palmer (1948) it was found that the CDRs of the other size spectra were either much lower or 3 to 4 dB higher for a given reflectivity. The only exceptions were a

few of the size spectra of Cataneo and Stout (1968) where the CDR was calculated to be as high as -16 dB for reflectivities between 30 and 37 dBZ.

The scatter diagram (Fig. 6.3) shows many rain observations lying well above the theoretical curve (solid line). The explanation previously given for these observations was that the radar was observing small hail aloft which melted by the time it reached the ground. While this may be true the results of Chapter V suggest that some of these observations may have been influenced by the propagation effect. It would therefore be useful to reanalyze the data in Fig. 6.3 and eliminate any observations where the propagation effect might be important such as on the far side of a thunderstorm. It is expected that some of the rain observations, with CDRs much above the theoretical curve, would then be eliminated. This would certainly improve the scatter diagram and strengthen the conclusion that the CDR is useful in discriminating between rain and hail.

It was previously mentioned that whenever the reflectivity is between 34 and 48 dBZ the probability of hail occurring on the ground increases with the CDR. Since propagation through heavy rain can seriously depolarize a 3 GHz circularly polarized wave the interpretation of the CDR-reflectivity observations in this region must be made with some estimate of the strength of this propagation effect. There are several ways that this estimate can be obtained.

In Fig. 5.6 it can be seen that the differential phase

shift (in degrees/km) is an exponential function of the reflectivity and therefore it should be possible to integrate the reflectivity with range to determine the total differential phase shift. This could be done with a device similar to ADA (Zawadzki and Rogers, 1969).

The phase angle and correlation PPI displays are useful in determining whether or not a propagation effect is present. High correlations in the intense precipitation areas indicate that a large fraction of the scatterers have the same orientation and thus form an anisotropic propagation medium. If the orientation of the backscattered ellipse is observed to progress rapidly with range from 0 to 45° or to remain greater than 36° when the reflectivity is relatively high then the propagation term is important.

Because propagation through rain causes the orientation of the backscattered ellipse to depart from the neighbourhood of 0° the phase angle does not readily discriminate between hail and rain on the basis of the non-Rayleigh differential phase shift upon scattering. However, theoretical calculations indicate that propagation through hail can cause greater depolarizations than rain and since the effect of propagation through rain can be estimated it could be useful to study the range variation of the various polarization parameters. If changes along a propagation path occur more rapidly or are larger than can be attributed to rain then this may indicate the presence of hail. This study would require reflectivity contours to be finer than the 10 dB

steps now available and the orientation of the backscattered ellipse to be contoured in steps smaller than 18° (i.e. the phase angle steps smaller than 36°). The chart recorder system could be used for a study of this type by moving the range gate back and forth through the storm with the antenna at a fixed azimuth. However, this procedure was not possible in the past since the antenna was set in the scan mode during thunderstorms so that the radar could be used to direct cloud seeding operations. An investigation of the range variation of the polarization parameters would be more feasible if the Alberta Hail Studies radar was computerized.

At present it appears that the best way to discriminate between rain and hail with a polarization diversity radar is with CDR-reflectivity measurements provided consideration is given to the propagation effect.

APPENDIX I

THE SCATTERING AMPLITUDES OF FOUR HAILSTONES

In 1972 the Alberta Hail Studies sent a sample of hailstones to Dr. G.C. McCormick's group at the National Research Council to be used in S-band scattering measurements. From this sample four hailstones, shaped like oblate spheroids, were selected and their minimum and maximum dimensions were sent to Dr. T. Oguchi of the Radio Research Laboratories in Japan. Assuming the four hailstones to be oblate spheroids of ice at 0°C he calculated their forward and backward scattering amplitudes. These scattering amplitudes were passed on to the author via Dr. McCormick and were used to calculate the parameters in Tables 5.1 and 6.1.

Table A1.1 lists the shape parameters of the four hailstones, Table A1.2 lists the forward scattering amplitudes, and Table A1.3 lists the backward scattering amplitudes.

TABLE A1.1. The minimum and maximum diameters, the axial ratio, and the diameter of an equivolumic sphere for the four selected hailstones.

	MINIMUM DIAMETER (cm)	MAXIMUM DIAMETER (cm)	AXIAL RATIO	EQUIVALENT DIAMETER (cm)
(1)	3.05	3.71	0.822	3.48
(2)	2.54	4.11	0.618	3.50
(3)	2.16	3.30	0.655	2.87
(4)	1.27	1.91	0.665	1.67

TABLE A1.2. The forward scattering amplitudes of the four selected hailstones. The underlined numbers may be inaccurate.

	$S_{11}(0)$	$S_{22}(0)$
(1)	$9.62 \times 10^{-3} - 2.26 \times 10^{-3}j$	$1.08 \times 10^{-2} - 3.00 \times 10^{-3}j$
(2)	$8.9 \times 10^{-3} - 1.74 \times 10^{-3}j$	$1.17 \times 10^{-2} - 3.4 \times 10^{-3}j$
(3)	$4.7 \times 10^{-3} - 6.03 \times 10^{-4}j$	$6.1 \times 10^{-3} - 1.06 \times 10^{-3}j$
(4)	$8.4 \times 10^{-4} - 2.61 \times 10^{-5}j$	$1.05 \times 10^{-3} - 4.1 \times 10^{-5}j$

TABLE A1.3. The backward scattering amplitudes of the four selected hailstones. The underlined numbers may be inaccurate.

	$S_{11}(180)$	$S_{22}(180)$
(1)	$4.28 \times 10^{-3} - 1.94 \times 10^{-3}j$	$4.84 \times 10^{-3} - 2.58 \times 10^{-3}j$
(2)	$3.2 \times 10^{-3} - 1.4 \times 10^{-3}j$	$4.3 \times 10^{-3} - 2.7 \times 10^{-3}j$
(3)	$2.7 \times 10^{-3} - 5.5 \times 10^{-4}j$	$3.6 \times 10^{-3} - 9.8 \times 10^{-4}j$
(4)	$7.0 \times 10^{-4} - 2.55 \times 10^{-5}j$	$8.9 \times 10^{-4} - 4.0 \times 10^{-5}j$

REFERENCES

- Allan, L.E., R.C. Markell, and G.C. McCormick, 1967: A variable-polarization antenna. Rep. ERB-768, Radio and Electrical Engineering Division, National Research Council of Canada, 12 pp.
- Atlas, D., M. Kerker, and W. Hitschfeld, 1953: Scattering and attenuation by non-spherical atmospheric particles. *J. Atmos. and Terrest. Phys.*, 3, 108-119.
- Barge, B.L., 1972: Hail detection with a polarization diversity radar. Sci. Rep. MW-71, Stormy Weather Group, McGill University, Montreal, 80 pp.
- Browne, I.C., and N.P. Robinson, 1952: Cross-polarization of the radar melting band. *Nature*, 170, 1078-1079.
- Cataneo, R., and G.E. Stout, 1968: Raindrop-size distribution in humid continental climates, and associated rainfall rate-radar reflectivity relationships. *J. Appl. Meteor.*, 7, 901-907.
- Crispin, J.W., Jr., and K.M. Siegel, eds., 1968: Methods of Radar Cross-Section Analysis, New York and London, Academic Press Inc., 426 pp.
- English, M., 1972: The Growth of Large Hail. Ph.D. Thesis, Dept. of Meteor., McGill University, Montreal.
- Fournier, d'Albe, E.M., and M.S. Hidayetulla, 1955: The break-up of large water drops falling at terminal velocity in free air. *Quart. J. Roy. Meteor. Soc.*, 81, 610-613.
- Gans, R., 1912: Über die Form ultramikroskopischer Goldteilchen (On the form of ultra-microscopic gold particles). *Ann. Phys.*, 37, 881-900.
- Gershenson, Yu, M., and A.B. Shuplatskii, 1961: Scattering of elliptically polarized radio waves by non-spherical atmospheric particles. *Tsentral'naia Aerologicheskaya Observatoriia*, Trudy, No. 36, 102-118.
- Hendry, A., and L.E. Allan, 1973: Apparatus for the real-time display of correlation and relative phase angle data from the Alberta Hail Studies radar. Rep. ERB-875, Radio and Electrical Engineering Division, National Research Council of Canada, 16 pp.

- Hunter, I.M., 1954: Polarization of radar echoes from meteorological precipitation. *Nature*, 173, 165-166.
- Kerker, M., and W. Illitschfeld, 1950: Effects of particle shape and secondary scattering on microwave reflections from clouds and precipitation. *Sci. Rep. MW-1*, Stormy Weather Group, McGill University, Montreal, 32 pp.
- Labrum, N.R., 1952: The scattering of radio waves by meteorological particles. *J. Appl. Phys.*, 23, 1324-1330.
- Lhermitte, R.M., and Atlas, 1963: Doppler fall speed and particle growth in stratiform precipitation. *Proc. Tenth Wea. Radar Conf.*, Washington, Amer. Meteor. Soc., 218-223.
- Marshall, J.S., and W. McK. Palmer, 1948: The distribution of raindrops with size. *J. Meteor.*, 5, 165-166.
- _____, and W.E. Gordon, 1957: Radiometeorology. *Meteor. Monographs*, 3, 73-113.
- McCormick, G.C., 1968: An antenna for obtaining polarization-related data with the Alberta Hail Radar. *Proc. of the Thirteenth Radar Meteor. Conf.*, Montreal, Amer. Meteor. Soc. 340-347.
- _____, and A. Hendry, 1970: The study of precipitation backscatter at 1.8 cm with a polarization diversity radar. *Proc. of the Fourteenth Radar Meteor. Conf.*, Tucson, Amer. Meteor. Soc., 225-230.
- _____, and _____, 1972: Results of precipitation backscatter measurements at 1.8 cm with a polarization diversity radar. *Proc. of the Fifteenth Radar Meteor. Conf.*, Champaign-Urbana, Amer. Meteor. Soc., 35-38.
- _____, _____, and B.L. Barge, 1972: The anisotropy of precipitation media. *Nature*, 238, 214-216.
- Morrison, J.A., M.J. Cross, and T.S. Chu, 1973: Rain-induced differential attenuation and differential phase shift at microwave frequencies. *Bell System Tech. J.*, 52, 599-604.
- Newell, R.E., S.G. Geotis, M.L. Stone, and A. Fleisher, 1955: How round are raindrops? *Proc. Fifth Wea. Radar Conf.*, Fort Monmouth, Amer. Meteor. Soc., 261-68.
- _____, _____, and A. Fleisher, 1957: The shape of rain and snow at microwavelengths. *MIT Weather Radar Research Rep.*, No. 28, 103 pp.

- Oguchi, T., 1960: Attenuation of electromagnetic wave due to rain with distorted raindrops. *J. Radio Res. Lab.*, 7, 467-485.
- _____, 1964: Attenuation of electromagnetic wave due to rain with distorted raindrops (Part II). *J. Radio Res. Lab.*, 11, 19-43.
- _____, 1966: Scattering and absorption of a millimeter wave due to rain and melting hailstones. *J. Radio Res. Lab.*, 13, 141-157.
- Peter, T.V., 1966: The polarization of radar returns from rain. *Trans. South African Inst. Elec. Engr.*, Nov., 234-250.
- Pruppacher, H.R., and R.L. Pitter, 1971: A semi-empirical determination of the shape of cloud and rain drops. *J. Atmos. Sci.*, 28, 86-94.
- Shupiatskii, A.B., 1959: Radar scattering by non-spherical particles. *Tsentral'naia Aerologicheskaja Observatoriia, Trudy*, No. 30, 39-52.
- _____, and S.P. Morgunov, 1963: The application of polarization methods to radar studies of clouds and precipitation. *Trudy Vsesoiuznoe Nauchi Meteorogicheskoi Soveshchaniia Leningrad*, pp. 295-305.
- Van de Hulst, H.C., 1957: Light Scattering by Small Particles. New York, John Wiley and Sons, Inc., 470 pp.
- Watson, P.A., and M. Arbabi, 1973: Rainfall crosspolarization at microwave frequencies. *Proc. IEE*, 120, 413-418.
- Wexler, R., 1955: An evaluation of the physical effects in the melting layer. *Proc. Fifth Wea. Radar Conf.*, Fort Monmouth, Amer. Meteor. Soc. 329-334.
- Wolf, E., 1954: Optics in terms of observable quantities. *Nuovo Cimento*, 12, Series 9, 884-888.
- _____, 1959: Coherence properties of partially polarized electromagnetic radiation. *Nuovo Cimento*, 13, Series 10, 1165-1181.
- Zawadzki, I.I., and R.R. Rogers, 1969: ADA, an instrument for real-time display of microwave attenuation due to rain. *Tech. Rep. MWT-6*, Stormy Weather Group, McGill University, Montreal, 19 pp.